

# Fundamentals of perovskite formation for photovoltaics

THÈSE N° 8368 (2018)

PRÉSENTÉE LE 3 FEVRIER 2018

À LA FACULTÉ DES SCIENCES DE BASE

LABORATOIRE DE PHOTONIQUE ET INTERFACES

PROGRAMME DOCTORAL EN CHIMIE ET GÉNIE CHIMIQUE

ÉCOLE POLYTECHNIQUE FÉDÉRALE DE LAUSANNE

POUR L'OBTENTION DU GRADE DE DOCTEUR ÈS SCIENCES

PAR

**Amita UMMADISINGU**

acceptée sur proposition du jury:

Prof. U. A. Hagfeldt, président du jury

Prof. M. Graetzel, directeur de thèse

Prof. J. Maier, rapporteur

Dr J. van de Lagemaat, rapporteur

Prof. L. Forró, rapporteur



ÉCOLE POLYTECHNIQUE  
FÉDÉRALE DE LAUSANNE

Suisse  
2018



# Abstract

Perovskite solar cells have become strong contenders in the arena of photovoltaics due to the stunning rise in their efficiency from 3 % to over 20 % in just seven years. In this time, numerous device architectures and thin film deposition methods have been explored. The sequential deposition and anti-solvent methods are among the most widely used for preparing perovskite solar cells.

Optimizing these perovskite deposition processes to tune the perovskite film morphology plays a key role in the race for the highest efficiencies as homogeneity of the film correlates with superior photovoltaic performance. To date, the factors controlling perovskite film formation in various deposition methods and the precise mechanism are little understood. In light of this, the aim of the thesis is to unravel the salient aspects of perovskite film formation.

I first study the formation of methylammonium lead iodide in sequential deposition using confocal laser scanning fluorescence microscopy (CLSM) and scanning electron microscopy (SEM). I discover that illumination during film formation is a major factor in the reaction as it greatly accelerates perovskite formation and tunes the final film morphology by controlling nucleation of lead iodide. The nucleation density increases logarithmically with the illumination intensity. I uncover the mechanism behind this effect and demonstrate that it is a quantum phenomenon and not merely a heating effect. I posit that absorbed light lowers the surface tension, thereby facilitating nucleation. Not only is this effect present in the main deposition methods – sequential deposition and the anti-solvent methods, but also in perovskites of more complex compositions that are employed in state-of-the-art solar cells.

Second, I scrutinize the individual stages in the formation of methylammonium lead iodide perovskite in sequential deposition. SEM-cathodoluminescence imaging identifies the presence of mixed crystalline aggregates composed of methylammonium lead iodide perovskite and lead iodide in forming perovskite films. Using cross-sectional CLSM for the first time, I identify the directionality of perovskite formation. Kinetic monitoring and model fitting bring forward the Avrami models as the most suitable to quantify and represent the formation of perovskite under different conditions of temperature, film thickness and illumination.

Finally, I identify a maturation effect in the perovskite film in solar cells stored in the dark and investigate the dynamic spontaneous coalescence of crystals in the film. During maturation, small crystals merge to form larger ones and this reduces the number of grain boundaries and the associated

trap states, suppressing non-radiative recombination. The photovoltaic performance of high efficiency solar cells thus increases and it is accompanied by a reduction in the hysteresis.

Overall, apart from providing insights into the dynamic nature of deposited films, I present a fundamental understanding of the perovskite formation process in different deposition methods and for various compositions. Such a comprehensive picture aids in the achievement of high photovoltaic performance.

**Keywords:** perovskite, solar cell, photovoltaic, formation, crystallization, nucleation, solid-state reaction, effect of illumination, kinetics, coalescence, sequential deposition, anti-solvent method, confocal laser scanning fluorescence microscopy, scanning electron microscopy, cathodoluminescence



# Résumé

Avec des rendements passant de 3 à plus de 20 % en seulement sept ans, les cellules solaires à base de pérovskite sont devenues des concurrentes incontestables dans l'univers du photovoltaïque. Différentes architectures et procédés de déposition des couches minces ont été explorés. Les méthodes dites de déposition séquentielle et d'anti-solvant sont parmi les plus utilisées dans la préparation des cellules pérovskite.

L'homogénéité de la couche de pérovskite étant corrélée à ses performances photovoltaïques, l'ajustement de sa morphologie *via* l'optimisation des procédés de déposition représente une étape clé dans la course aux rendements. Jusqu'à présent, les paramètres contrôlant la formation des couches de pérovskite au travers de différentes méthodes de déposition ainsi que le mécanisme précis ne sont que très peu compris. Ainsi, le but de cette thèse est de définir et d'expliquer les aspects essentiels à la formation des couches de pérovskite.

Dans un premier temps, j'ai étudié la formation de l'iodure de plomb de méthylammonium par dépôts séquentiels en utilisant un microscope confocal à balayage laser (MCBL) et un microscope électronique à balayage (MEB). J'ai ainsi pu découvrir le rôle primordial des conditions d'illumination. Elles accélèrent drastiquement la formation du matériau et modifient la morphologie finale de la couche en contrôlant la nucléation de l'iodure de plomb. J'ai aussi élucidé le mécanisme derrière cet effet et démontré qu'il impliquait, non pas un simple effet thermique, mais un phénomène quantique.

En effet, j'ai suggéré que la lumière absorbée diminuait la tension de surface, facilitant ainsi la nucléation. Ce phénomène est non seulement présent dans la préparation de simples pérovskites avec les méthodes de déposition principales – séquentielles et anti-solvant – mais aussi lors de la préparation de pérovskites utilisées en pratique dans les cellules solaires et possédant une composition plus complexe.

Par la suite, j'ai examiné minutieusement les différentes étapes de formation de la pérovskite d'iodure de plomb de méthylammonium lors d'un dépôt séquentiel. Les images obtenues par MEB-cathodoluminescence montrent la présence d'un mélange cristallin d'agrégats. La couche de pérovskite ainsi formée se compose de la pérovskite d'iodure de plomb de méthylammonium et d'iodure de plomb. En utilisant pour la première fois la MCBL transversale, j'ai identifié l'orientation de la formation des pérovskites. La cinétique de cette formation a par la suite été déterminée. Les

modèles d'Avrami se sont avérés les plus adaptés pour quantifier et représenter ce phénomène sous différentes conditions de température, d'épaisseur de film et d'illumination.

Pour finir, j'ai étudié le caractère dynamique des couches de pérovskite dans les cellules solaires conservées à l'obscurité et identifié la coalescence spontanée de cristaux à l'intérieur. Au cours de ce phénomène, les petits cristaux s'unissent pour en former de plus grands. Cela réduit les joints de grains et, *a fortiori*, le nombre d'état accessible diminuant la possibilité de recombinaison non-radiative. Les performances photovoltaïques de ces cellules solaires sont ainsi augmentées et le cycle d'hystérésis réduit.

Ainsi, en plus de fournir une étude approfondie sur le caractère dynamique des couches déposées, ma thèse présente des connaissances essentielles et fondamentales pour comprendre les phénomènes impliqués dans la formation des pérovskites de différentes compositions et élaborées grâce à différentes méthodes de déposition. Cette étude détaillée fournit ainsi des informations cruciales pour le développement de cellules photovoltaïques pérovskites à haute performance.

**Mots-clés:** pérovskite, cellule solaire, photovoltaïque, formation, cristallisation, nucléation, réaction à l'état solide, effet de l'illumination, cinétique, coalescence, déposition séquentielle, méthode anti-solvant, microscopie confocal à balayage laser, microscopie électronique à balayage, cathodoluminescence.

# Contents

<b>Abstract .....</b>	<b>i</b>
<b>Résumé .....</b>	<b>iii</b>
<b>List of Figures.....</b>	<b>ix</b>
<b>List of Tables .....</b>	<b>xvii</b>
<b>List of Equations.....</b>	<b>xviii</b>
<b>List of Abbreviations .....</b>	<b>xix</b>
<b>List of Symbols.....</b>	<b>xxi</b>
<b>Chapter 1      Introduction.....</b>	<b>1</b>
1.1    Photovoltaic technologies.....	2
1.2    Nature of perovskite materials.....	5
1.3    Development of perovskite solar cells.....	7
1.3.1 Architectures .....	7
1.3.2 Solution-based deposition methods .....	9
1.3.3 Compositional engineering of perovskites.....	10
1.4    Concepts in crystallization.....	11
1.5    Motivation and experimental approach.....	13
1.6    Characterization techniques .....	14
1.6.1 Optical techniques .....	14
1.6.2 Imaging techniques .....	15
1.6.3 Structural characterization methods.....	17
1.6.4 Solar cell characterization.....	18

1.7	Outline and organization of the thesis.....	20
<b>Chapter 2</b>	<b>The effect of illumination on the formation of perovskite films .....</b>	<b>23</b>
2.1	Introduction.....	23
2.2	Results and discussion .....	24
2.2.1	Conversion in the dark and under illumination .....	24
2.2.2	Nucleation mode and density .....	27
2.2.3	Mechanism of light-activated nucleation .....	31
2.2.4	Photovoltaic devices .....	36
2.2.5	CLSM study of formation of complex perovskites in anti-solvent method .....	42
2.3	Conclusion.....	46
2.4	Materials and methods.....	46
2.4.1	Materials.....	46
2.4.2	Sequential deposition sample preparation .....	47
2.4.3	Confocal laser scanning fluorescence microscopy and image processing.....	47
2.4.4	Ultraviolet-visible spectroscopy and experiments .....	47
2.4.5	Electrochemical experiments .....	47
2.4.6	X-ray diffraction measurements.....	48
2.4.7	Sequential deposition device preparation.....	49
2.4.8	Sequential deposition device characterization .....	49
2.4.9	Anti-solvent method sample and device preparation .....	49
2.4.10	Anti-solvent method device characterization.....	50
<b>Chapter 3</b>	<b>The detailed path of sequential deposition for perovskite formation.....</b>	<b>51</b>
3.1	Introduction.....	51
3.2	Results and discussion .....	53
3.2.1	Stages of the reaction .....	53
3.2.2	Confocal laser scanning fluorescence microscopy .....	59
3.2.3	In-situ isothermal kinetic monitoring and solid-state kinetic model.....	62

3.2.4	In-situ kinetic monitoring in the dark and under illumination .....	63
3.3	Conclusion.....	65
3.4	Materials and methods.....	66
3.4.1	Materials.....	66
3.4.2	Sample preparation.....	66
3.4.3	X-ray diffraction measurements.....	66
3.4.4	Scanning electron microscopy-cathodoluminescence .....	66
3.4.5	Confocal laser scanning fluorescence microscopy and image processing .....	67
3.4.6	Spectroscopy.....	67
<b>Chapter 4</b>	<b>Crystal coalescence in highly efficient perovskite solar cells.....</b>	<b>69</b>
4.1	Introduction.....	69
4.2	Results and discussion .....	70
4.2.1	Photovoltaic performance.....	70
4.2.2	Opto-electronic characterization .....	72
4.2.3	Film morphology.....	74
4.2.4	Thermodynamics of coalescence.....	76
4.3	Conclusion.....	77
4.4	Materials and methods.....	77
4.4.1	Scanning electron microscopy.....	77
4.4.2	Time-correlated single-photon counting measurement.....	77
4.4.3	X-ray diffraction measurements.....	77
4.4.4	Solar cell preparation.....	78
4.4.5	Opto-electronic measurements.....	78
<b>Chapter 5</b>	<b>Conclusion .....</b>	<b>79</b>
5.1	Achieved results.....	79
5.2	Future development.....	80
<b>References.....</b>		<b>83</b>

## Contents

---

<b>Acknowledgements.....</b>	<b>93</b>
<b>Curriculum Vitae.....</b>	<b>95</b>

## List of Figures

Figure 1:1 Estimated share of net electricity generation from different sources in the year a, 2015. b, 2040. (Data source: [4]).....	2
Figure 1:2 Schematic showing the energy bands in a semiconductor.....	3
Figure 1:3 Crystal structure of metal halide perovskites in the cubic phase with the generic chemical formula $ABX_3$ . ....	6
Figure 1:4 Optical measurements of a $CH_3NH_3PbI_3$ film. a, Absorption spectrum (OD, optical density). b, Steady-state photoluminescence (PL) measurement (a.u., arbitrary units).....	6
Figure 1:5 Schematic showing some architectures of perovskite solar cells (dimensions not to scale). a, Mesoscopic with nanocrystalline particles of perovskite. b, Mesosuperstructured. c, Mesoscopic with perovskite infiltrated and as a capping layer. d, Planar. ....	8
Figure 1:6 Schematic of sequential deposition for depositing a $CH_3NH_3PbI_3$ film. ....	9
Figure 1:7 Schematic of the anti-solvent method for depositing a $CH_3NH_3PbI_3$ film. ....	10
Figure 1:8 Schematic depicting CLSM imaging of the surface of a sample containing two semiconductors of different bandgaps. a, Laser excitation of and photoluminescence from one point as the x-y plane is scanned. b, Energy bands of the semiconductors with photoluminescence at different frequencies. c, Photoluminescence from each semiconductor captured by a different detector and digital images are stored. d, Images are pseudocoloured and combined to form a composite image. ....	16
Figure 1:9 A typical example of a J-V measurement of a solar cell measured under illumination.....	19
Figure 2:1 $CH_3NH_3PbI_3$ formation in sequential deposition in the dark and under 1 Sun illumination. In these CLSM images, the emission between 500 and 550 nm attributed to $PbI_2$ [71] is assigned a green colour, while the emission between 700 and 800 nm is attributed to perovskite[69] and assigned a red colour. Colour saturation scales with emission intensity. a, Unreacted $PbI_2$ film. b-e, Sample dipped in MAI solution for respectively 6, 8, 10 and 60 s in the dark. f-i, Sample dipped for	

respectively 2, 4, 6 and 60 s under a light intensity of 1 Sun. Note the shorter dipping times in the right-hand column (under illumination) than in the left (in the dark). Insets show SEM images. All scale bars show 5  $\mu\text{m}$ , and are applicable to both CLSM and SEM images..... 26

Figure 2:2 Growth of  $\text{PbI}_2$  nuclei under different conditions in sequential deposition. a, SEM image showing a standard unreacted  $\text{PbI}_2$  film (as-deposited). b, c, SEM images of standard  $\text{PbI}_2$  films dipped in MAI solution for 4 s: in the dark showing low crystal density (b) and under 1 Sun light intensity showing high crystal density (c). d, e, SEM images of  $\text{PbI}_2$  films annealed at 100  $^\circ\text{C}$  for 1 h, dipped in MAI solution for 4 s: in the dark (d) and under 1 Sun light intensity (e). Scale bars (a-e), 1  $\mu\text{m}$ . It is interesting to compare samples made under 1 Sun light intensity, as the light-activated nucleation is expected to take place and the affinity for nucleation can be assessed. Image (e) shows a sample of initially high crystallinity with substantially fewer crystals growing on the surface after dipping, compared to the analogous standard sample in (c), indicating that amorphous  $\text{PbI}_2$  is required for the growth of nuclei. f, XRD analysis showing the full-width at half-maximum (FWHM) of the Voigt function fits of the (001) reflection of the 2H polytype of  $\text{PbI}_2$  and the corresponding height of the platelet obtained using the Scherrer equation. We observe an increase in platelet height from 17 nm to 36 nm on annealing the standard  $\text{PbI}_2$  sample at 100  $^\circ\text{C}$  for 1 h. The platelet height increases from 17 nm in the standard unreacted  $\text{PbI}_2$  film, to 20 nm and 29 nm, on dipping in 0.038 M MAI in 2-propanol in the dark and under 1 Sun illumination, respectively. On dipping standard  $\text{PbI}_2$  films in 0.038 M EMIm TFSI in 2-propanol (for equivalence with 0.038 M MAI in 2-propanol), an increase in the platelet height from 17 nm to 19 nm and 24 nm was observed, for dipping in the dark and under 1 Sun, respectively. This is similar to the trend seen for dipping in MAI. See Materials and methods for details. .... 28

Figure 2:3 Nucleation density under different illumination conditions. a, From top to bottom, SEM images of samples dipped in MAI solution for 25 s in the dark, under 0.001 Sun, 0.01 Sun, 0.1 Sun and 1 Sun. Imaged regions are 10  $\mu\text{m} \times 7 \mu\text{m}$ . b, Number of  $\text{PbI}_2$ -perovskite mixed crystals identified from the images shown in (a). c, Absorbance spectrum of an unreacted  $\text{PbI}_2$  film (OD, optical density). Absorption tail states (the 'Urbach tail'), attributed to inherent disorder of the material, are visible. d, SEM image of sample dipped for 25 s under monochromatic illumination of 2.0 eV. e, As (d), but under monochromatic illumination of 2.5 eV. Scale bars (d, e), 2.5  $\mu\text{m}$ . .... 29



Figure 2:4 SEM images of  $\text{CH}_3\text{NH}_3\text{PbI}_3$  films prepared using sequential deposition under various temperature and light conditions.  $\text{PbI}_2$  films were dipped isothermally in MAI solution for 25 s at the following conditions: a, 35 °C under 0.01 Sun illumination; b, 50 °C under 0.01 Sun; c, 35 °C under 1 Sun; and d, 50 °C under 1 Sun. Dipping at a higher temperature and the same light intensity gives larger perovskite crystals; dipping at a higher light intensity and the same temperature gives a higher nucleation density with small crystals. Scale bars (a–d), 2  $\mu\text{m}$ . ..... 30

Figure 2:5 Electrochemical experiments. a, b, Photograph (a) and cross-sectional diagram (b) of a  $\text{PbI}_2$  electrode. c, d, Photograph (c) and diagram (d) of set-up with a  $\text{PbI}_2$  electrode in contact with 0.38 M EMIm TFSI in 2-propanol, used for chopped light chronopotentiometry and EIS measurement. WE, working electrode; Ref, reference electrode; CE, counter electrode. e, Diagram of set-up used to determine the chemical potential of 0.038 M MAI in 2-propanol (IPA) solution, and f, the corresponding chronopotentiometry experiment data. The chemical potential of the MAI solution was determined to be + 0.056 V versus Ag/AgCl, KCl (saturated). g, Variable light chronopotentiometric photo-voltage measurement at zero applied current (dark, 0.01 Sun, 0.1 Sun, 1 Sun and dark). The potential under the initial dark condition is set to zero. h, Mott-Schottky analysis of  $\text{PbI}_2$  film in the dark, where  $C$  is the space-charge layer capacitance normalized by the area considering a geometrically flat surface (Equation 2:4). A flat band potential ( $E_{fb}$ ) of – 0.46 V versus Ag/AgCl, KCl (saturated) was determined from the x-intercept of a fit of the linear region. The upper limit of the charge carrier concentration ( $N_D$ ), considering a geometrically flat surface, was obtained as  $8 \times 10^{19} \text{ cm}^{-3}$ . i, Energy levels versus Ag/AgCl, KCl (saturated) and the equivalent value versus the vacuum level shown. The Ag/AgCl, KCl (saturated) reference electrode was calibrated by dissolving ferrocene (Fc) in the ionic liquid solution and verifying that the position of the  $\text{Fc}/\text{Fc}^+$  couple was + 0.4 V versus Ag/AgCl, KCl (saturated), consistent with the literature[79]. The energy levels determined from f, g and h are shown. Electron-quasi-Fermi level under illumination is denoted by  $E_F^*$ . Reported values[80] for the conduction band (CB) and valence band (VB) edges of  $\text{PbI}_2$  are also shown... 31

Figure 2:6 Energy band diagrams of  $\text{PbI}_2$  film and 0.038 M MAI in 2-propanol solution in the dark and under 1 Sun illumination. Diagrams constructed using data from Figure 2:5i and band bending assumed in both cases.  $E_F$ , Fermi level;  $\mu_{\text{MAI}}$ , chemical potential of the electrolyte (MAI solution). a, In the dark, after contact and electrostatic equilibration, and b, under 1 Sun illumination, with the limits of surface

traps obtained from the Mott-Schottky analysis shown in blue. Quasi Fermi level for holes not shown. .... 32

Figure 2:7 Diagrams of the nucleation mechanism in the  $\text{PbI}_2$  film. a,  $\text{PbI}_2$  film as-deposited, showing amorphous domains and crystalline clusters. A crystalline cluster embedded in the amorphous component is shown with the (001) face exposed. b, Dipping the  $\text{PbI}_2$  film in the MAI solution. c, Accumulation of  $\text{I}^-$  ions at the interface in the MAI solution due to photo-generated holes trapped at the  $\text{PbI}_2$  surface.  $\text{PbI}_2$  transport from amorphous domains to a crystalline cluster is shown. d, Dependence of free-energy change on cluster size: contributions from interfacial and volume terms are shown, with the critical free energy of nucleation ( $\Delta G^*$ ) and the critical cluster size ( $N^*$ ) in the dark and under illumination. e, Cluster size distribution in an as-deposited  $\text{PbI}_2$  film. The fraction of the clusters acting as nuclei and growing in the dark is shown in grey. f, The fraction of the clusters growing under illumination is shown in orange..... 34

Figure 2:8 Effect of populating surface traps. Shown are SEM images of  $\text{PbI}_2$  films that have been dipped for 6 s in 0.038 M MAI in 2-propanol solution; a, in the dark, no voltage bias; b, under 0.02 Sun illumination, no voltage bias; and c, under 0.02 Sun illumination, bias of + 0.8 V versus the Nernst potential of MAI. Panels (b) and (c) show comparable nucleation density, while that in (a) is low. Scale bars (a–c), 2  $\mu\text{m}$ . .... 35

Figure 2:9 Statistical analysis of photovoltaic data (backward scans) recorded under simulated AM1.5G illumination. Left-hand panels (a–d) represent 5  $\text{CH}_3\text{NH}_3\text{PbI}_3$  devices of each condition (dipped into MAI solution in the dark, and under 0.1 Sun and 1 Sun illumination) fabricated using sequential deposition. Centre panels (e–h) represent 6  $\text{CH}_3\text{NH}_3\text{PbI}_3$  devices of each condition (made in the dark and under 1 Sun illumination) prepared using the anti-solvent method. Righthand panels (i–l) represent 10 Rb-incorporated perovskite devices of each condition (made in the dark and under 1 Sun illumination) prepared using the anti-solvent method. a, e, i, Short-circuit current density ( $J_{sc}$ ). b, f, j, Open-circuit voltage ( $V_{oc}$ ). c, g, k, Fill factor (FF). d, h, l, Power conversion efficiency (PCE). The upper and lower error bars represent the maximum and minimum values respectively, and the mid-line in each box represents the median value. The top and the bottom of the box represent the upper quartile (75<sup>th</sup> percentile, Q3) and lower quartile (25<sup>th</sup> percentile, Q1) respectively, and box height represents the interquartile range (Q3–Q1). Filled

squares indicate the mean values shown in Table 2:1. See Materials and methods for details of illumination..... 37

Figure 2:10 Photovoltaic device characterization and analysis of  $\text{CH}_3\text{NH}_3\text{PbI}_3$  samples made using sequential deposition. a–c, SEM images of the perovskite films corresponding to devices dipped into MAI solution in the dark, and under 0.1 Sun and 1 Sun respectively. Scale bars (a–c), 1  $\mu\text{m}$ . d, Absolute IPCE spectra (solid lines) and the integrated current densities (dashed lines) of representative devices dipped into MAI solution in the dark and under 1 Sun. e, XRD spectra of perovskite films dipped into MAI solution in the dark, and under 0.1 Sun and 1 Sun. The main reflections corresponding to the tetragonal perovskite have been indicated. \* Reflections of the  $\text{PbI}_2$  in the 2H polytype; § reflections from the FTO. Similar amounts of  $\text{PbI}_2$  remain in all the films. .... 39

Figure 2:11 Absolute IPCE spectra (solid lines) and the integrated current densities (dashed lines) of representative devices prepared using the anti-solvent method in the dark and under 1 Sun illumination. a,  $\text{CH}_3\text{NH}_3\text{PbI}_3$ ; b, Rb-incorporated composition. .... 40

Figure 2:12 Images of  $\text{CH}_3\text{NH}_3\text{PbI}_3$  films made using the anti-solvent method in the dark and under a light intensity of 1 Sun. Main panels, SEM images. a, Film made in the dark showing low perovskite crystal density. b, Film made under 1 Sun illumination showing high perovskite crystal density. Insets show CLSM images with emission between 700 nm and 800 nm attributed to perovskite and assigned a red colour. Colour saturation scales with emission intensity. Scale bars: main panels (a, b), 0.5  $\mu\text{m}$ ; insets (a, b), 5  $\mu\text{m}$ ..... 41

Figure 2:13 SEM images of perovskite films prepared using the anti-solvent method. a, b, Double-cation composition made in the dark (a) and under 1 Sun illumination (b). c, d, Triple-cation composition made in the dark (c) and under 1 Sun (d). Scale bars (a–d), 1  $\mu\text{m}$ . e, f, Rb-incorporated composition made in the dark (e) and under 1 Sun (f). Scale bars (e, f), 2  $\mu\text{m}$ . .... 42

Figure 2:14 Optical measurements of unannealed perovskite films of the double-cation and the triple-cation compositions. a, Absorption spectra (OD, optical density). b, Steady-state photoluminescence (PL) measurements (a.u., arbitrary units)..... 43

Figure 2:15 Unannealed perovskite films of a–d, the double-cation, e–h, the triple-cation and i–l, the Rb-incorporated compositions. In these CLSM images, the emission between 640 and 650 nm is assigned a green colour (images a, e, i), while the emission between 680 and 690 nm is assigned a blue colour (images b, f, j) and the emission between 725 and 735 nm is assigned a red colour (images c, g, k). Composite images showing all three emissions for each sample are shown in images (d), (h) and (l). Colour saturation scales with emission intensity. Images are 26.36x26.36  $\mu\text{m}^2$  each..... 45

Figure 3:1 XRD analysis of  $\text{PbI}_2$  crystallization and perovskite formation. a, XRD spectra of  $\text{PbI}_2$  samples dipped in MAI for 2, 4, 8, 25, 50, 200 and 400 s, showing the (001) reflection of the 2H polytype of  $\text{PbI}_2$ , the (002) and (110) reflections of the tetragonal perovskite. b, FWHM of the (001) reflection of  $\text{PbI}_2$  and of the (110) reflection of the perovskite vs. time for the spectra shown in (a). ..... 53

Figure 3:2 Schematic depicting the stages of the reaction in sequential deposition. Dashed arrows indicate mass transfer. a, Nucleation and growth of  $\text{PbI}_2$ . b, Intercalation of MAI and structural reorganization to form  $\text{CH}_3\text{NH}_3\text{PbI}_3$  perovskite. c, Ostwald ripening where perovskite from the mesoporous layer is transported to the capping layer. d, Further Ostwald ripening at longer dipping times where perovskite from the small crystals in the capping layer is transported to larger ones. e, Gibbs free energy shown as a function of the reaction coordinate. .... 54

Figure 3:3 XRD spectra of unreacted  $\text{PbI}_2$  sample and sample dipped in MAI solution for 4 s in the dark. The (001), (002), (003) and (004) reflections of the 2H polytype are indicated and reflections from the FTO have been indicated with \*. ..... 55

Figure 3:4 Perovskite formation with time studied using SEM. a, Unreacted  $\text{PbI}_2$  film. b, Sample dipped for 2 s showing the growth of nuclei as hexagonal platelets of  $\text{PbI}_2$ . c, Sample dipped for 4 s showing hexagonal platelets of  $\text{PbI}_2$  on the crystal surfaces. d, Sample dipped for 8 s showing the textured crystals. Scale bars (a-c), 0.5  $\mu\text{m}$ . (d), 1  $\mu\text{m}$ . .... 56

Figure 3:5 Cathodoluminescence study on films of intermediate conversion. a, SEM image of sample dipped for 10s with clusters visible on the crystals. Scale bar, 0.5  $\mu\text{m}$ . b, CL spectra taken at two different points on the same sample.  $\text{PbI}_2$  emission between 480 and 550 nm is assigned green and perovskite emission between 720 and 810 nm is assigned red. c, Pseudocolour CL image overlay on SEM image of the same sample showing mixed crystalline aggregates composed of perovskite and

PbI<sub>2</sub>. Scale bar, 0.5  $\mu$ m. d, Pseudocolour CL image overlay on SEM image. The crystal is perovskite while the clusters (indicated with arrows) on it are identified as PbI<sub>2</sub>. Scale bar, 0.5  $\mu$ m. .... 57

Figure 3:6 Cathodoluminescence study on a sample dipped for 60 s for nearly complete conversion. a, CL spectrum at a point on a sample. The emission between 720 and 810 nm, attributed to perovskite, is assigned red. b, Pseudocolour CL image overlay on a SEM image of the same sample. Scale bar, 1  $\mu$ m..... 58

Figure 3:7 SEM images of perovskite films with increasing dipping times showing Ostwald ripening. a, Dipped for 400 s. b, Dipped for 800 s. Scale bars (a- b), 1  $\mu$ m. 59

Figure 3:8 Confocal laser scanning fluorescence microscopy of samples with a 2.5  $\mu$ m mesoporous Al<sub>2</sub>O<sub>3</sub> layer. Emission between 500 and 550 nm attributed to PbI<sub>2</sub> and assigned green colour and emission between 700 and 800 nm attributed to perovskite and assigned red colour. The colour saturation scales with the emission intensity. a, Schematic showing planes parallel to the sample surface and the cross section, showing the different parts of the sample being imaged. b, Composite pseudocolour image of the surface of a sample of intermediate conversion dipped for 60 s. Scale bar, 5  $\mu$ m. c, Composite pseudocolour cross-sectional image of the same sample showing the perovskite capping layer, over the unconverted PbI<sub>2</sub> in the mesoporous layer. Scale bar, 1  $\mu$ m. d, Normalized emission intensity showing horizontally averaged values of PbI<sub>2</sub> emission and perovskite emission across the depth of the sample in (c). e, Composite pseudocolour cross-sectional image of a sample of nearly complete conversion showing trapped, unconverted PbI<sub>2</sub> in the mesoporous layer. Scale bar, 2  $\mu$ m..... 61

Figure 3:9 In-situ kinetic data of perovskite formation. a, Isothermal kinetic data at 10, 15 and 25°C shown as the conversion fraction ( $\alpha$ ). b, Isothermal reaction rate ( $d\alpha/dt$ ) shown as a function of conversion fraction ( $\alpha$ ) for data in (a). c, Kinetic data for samples of low and high PbI<sub>2</sub> loading dipped under light and in the dark, shown as the conversion fraction ( $\alpha$ ). .... 62

Figure 4:1 Current density-voltage (J-V) curves for a perovskite solar cell at a, 2 and b, 28 days after preparation, storing the device in the dark and in dry air at room temperature. The J-V curves were measured at a scan rate of 10 mV s<sup>-1</sup> from forward bias to short circuit condition and from short circuit condition to forward bias under AM1.5 simulated solar light illumination. The device was not preconditioned under

light or voltage bias before each J-V scan. The active area was defined by a shadow mask with an aperture of 0.16 cm<sup>2</sup>. ..... 71

Figure 4:2 Data collected 2 and 28 days after the sample preparation. The samples were stored in the dark and in dry air at room temperature. a, Imaginary part of the intensity modulated photocurrent spectra of a complete perovskite solar cell. The spectra were normalized to the highest peak at 10<sup>5</sup> Hz. b, TCSPC measurement of a perovskite film deposited on a microscope glass slide. The sample was excited at 480 nm from the perovskite side and the emission at 760 nm from the same side was monitored..... 72

Figure 4:3 Mono-exponential function fits of the TCSPC data of the perovskite film a, after 2 days and b, after 28 days of storage in the dark..... 73

Figure 4:4 SEM images of a perovskite film stored for a, 2 days and b, 28 days in dark and dry air at room temperature. c, Statistical distribution of areas of crystals for 2, 14 and 28 days. Data for 2 and 28 days extracted from the SEM top views in d, 2 days and e, 28 days respectively..... 74

Figure 4:5 X-ray diffraction patterns collected 2 and 28 days after perovskite film preparation. The samples were stored in the dark and in dry air at room temperature..... 75

Figure 4:6 Schematic of crystal coalescence in a perovskite film. a, An as-prepared film of crystals with a small crystallographic misorientation at the grain boundary shown in red. Arrows indicate the grain boundary of interest between these crystals. b, Film after dark storage, showing the coalescence of these crystals. c, Cross sectional view of crystals with a small crystallographic misorientation at the grain boundary which preferentially coalesce. d, Cross sectional view of crystals with a large crystallographic misorientation at the grain boundary which do not coalesce. .... 76

## List of Tables

Table 2:1 Photovoltaic device data recorded under simulated AM1.5G illumination. a, Average values of parameters shown with standard deviations from the backward scans of numerous devices (5 CH <sub>3</sub> NH <sub>3</sub> PbI <sub>3</sub> cells made using sequential deposition, 6 CH <sub>3</sub> NH <sub>3</sub> PbI <sub>3</sub> cells made using the anti-solvent method and 10 Rb-incorporated composition cells made using the anti-solvent method) prepared under different illumination conditions. b, Photovoltaic parameters from the forward and backward scans of one device of each preparation condition. The hysteresis of the photovoltaic devices is low.....	38
Table 3:1 FWHM of the (001) reflection of the 2H polytype of PbI <sub>2</sub> and the corresponding height of the platelet from the Scherrer equation. ....	55
Table 4:1 Photovoltaic performance parameters: open-circuit voltage ( $V_{oc}$ ), short circuit current ( $J_{sc}$ ), fill factor (FF) and maximum power conversion efficiency (PCE) extracted from the forward and backward J-V scans in Figure 4:1.....	71
Table 4:2 Averaged photovoltaic parameters from 5 identically-prepared devices: open-circuit voltage ( $V_{oc}$ ), short circuit current ( $J_{sc}$ ), fill factor, power conversion efficiency (PCE) as measured in the forward and backward direction. A 0.148 cm <sup>2</sup> aperture was placed on the active area for measurement. Devices were stored in the dark and in dry air (below 1% relative humidity) at room temperature. ....	71
Table 4:3 Mono-exponential function fit parameters of the perovskite film 2 days and 28 days after storage in the dark.....	73
Table 4:4 Number of crystals extracted from SEM top view images of a sample after 2, 14 and 28 days of storage. All crystal surface areas are in μm <sup>2</sup> . ....	75
Table 4:5 Miller indices (hkl), peak intensity normalized to the intensity of the perovskite peak at 32.3 2θ and the crystal size extracted from the spectra in Figure 4:5. ....	76

## List of Equations

Equation 1:1 – Scherrer equation for estimation of crystallite size[63] .....	18
Equation 1:2 – Equation for fill factor.....	19
Equation 1:3 – Expression for PCE.....	20
Equation 1:4 – Expression for IPCE .....	20
Equation 2:1 – Expression for the critical free energy of nucleation[82] .....	33
Equation 2:2 – Expression for the critical cluster size[82] .....	33
Equation 2:3 – Equation for surface tension[79, 83].....	33
Equation 2:4 – Expression used for Mott-Schottky analysis[81].....	48
Equation 3:1 – General expression for solid-state kinetic models[104] .....	62
Equation 3:2 – Avrami models under isothermal conditions[104] .....	63
Equation 4:1 – Mono-exponential function used for fitting TCSPC data .....	73



## List of Abbreviations

AM	air mass
CB	conduction band
CE	counter electrode
CL	cathodoluminescence
CLSM	confocal laser scanning fluorescence microscopy
DSSCs	dye-sensitized solar cells
EIS	electrochemical impedance spectroscopy
EMIm TFSI	1-ethyl-3-methylimidazolium bis(trifluoromethylsulfonyl)imide
FA	formamidineum
Fc	ferrocene
FEG-SEM	field emission gun scanning electron microscope
FF	fill factor
FK209	tris(2-(1H-pyrazol-1-yl)-4-tert-butylpyridine)-cobalt(III)tris(bis(trifluoromethylsulfonyl)imide)
FTO	fluorine-doped tin oxide
FWHM	full width at half maximum
HTM	hole transport material
IMPS	intensity modulated photocurrent spectroscopy
IPA	2-propanol
IPCE	incident-photon-to-current conversion efficiency
J-V	current density-voltage
LED	light-emitting diode
Li-TFSI	bis(trifluoromethylsulfonyl)imide lithium salt
MA	methylammonium

#### List of Abbreviations

---

MAI	methyllummonium iodide
MPP	maximum power point
NA	numerical aperture
PCE	power conversion efficiency
PL	photoluminescence
PTAA	poly-triarylamine
PV	photovoltaics
Ref	reference electrode
SEM	scanning electron microscopy
spiro-OMeTAD	2,2',7,7'-tetrakis (N,N-di-p-methoxyphenyl-amine) 9,9'-spirobifluorene
TBP	4-tert-butylpyridine
TCPSC	time correlated single photon counting
UV	ultraviolet
VB	valence band
Vis	visible
WE	working electrode
XRD	X-Ray diffraction

## List of Symbols

$A_o$	pre-exponential constant
$A_S$	surface area
$\alpha$	conversion fraction
$B$	peak width
$c$	speed of light
$c_o$	double-layer capacitance
$C$	space-charge layer capacitance normalized by the area
$C_{SC}$	space-charge layer capacitance
$e$	elementary charge
$e^-$	electrons
$E_{fb}$	flat band potential
$E_F$	Fermi level
$E_F^*$	electron-quasi-Fermi level under illumination
$E_g$	band gap
$\epsilon_o$	vacuum permittivity
$\epsilon_r$	dielectric constant
$\Delta G^*$	critical free energy of nucleation
$\Gamma_i$	interfacial free energy per unit interfacial area for the $i^{\text{th}}$ area
$\gamma$	interfacial tension
$\gamma_o$	surface tension at zero charge
$h$	Planck constant
$h^+$	hole
$J_{MPP}$	current density at maximum power point
$J_{sc}$	short circuit current density

$k$	effective reaction rate constant
$k_B$	Boltzmann constant
$K$	Scherrer constant
$l$	solid-state kinetic model parameter
$L$	linear dimension of crystallite
$\lambda$	wavelength
$m$	solid-state kinetic model parameter
$\mu$	chemical potential
$n$	solid-state kinetic model parameter, Avrami exponent
$N^*$	critical cluster size
$N_D$	charge carrier concentration
$\eta_i$	shape factor for the $i^{\text{th}}$ area
$\nu$	frequency
$P_{in}$	incident power
$P_{max}$	maximum power output
$\sigma$	excess surface charge
$t$	time
$T$	temperature
$\tau$	decay time
$\theta$	Bragg angle
$V_{fb}$	flat band potential
$V_{oc}$	open-circuit potential
$V_{MPP}$	voltage at maximum power point
$y$	intensity as a function of time
$y_o$	baseline intensity

# Chapter 1 Introduction

*The section on characterization techniques was adapted from the following article with the permission of all co-authors and the journal.*

**Preprint version of the review paper:** A. Ummadisingu, J.-Y. Seo, M. Stojanovic, S. M. Zakeeruddin, M. Grätzel, A. Hagfeldt, N. Vlachopoulos and M. Saliba, "Additives, hole transporting materials and spectroscopic methods to characterize the properties of perovskite films," *Chimia*, vol. 71, pp. 754-761, Nov 2017. (doi : <https://doi.org/10.2533/chimia.2017.754>)

**My contribution:** Prepared the section on the spectroscopic characterization of perovskites.

The world is faced with an ever increasing demand for energy to maintain the growth and development of human civilization[1]. Estimates indicate that the world energy demand could rise to as much as 1000EJ or more by 2050[2, 3]. The world energy consumption in 2010 was close to half that value. It is particularly important to consider our dependence on diminishing energy resources such as fossil fuels as they will contribute to almost 80% of the energy supply through 2040. According to the report by the International Energy Agency – the International Energy Outlook 2017[4], natural gas is the fastest-growing fossil fuel with the global use increasing by around 1.4% every year. Petroleum also shows an increase in utilization with 0.7% growth per year while coal consumption shows little growth (0.1% per year)[4].

Fossil fuels cannot meet the energy demand for more than a couple of decades, for two main reasons. Firstly, although reserves of easily extracted oil, gas and even coal would possibly have peaked in the coming decade owing to increased exploration[5], the production is expected to be hampered by the increasingly stringent regulations placed on fossil fuel use by policy makers and governments. The share of electricity generated from coal for instance is predicted to drop to 30% in 2040 from 40% in 2015 as shown in Figure 1:1[4]. Secondly, fossil fuels are responsible for an estimated 74% of all CO<sub>2</sub> emissions from human activity. These emissions have led to the serious environmental issue of global warming[3]. Growing global consensus on the need to reduce these emissions as a priority motivates the development of and the rapid transition to low-emission alternatives[2, 3]. Consequently, there is a pressing need for new and sustainable solutions to address the future energy demand[1].

The frontrunners for this task of replacing fossil fuels are renewable and nuclear energies, which are the world's fastest growing energy sources[4]. Many energy experts championed nuclear power as an essential component in any climate-change-mitigation strategy[5] and electricity generation from nuclear sources grows by 1.5% per year[4]. However, the aftermath of the nuclear disaster stemming from the earthquake and tsunami in Japan on March 11, 2011 has brought forward concerns regarding

the safety of the technology[5]. As a result, policies to limit or phase out nuclear power have been adopted in several countries. Therefore, the share of electricity generated from nuclear power is expected to be 11% in 2040, the same as in 2015, as shown in Figure 1:1[4].

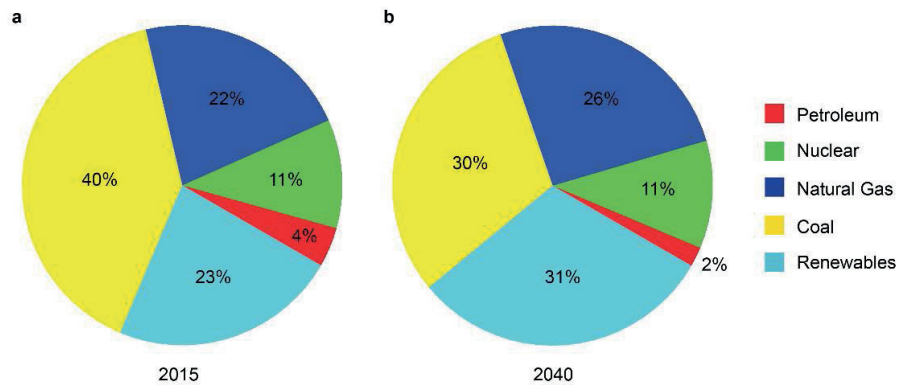


Figure 1:1 Estimated share of net electricity generation from different sources in the year a, 2015. b, 2040. (Data source: [4])

In light of this, renewable energy technologies are the prime candidates to take on the challenging task of tackling the previously mentioned issues and meeting the energy demand. These include solar, wind, ocean, hydro, biomass and geothermal sources[3]. Electricity production from these sources rises by an average of 2.8% per year with predictions for 2040 indicating that they will provide a large share (31%) of electricity generation surpassing that from coal at 30% (see Figure 1:1)[4]. Among these, solar resource is the most promising and the most abundant with nearly 4000 trillion kWh of energy supplied to the earth every day in the form of electromagnetic radiation. This resource can provide for the annual global energy consumption 10,000 times over[2]. Technologies such as concentrating solar thermal power and solar photovoltaics (PV) provide excellent options to harvest this abundant solar resource. Solar PV is the most promising as the fastest growing energy technology in the world with nearly 50 GW of new capacity added every year[1]. The development of various PV technologies will be outlined next.

## 1.1 Photovoltaic technologies

In semiconductor crystals, electrons ( $e^-$ ) are present in energy bands and the bands can be separated by regions in energy where electrons are absent as no wavelike electron orbitals exist. This region in energy where the presence of electrons is forbidden is called the band gap ( $E_g$ ). In the case of insulators, the allowed energy levels are filled or empty, meaning that electrons do not move in an electric field. Metals consist of one or more partly filled bands, while crystals are considered semiconductors if one or more bands are slightly filled or slightly empty.

The conduction band is the one vacant at absolute zero and its lowest point is termed the conduction band edge. On the other hand, the valence band is the one filled at absolute zero and its highest point is the valence band edge. To define the band gap more specifically, it is the difference between the conduction band edge and the valence band edge[6]. A schematic showing the energy bands in a semiconductor is presented in Figure 1:2.

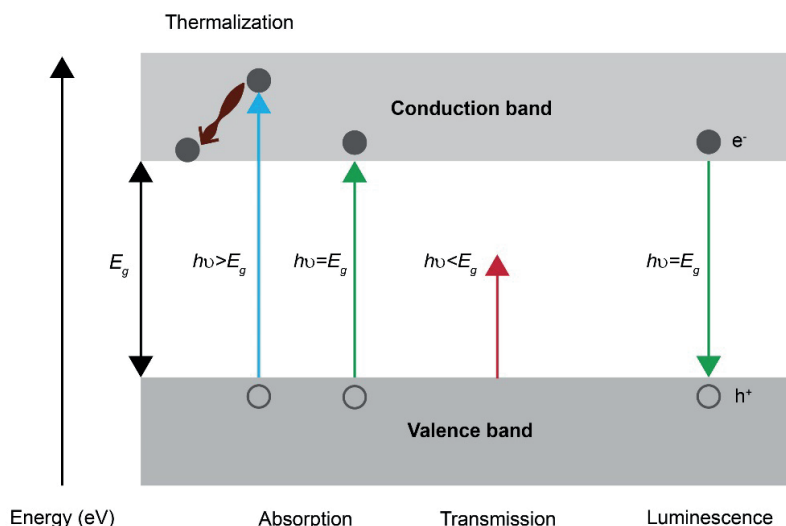


Figure 1:2 Schematic showing the energy bands in a semiconductor.

Semiconductors are the principal photoactive materials used in photovoltaic applications. In a direct absorption process, the absorption of a photon by a semiconductor results in the formation of an electron and a hole ( $h^+$ )[6]. However, only photons of energy greater than or equal to the band gap ( $h\nu \geq E_g$ , where  $h$  is the Planck constant,  $\nu$  is the frequency of light) are absorbed while those of lower energy are transmitted without being absorbed ( $h\nu < E_g$ ) (shown in Figure 1:2). In semiconductors, electron-hole recombination can proceed through a radiative pathway or a non-radiative one. In the radiative pathway, when an electron from the conduction band edge combines with a hole from the valence band edge, a photon of energy corresponding to the band gap is emitted (as shown in Figure 1:2) and this emission is referred to as luminescence. The excitation that generates electron-hole pairs can be provided in a variety of ways including the absorption of photons as mentioned above. Photoluminescence (PL) is the term used for the luminescence observed when annihilation of electron-hole pairs formed through photo-excitation occurs radiatively[7].

The photovoltaic effect was discovered in 1839 by a physicist, Alexandre-Edmund Becquerel. While studying the effect of light on electrolytic cells, he observed that “electrical currents arose from certain light induced chemical reactions”[8]. Others observed similar effects in Selenium several decades later.

It was in the late 1940s that the development of solid-state devices eventually led to the first silicon solar cell with an efficiency of 6%[9].

Silicon solar cells are one of the main types of PV technologies and a large fraction of them are single-junction cells based on wafers made from single crystals or polycrystals. These types of devices are commonly categorized as first-generation PV technologies[10]. However, the downside of these technologies is the relatively high cost incurred in the fabrication due to high material losses and energy consumption[8]. Moreover, silicon wafers are often several hundred microns thick[9]. As an alternative to this technology, thin-film PV technologies emerged where films thinner than 10  $\mu\text{m}$  could absorb the solar spectrum much more efficiently[9, 10]. As smaller quantities of the active materials were needed, this reduced production costs[8]. In these thin-film PV devices that are classified as second-generation technologies, materials such as amorphous silicon, copper indium gallium diselenide, cadmium telluride/cadmium sulphide or polycrystalline silicon are deposited on low-cost substrates such as glass[10].

At this point, it is interesting to discuss the theoretical limitation on the maximum efficiency that can be achieved with a single-bandgap device. The Shockley-Queisser limit restricts efficiencies to either 31% or 41%, for unconcentrated and maximally concentrated light respectively. These efficiencies are obtained by taking into account the irreversibility at maximum power extraction, the Carnot thermodynamic conversion limitation and the loss due to the polychromatic nature of sunlight. The polychromatic nature of the incident sunlight is one of the main losses in solar cells accounting for more than half of the total loss of incident solar energy in its conversion to electricity[11]. This loss consists of two components, the first of which is the sub-bandgap transmission loss since only photons of energy greater than the bandgap of the photoactive material are absorbed. The second component is associated with the hot charge carriers generated when photons of energy greater than the bandgap are absorbed. The relaxation of the hot charge carriers to the conduction band of the photoactive material is termed as thermalization (as shown in Figure 1:2)[12].

Third-generation PV technologies aim to decrease costs below that of the second-generation by significantly increasing efficiencies, without losing the economic and environmental cost advantages of thin-film deposition techniques. These involve approaches to achieve efficiencies higher than that of a single-junction solar cell by addressing both the losses incurred due to the polychromatic nature of the incident sunlight. Third-generation PV technologies include quantum dot cells, tandem or multi-junction cells, intermediate band cells, multiple-carrier excitation, hot-carrier cells and up-conversion and down-conversion technologies[11]. Dye-sensitized solar cells (DSSCs) and organic or polymer cells are also considered third-generation PV technologies[8] though research on these to reach the above-mentioned targets is ongoing.



It is interesting to take a closer look at DSSCs. In these solar cells, a wide band semiconductor such as titanium dioxide ( $\text{TiO}_2$ ) is taken in the form of nanometer-sized particles and it is deposited as a mesoscopic layer. Anchored to the surface of the  $\text{TiO}_2$ , is a sensitizer-a charge transfer dye that absorbs light. Photo-excitation of the dye results in the injection of an electron into the conduction band of the  $\text{TiO}_2$ . Another component of the cell is the electrolyte, which consists of a redox system, such as the iodide/triiodide couple, in an organic solvent. Electron donation from the electrolyte regenerates the dye. Over the years, solid-state DSSCs have been developed where the redox electrolyte was replaced by a solid hole transport material (HTM)[13]. A widely used HTM is the amorphous organic material, 2,2',7,7'-tetrakis (N,N-di-p-methoxyphenyl-amine) 9,9'-spirobifluorene (spiro-OMeTAD)[14].

## 1.2 Nature of perovskite materials

Crystalline materials are widely used by man for different purposes including technological applications. Crystals are solids composed of a three-dimensional periodic arrangement of matter such as atoms, ions and molecules. This periodic order described by the so-called crystal lattice and population of the lattice points with matter gives us the crystal structure. Real crystals consisting of just one grain, without any grain boundaries, are termed perfect single crystals. However, in reality all single crystals are imperfect and contain defects. Polycrystals on the other hand contain several grains which in turn may consist of crystallites of different sizes and crystallographic orientations[15].

In recent years, a crystalline material called perovskite has attracted a lot of attention for use in solar cells. The term 'perovskite' is the name of the mineral form of  $\text{CaTiO}_3$ , which has a crystal structure composed of corner-sharing  $\text{TiO}_6$  octahedra in all three dimensions while Ca occupies the cuboctahedral void in every unit cell[16]. The same crystal structure is present in materials with the generic chemical formula of  $\text{ABX}_3$ , where X is an anion, while A and B are cations with A being larger in size than B[16, 17]. Such materials are also referred to as perovskites and they have been found to be insulating, semiconducting or superconducting[16]. Among these, hybrid organic-inorganic compositions are of interest. The general crystal structure of these materials in the cubic phase, which is generally the phase stable at high temperatures[17], is shown in Figure 1:3. In these hybrid perovskites, organic or inorganic cations occupy the A position (red) while divalent metal cations and halide anions occupy the B (grey) and X (green) positions respectively[18].

One of the most widely investigated perovskites of this type for solar cell applications is methylammonium lead iodide ( $\text{CH}_3\text{NH}_3\text{PbI}_3$ ). This perovskite composition will be the focus of this thesis work. For this material, the stable phase at room temperature is the tetragonal with a transition to the cubic phase taking place at a temperature above 330K[19]. The orthorhombic phase has been reported to be the stable phase at temperatures below 160K[19].

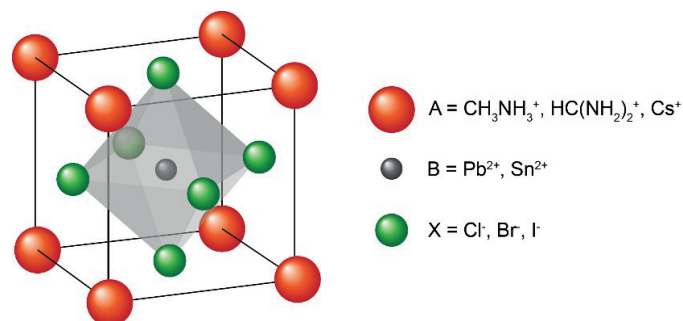


Figure 1:3 Crystal structure of metal halide perovskites in the cubic phase with the generic chemical formula  $\text{ABX}_3$ .

Perovskites have been investigated in the past few decades for their interesting and unique properties. Organo-lead halide perovskites in particular, have been found to be very attractive for use as light harvesters in solar cells due to their excellent optical and electronic properties. These properties include direct bandgaps, large absorption coefficients and high carrier mobilities.  $\text{CH}_3\text{NH}_3\text{PbI}_3$  has a direct band gap of 1.55 eV, which corresponds to its absorption onset of 800 nm[18] as shown in Figure 1:4a.

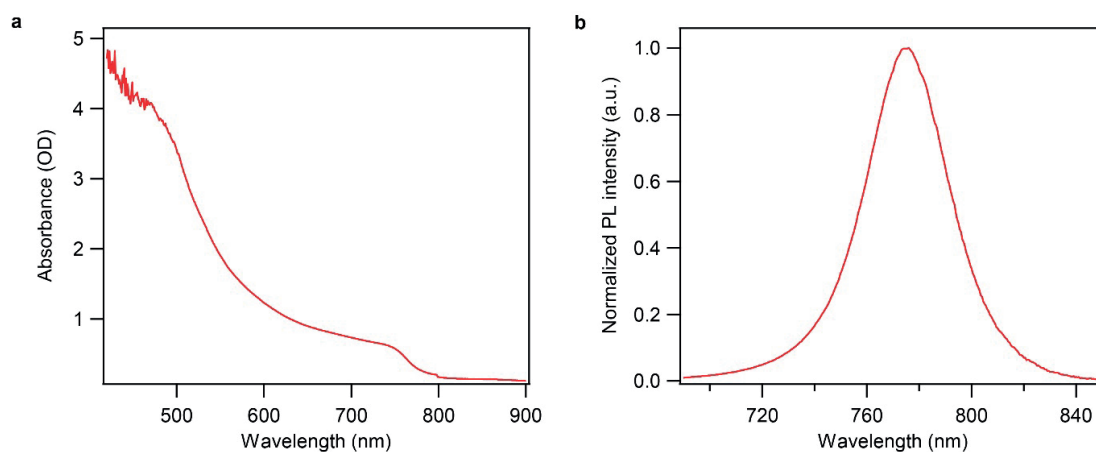


Figure 1:4 Optical measurements of a  $\text{CH}_3\text{NH}_3\text{PbI}_3$  film. a, Absorption spectrum (OD, optical density). b, Steady-state photoluminescence (PL) measurement (a.u., arbitrary units).

The report by De Wolf et al.[20] discussed the interesting implications of the sharp optical absorption edge present in perovskites for photovoltaic performance. In particular, they plotted the absorption coefficient as a function of photon energy for typical photovoltaic materials, including perovskites and identified the presence of absorption tail states, also called the Urbach tail. They took a closer look at these absorption tail states by extracting the Urbach energy, which is the slope of the exponential part of the above-mentioned plot. An increase in the Urbach energy is indicative of the structural disorder of the semiconductor, a crucial aspect of materials used in opto-electronic applications. De Wolf et al. also reported that the  $\text{CH}_3\text{NH}_3\text{PbI}_3$  perovskite has a steep absorption onset, giving an Urbach energy as small as 15 meV, which points to a well-ordered microstructure[20].

As far as the carrier mobilities are concerned, it is interesting that both electron and hole mobilities are relatively high. This is due to the small effective masses for the charge carriers[18]. Reports suggest that the electron mobility in  $\text{CH}_3\text{NH}_3\text{PbI}_3$  films is between  $0.7$  and  $3 \text{ cm}^2 (\text{V s})^{-1}$  while the hole mobility is between  $0.4$  and  $3 \text{ cm}^2 (\text{V s})^{-1}$ [21]. At this point, the milestones in the development of perovskite solar cells will be outlined.

### 1.3 Development of perovskite solar cells

One of the first reports that utilized perovskite materials in solar cells was by Kojima et al. in 2009[22]. In this work, nanocrystalline particles of methylammonium lead iodide perovskite ( $\text{CH}_3\text{NH}_3\text{PbI}_3$ ) or methylammonium lead bromide perovskite ( $\text{CH}_3\text{NH}_3\text{PbBr}_3$ ) were used as the sensitizer to replace the dye in liquid-electrolyte-based DSSCs. The authors demonstrated that methylammonium lead iodide perovskite cells gave a power-conversion efficiency (PCE) of 3.8%. The performance was improved to 6.5% using  $\text{CH}_3\text{NH}_3\text{PbI}_3$  as reported by Im et al. in 2011[23]. This was achieved by changing both the electrolyte formulation and the perovskite deposition method[18].

A major shift in the field occurred through the replacement of the liquid electrolyte with a solid-state HTM, spiro-OMeTAD as described in the report by Kim et al.[24] in 2012. As mentioned earlier, this hole-transport material was already in use in solid-state DSSCs. Since then, there has been a rapid increase in the number of publications in the field of solar cells where these hybrid perovskites are used. Major developments in the field that followed will be described below under the classification of device architectures and deposition methods.

#### 1.3.1 Architectures

Several perovskite solar cell architectures have been introduced over the years and those most widely studied are mentioned here. The solar cells discussed so far were based on the architecture used in DSSCs often referred to as the mesoscopic architecture. They consisted of a mesoporous  $\text{TiO}_2$  layer, which is the electron transport layer resting on a glass substrate coated with a conductive material, for instance fluorine-doped tin oxide (FTO). The nanocrystalline particles of the perovskite are deposited onto the mesoporous scaffold and the HTM is deposited on top followed by the metallic electrode (see Figure 1:5a).

An interesting development was reported in 2012 by Lee et al.[25] who prepared perovskite solar cells in the so-called mesosuperstructure architecture. In this architecture, an  $\text{Al}_2\text{O}_3$  scaffold was used instead of the  $\text{TiO}_2$  layer and the perovskite was infiltrated into the pores of the mesoporous scaffold covering the entire scaffold (see Figure 1:5b). They achieved a PCE of 10.9% with this fabrication process. As electrons cannot be injected from the perovskite into the insulating  $\text{Al}_2\text{O}_3$  scaffold, they are

transported through the perovskite itself. In the same year, Etgar et al.[26] demonstrated that a HTM-free solar cell could give a PCE of 5.5%. The high hole mobility of perovskite has been mentioned earlier and this report highlighted this aspect by demonstrating that the perovskite can also act as a hole conductor.

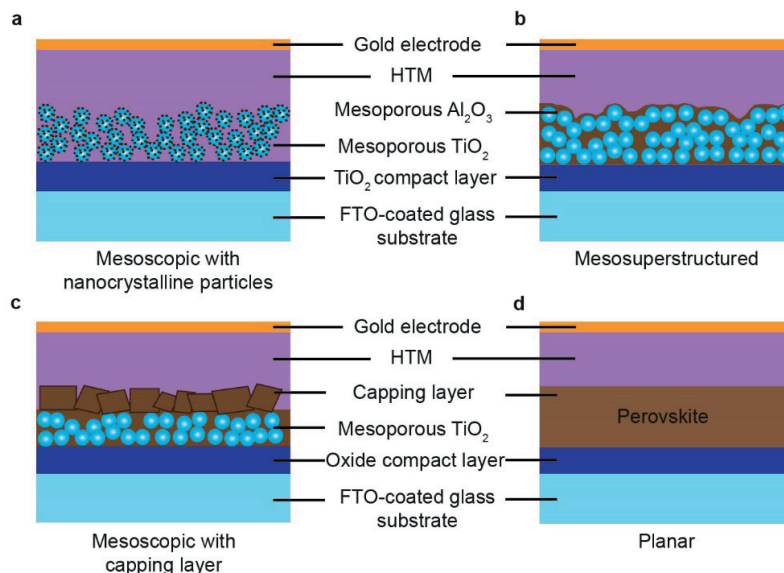


Figure 1:5 Schematic showing some architectures of perovskite solar cells (dimensions not to scale). a, Mesoscopic with nanocrystalline particles of perovskite. b, Mesosuperstructured. c, Mesoscopic with perovskite infiltrated and as a capping layer. d, Planar.

The work by Heo et al.[27] in 2013 presented a layered architecture, which builds on the mesoscopic architecture described above. Two interesting improvements were reported. First, the pores of the mesoporous  $\text{TiO}_2$  film are infiltrated with  $\text{CH}_3\text{NH}_3\text{PbI}_3$  and an overlayer of the perovskite (also called the capping layer) exists on top of the mesoporous  $\text{TiO}_2$  film as shown in Figure 1:5c. This process of filling the unoccupied space in the pores with perovskite provided a high concentration of perovskite in the given volume. Second, a polymeric hole conductor, poly-triarylamine (PTAA) was used and it penetrated into the gaps between the perovskite crystals in the over layer. This was a critical aspect as it increased contact between the HTM and perovskite overlayer. Due to both these aspects, an increase in the PCE to 12% was achieved[27]. In the years that followed, this architecture consisting of both mesoscopic perovskite and a capping layer of the perovskite on top was widely investigated and it will be taken up in this thesis.

Studies also looked into and confirmed the ambipolar nature of the perovskite previously indicated by the reports by Lee et al.[25] and Etgar et al.[26]. This led to the development of the planar architecture which omits the mesoscopic scaffold altogether[18] (see Figure 1:5d). At this point, the fully printable architecture introduced by Mei et al.[28] in 2014 will also be described. These cells consist of a layer of mesoporous  $\text{TiO}_2$  and another mesoporous layer of  $\text{ZrO}_2$  amounting to about  $3\text{ }\mu\text{m}$ , as a scaffold

infiltrated with perovskite and covered by a porous carbon film instead of a hole conductor. This architecture will also be discussed later in the thesis.

### 1.3.2 Solution-based deposition methods

During the short span of a few years, remarkable results have been obtained in terms of prototype solar cell efficiencies. These materials have been shown to give high efficiencies as high as 22% through solution-based fabrication methods. In general, solution-based deposition methods have great potential due to the ease of scale up for large-scale production. Therefore, these achievements are very promising for the scale up of perovskite photovoltaics in the near future[29, 30]. The high solar cell performances achieved in this short period of time are largely due to the extensive effort that has been invested over the years to develop and optimize these perovskite thin film deposition procedures[18]. These methods include single-step deposition[23], sequential deposition[31, 32] and anti-solvent methods[33, 34]. Among these, sequential deposition and anti-solvent methods are two of the most widely used for the fabrication of solar cells.

Sequential deposition was first introduced by Liang et al.[32] in 1998 for the preparation of perovskite thin films. The method was optimized by Burschka et al.[31] in 2013 for the fabrication of efficient solar cells. Since then, sequential deposition has been widely used for the preparation of solar cells. In this method, the formation of a methylammonium lead iodide perovskite ( $\text{CH}_3\text{NH}_3\text{PbI}_3$ ) film is achieved through two steps. First, a lead iodide ( $\text{PbI}_2$ ) solution is infiltrated into a mesoporous  $\text{TiO}_2$  film and then the film is dried. Second, the  $\text{PbI}_2$  film is dipped in a solution of methylammonium iodide (MAI) in 2-propanol for a few seconds resulting in the formation of the perovskite. A schematic showing the deposition steps is presented as Figure 1:6.

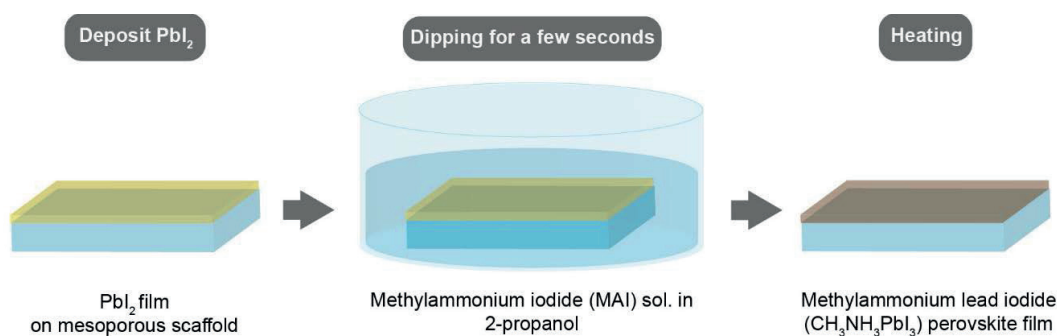


Figure 1:6 Schematic of sequential deposition for depositing a  $\text{CH}_3\text{NH}_3\text{PbI}_3$  film.

The anti-solvent method was introduced by Jeon et al.[34] in 2014 and it is the route employed in the more recent fabrication of high efficiency solar cells in 2016[33, 35]. In this method, a perovskite precursor solution is spin-coated, and then an anti-solvent is dripped, following which the sample is heated as shown in Figure 1:7. This results in the formation of a thin-film of perovskite.

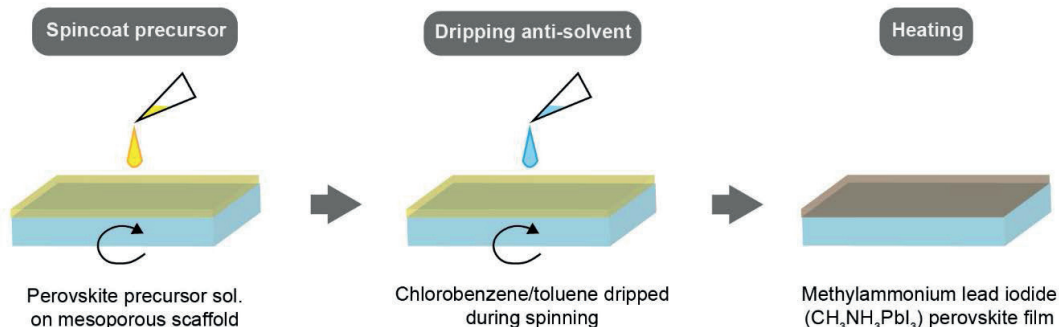


Figure 1:7 Schematic of the anti-solvent method for depositing a  $\text{CH}_3\text{NH}_3\text{PbI}_3$  film.

### 1.3.3 Compositional engineering of perovskites

In addition to  $\text{CH}_3\text{NH}_3\text{PbI}_3$ , other perovskite compositions have also been explored for use in solar cells. As the band gap of the perovskite and other opto-electronic properties can be tuned by changing its composition, several studies have looked into replacing or mixing ions at different positions in the perovskite structure. As a result, highly complex perovskites have been engineered with multiple cations and halides in order to achieve better solar cell performances[35, 36] or to achieve specific bandgaps needed for tandem applications[37]. For instance, Pellet et al.[38] investigated changes to the perovskite composition using formamidinium ions ( $\text{HC}(\text{NH}_2)_2^+$ , FA) at the A site to fully or partially replace the methyl ammonium ions ( $\text{CH}_3\text{NH}_3^+$ ). Formamidinium lead iodide ( $\text{FAPbI}_3$ ) has a smaller band gap 1.48 eV and consequently a red-shifted absorption onset at 840 nm, which facilitates a broader absorption of the solar spectrum compared to  $\text{CH}_3\text{NH}_3\text{PbI}_3$ [38, 39]. The report by Jeon et al.[34] showed mixed iodide-bromide perovskite compositions designated  $\text{CH}_3\text{NH}_3\text{Pb}(\text{I}_{1-x}\text{Br}_x)_3$ . The substitution of  $\text{I}^-$  by  $\text{Br}^-$  increases the band gap of the resulting perovskite[40]. Following these publications, Yang et al.[41] achieved a PCE of 20.1% using a perovskite of the formula  $\text{FA}_{1-x}\text{MA}_x\text{Pb}(\text{I}_{1-y}\text{Br}_y)_3$ . The report by Correa-Baena et al.[42] demonstrated that a PCE of 18% could be achieved for planar architectures with  $\text{SnO}_2$  as the electron selective layer using a perovskite with a nominal composition of  $\text{MA}_{0.17}\text{FA}_{0.83}\text{Pb}(\text{I}_{0.83}\text{Br}_{0.17})_3$ . This formulation is referred to as the ‘double-cation composition’ later in Chapter 2. Bi et al.[33] showed a formulation with excess  $\text{PbI}_2$  in the perovskite precursor solution to further improve the PCE to 20.8%.

Caesium was included into the perovskite structure at the A position giving perovskites of the formula  $\text{Cs}_x\text{FA}_{1-x}\text{Pb}(\text{I}_{1-y}\text{Br}_y)_3$ . The composition was optimized for single-junction solar cells in the report in 2015[43] and for tandem solar cells in the publication in 2016[37]. Saliba et al.[36] showed that the perovskite of the nominal composition  $\text{Cs}_{0.05}(\text{MA}_{0.17}\text{FA}_{0.83})_{0.95}\text{Pb}(\text{I}_{0.83}\text{Br}_{0.17})_3$  gave cells with improved stability, reproducibility and efficiency. The reported optimal composition is referred to as the ‘triple-cation composition’ later in Chapter 2.

Rubidium iodide was used as an additive in the perovskite precursor solution in our report in 2016 to improve cell performance[35]. At this point, a short summary of those reported findings is presented. We demonstrated the practical improvements in the photovoltaic performance of solar cells when the Rb-incorporated perovskite is used. For this composition, we achieved stabilized PCEs of up to 21.6% for the best-performing cell with an average PCE of 20.2% for small areas. We also demonstrated a stabilized PCE of 19.0% on a 0.5 cm<sup>2</sup> cell. An open-circuit voltage of 1.24 V at a band gap of 1.63 eV gives a loss-in-potential of 0.39 V. This is lower than the value of 0.4 V achieved by commercial silicon cells. Solar cells with the Rb-incorporated composition using PTAA as the HTM maintained 95% of their initial performance at 85°C for 500 hours under full solar illumination and maximum power point tracking[35]. Perovskite films made using this procedure are designated 'Rb-incorporated composition' in Chapter 2.

While the above mentioned compositions result in 3-dimensional perovskites, some publications in the field have also looked into 2-dimensional perovskite structures for photovoltaics[44]. Others have explored tin-based perovskites where tin replaces some or all of the lead in the perovskite structure[45]. In this thesis, the focus is on 3-dimensional lead-based perovskites.

## 1.4 Concepts in crystallization

As a large part of this thesis focuses on the formation of crystalline perovskite films, some concepts in crystallization are introduced at this point. The complex phenomenon of crystal growth has been studied extensively in the past decades. However, many aspects of it have not yet been completely understood. Some of the theoretical background used to interpret the results in this thesis are explained here. To begin with, crystal growth or the formation of a new crystalline phase in the mother phase takes place in three general cases: growth from a melt or solution, growth from a vapour or gas phase and growth within a solid phase[15].

The driving force for crystallization is the supersaturation[15], which is the difference in the chemical potentials of the mother phase and the new phase[46]. The formation of the new phase commences with nucleation. Classical nucleation theory defines nucleation and the associated critical particle size of a new phase as follows. If the particle is of subcritical size, energy is needed for growth, while if the particle is of supercritical size, energy is released during growth. The formation of a particle of supercritical size from one of subcritical size is termed nucleation[47]. There is an activation barrier associated with nucleation and it is the work needed for the formation of the critical nuclei[46].

There are two classes of nucleation, namely homogeneous and heterogeneous nucleation. Homogeneous nucleation involves the spontaneous formation and growth of minute particles of a new phase in another phase. On the other hand, in heterogeneous nucleation, the formation and growth of



the new phase takes place on a foreign particle or surface as this lowers the energy barrier for formation[48]. Nucleation processes can also be classified as primary or secondary nucleation. Primary nucleation takes place spontaneously in the homogeneous case and with the aid of foreign particles in the heterogeneous case. In contrast, secondary nucleation is only initiated by crystals of the new phase that are already present in the system[15].

The rate of formation of particles of supercritical size is termed the nucleation rate. Four modes of nucleation have been described in the literature based on the nucleation rate present in the system. They are continuous nucleation, saturation by pre-existing nuclei, Avrami nucleation and mixed nucleation mechanisms. Continuous nucleation is characterized by the presence of a continuous nucleation rate at constant temperature with no nuclei present at the start[47].

Now consider the opposite case where some particles of the new phase are already present at the beginning of the crystallization and the nucleation rate is zero. Such particles can be formed through the rapid cooling of a stable phase from a higher temperature, which can result in the formation of a metastable phase, such as an amorphous alloy with the tendency to crystallize. Based on the thermal treatment it was subjected to, the metastable phase could have particles of a new, stable phase present in it with some particle size distribution. These particles of the new, stable phase have the potential to grow under the right conditions. Therefore, for greater clarity, all particles of the new, stable phase are termed potential nuclei in this thesis. However, only the fraction of these particles whose size exceeds the critical size would grow and this critical size is determined by the parameters such as the temperature[47]. That fraction of particles that are larger than the critical size and grow have been referred to as pre-existing nuclei in the literature[47] and such a nucleation mode is called saturation by pre-existing nuclei.

The next mode of nucleation discussed will be Avrami nucleation. Here, particles of supercritical size or nuclei are formed from those of subcritical size, all the while maintaining the total number of sub and supercritical particles constant. Avrami nucleation resembles continuous nucleation at the start of nucleation and approaches the saturation by pre-existing nuclei mode at the end[47].

The final mode of nucleation is mixed nucleation where combinations of the above nucleation modes are present. A combination of saturation by pre-existing nuclei mode and either continuous nucleation or Avrami nucleation can be helpful to describe some systems. However, the combination of continuous and Avrami nucleation modes is less physically meaningful given that in both modes, the number of nuclei increases with time[47].



## 1.5 Motivation and experimental approach

Remarkable progress has been made in terms of photovoltaic performance of perovskite solar cells through improvements in architectures, deposition methods and compositions. Many of these advances improved the perovskite film quality by engineering the morphology of the polycrystalline perovskite film. Reports indicate that the film morphology may determine the opto-electronic properties of the film. Therefore, it determines the final solar cell performance[49, 50].

Nevertheless, control of the perovskite film morphology by altering the deposition process is not straightforward as effects are difficult to predict considering the fact that some of the fundamental aspects of the perovskite formation remain unknown and are yet to be investigated. Such an issue is especially important for the scale-up of perovskite solar cell technology where control over the process is critical for consistently achieving superior film quality for high device performance. Therefore, it is necessary to have knowledge about the various factors of the formation process, which would help achieve better control over perovskite morphology and enable tailoring of the perovskite films as per the requirement.

The aim of the thesis is to obtain a comprehensive understanding of perovskite formation through various routes and understand related phenomenon in deposited perovskite films and solar cells. To accomplish this goal, this thesis attempts to identify unknown factors in perovskite formation using various characterization methods described in detail in the following section. To begin with, this thesis concentrates on a major factor in perovskite formation that I discover, the surprising effect of illumination. This thesis goes on to unravel both the mechanism behind and the stages involved in the crystal growth in perovskite films. Furthermore, kinetic monitoring and model fitting bring forward an interesting option to quantify and represent the formation of perovskite under different reaction conditions. While a large part of the work focuses on the above-mentioned areas, the thesis also examines related topics such as changes in the morphology of the perovskite film during storage. A detailed outline of the aspects covered in this thesis is presented in section 1.7.

In practical terms, in order to scrutinize the formation of perovskite through different deposition methods, samples at different points in the formation process are systematically prepared and examined. Using innovative imaging techniques such as scanning electron microscopy (SEM), SEM-cathodoluminescence (CL) and confocal laser scanning fluorescence microscopy (CLSM), the surfaces of forming perovskite films are inspected to establish links between the deposition process and the final perovskite film morphology as well as the film quality. In addition to studying the surface, a novel cross-sectional CLSM imaging technique developed and employed in this thesis opens the door for understanding the properties of perovskites in vertical cross sections of solar cells. This is inevitably

demonstrated while looking into another previously undiscovered aspect of perovskite formation – the directionality of the perovskite formation reaction in a vertical cross section. Thus, the evolution of forming perovskite films as the reaction progresses with time is closely studied. At different points throughout the thesis, the practical implications of our results, for the fabrication of solar cells for instance, are demonstrated. Therefore, this thesis presents new physical insights into fundamentally important aspects of the perovskite formation and these have wide implications for the optoelectronics field.

## 1.6 Characterization techniques

Those characterization techniques frequently used to examine perovskite formation in this thesis will be introduced at this point. Spectroscopic techniques utilized here include ultraviolet (UV)-visible (Vis) absorption spectroscopy, steady-state photoluminescence (PL) spectroscopy and time correlated single photon counting (TCSPC). Next, imaging techniques will be taken up and an important tool used throughout the thesis, CLSM is introduced. SEM and SEM-CL will be described briefly. X-ray diffraction measurements (XRD) will then be taken up. Finally, the solar cell characterization techniques used in this thesis will be discussed.

### 1.6.1 Optical techniques

#### **Absorption measurements**

Steady-state spectroscopic measurements have been widely used in the literature, as they are rapid, contactless and non-destructive. Absorption spectra have been extensively employed to determine the range over which light is absorbed for various materials. Of particular interest is the onset of light absorption. UV-Vis absorption measurements have been used in recent studies of organic-inorganic perovskites[20]. As mentioned earlier, the UV-Vis absorption spectrum of a  $\text{CH}_3\text{NH}_3\text{PbI}_3$  perovskite film has been shown in Figure 1:4a.

#### **Steady-state photoluminescence spectroscopy**

Due to the large potential of perovskites for use in optoelectronic applications, including photovoltaics and light emitting diodes, understanding the emission behaviour of these materials is of considerable importance[51]. Steady-state and time-resolved photoluminescence measurements are often used to evaluate the quality of perovskite films[52] and solar cells[51].

One of the most commonly used measurements is the steady state PL, which can provide information complementary to the absorption spectra discussed earlier. As mentioned earlier in section 1.1, PL involves photo-excitation and the radiative recombination of electron-hole pairs resulting in the

emission of photons of energy corresponding to the band gap of the semiconductor. For perovskites of interest, the photo-excitation is generally achieved using UV light and the emission is detected in the visible or the infra-red region. The steady-state PL spectrum of  $\text{CH}_3\text{NH}_3\text{PbI}_3$  perovskite film has been shown in Figure 1:4b.

The steady-state PL is a convenient option for the swift detection of perovskites of various compositions, thereby different bandgaps, as evident from the report by McMeekin et al.[37]. Moreover, as highly luminescent films are associated with superior film quality[53], the measurement can be used to assess and compare perovskite films. In addition, steady-state PL measurements have been used in the literature to investigate the HTM/perovskite interface. Zhang et al.[54] studied  $\text{CH}_3\text{NH}_3\text{PbI}_3$  perovskite films with different HTMs deposited on top. They found that more than 90% of the PL was quenched when suitable HTMs such as spiro-OMeTAD were used, indicating that efficient charge transfer takes place across the interface, from the perovskite to the HTM.

### **Time correlated single photon counting measurements**

TCSPC measurements, also referred to as time-resolved photoluminescence spectroscopy, can be used to study the photo-physical properties of perovskite films and crystals. In this technique, a light source such as a pulsed laser is used for excitation. From the resulting PL, single photons of a selected wavelength are detected and their arrival times at the detector are measured with respect to the excitation. From the PL decay, the recombination lifetime of charge carriers can be measured. Longer lifetimes are often associated with superior material quality[52]. Several reports in the literature have utilized this technique to compare control samples with those containing additives[55, 56]. Many have demonstrated that superior film quality, achieved through the inclusion of additives, is associated with longer recombination lifetimes. Studies have also focused on employing PL decay measurements to explain the kinetics of recombination in organic-inorganic perovskites[57]. In addition, charge-carrier diffusion constants and diffusion lengths can be assessed using different charge-transport layers through the quenching observed in the PL decay[58].

## **1.6.2 Imaging techniques**

### **Confocal laser scanning fluorescence microscopy**

CLSM is an important imaging tool frequently used in biology, and recently adopted in geology. In this technique, the local emission can be probed point-by-point, thereby generating a two-dimensional map[59]. Figure 1:8 shows a schematic of the central aspects of the technique for imaging a sample surface containing two semiconductors of different bandgaps. In this technique, a beam of laser light used for excitation is focused at one point on the sample and the fluorescence emitted from this point

will be focused on the photodetector. The laser moves in a raster scanning pattern across the x-y plane covering a small area on the surface of the sample. While imaging a sample containing two semiconductors, as the bandgaps are different, the frequency ( $\nu$ ) and the corresponding wavelength of the photoluminescence emitted are also different (Figure 1:8b). Using two detectors simultaneously to collect photons in different ranges of wavelengths, the emission from each semiconductor is detected and digital images are stored as shown in Figure 1:8c. In the image processing stage, diverse pseudocolours are assigned to the two images containing the data from each detector and the images are combined to form a composite, which displays the information collected by both detectors (Figure 1:8d). Therefore, this tool facilitates the localization of different components or semiconductors in a sample based on differences in their emission wavelengths.

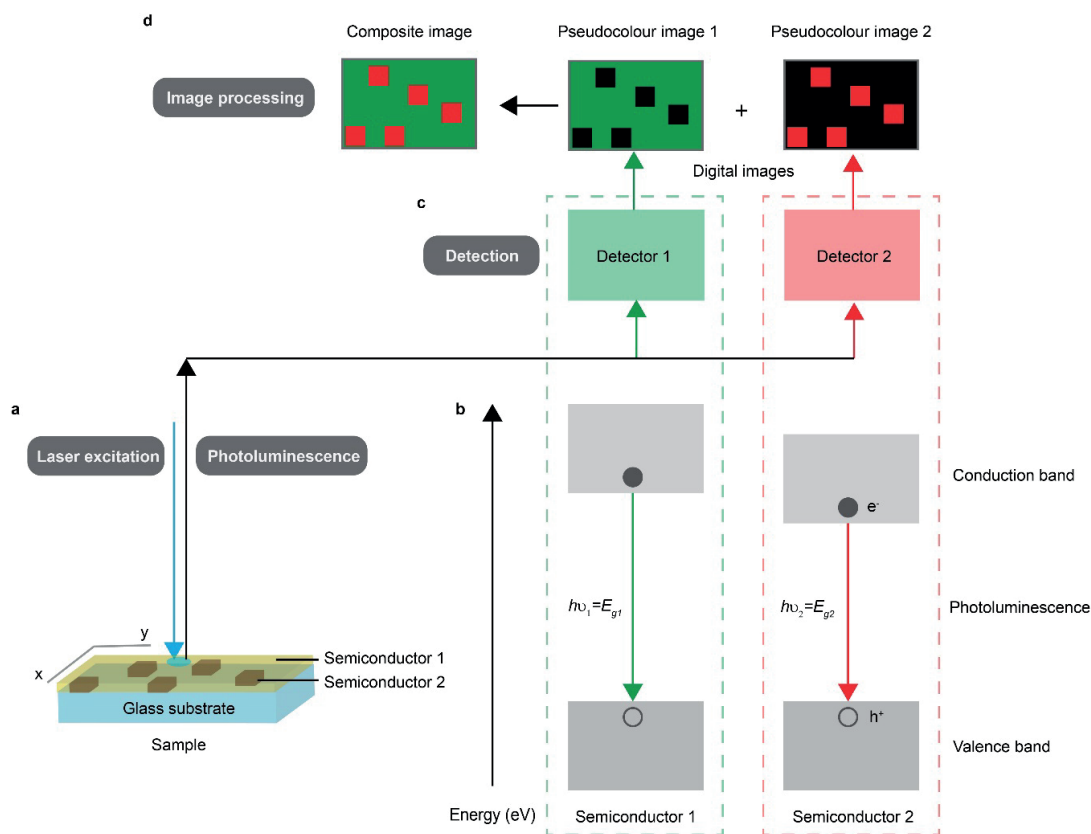


Figure 1:8 Schematic depicting CLSM imaging of the surface of a sample containing two semiconductors of different bandgaps. a, Laser excitation of and photoluminescence from one point as the x-y plane is scanned. b, Energy bands of the semiconductors with photoluminescence at different frequencies. c, Photoluminescence from each semiconductor captured by a different detector and digital images are stored. d, Images are pseudocoloured and combined to form a composite image.

Forming perovskite films are expected to contain a mixture of semiconductors as lead halides, which are constituent components, are also semiconductors. Thus, CLSM is ideal for studying the evolution of the surface of the perovskite film. This technique can also identify emissive intermediates that may be formed during the deposition process. Therefore, CLSM is used in this thesis to study the formation of

perovskite films in sequential deposition[60] (in Chapter 2 and Chapter 3) and in the anti-solvent method[35] (in Chapter 2).

CLSM also has the potential to answer interesting questions that are more challenging to address and cannot be explained using techniques such as SEM and atomic-force microscopy. A new cross-sectional fluorescence imaging technique has been developed and demonstrated to obtain information otherwise inaccessible through the traditional surface imaging technique as described in detail in Chapter 3.

Some studies in the literature have also employed PL imaging techniques. In the study by de Quillettes et al.[52], PL imaging combined with fluorescence lifetime imaging was employed to demonstrate that grains in perovskite films exhibit different PL intensities and lifetimes, in spite of the fact that these films had long bulk lifetimes. It was also used to show the photo-brightening of perovskite films, resulting in enhanced PL[61]. Mastroianni et al.[51] looked into the correlation of the morphology of perovskite films with the photovoltaic performance using PL imaging.

### **Scanning electron microscopy and cathodoluminescence**

Secondary electrons are among the multiple secondary particles generated by the incident high-energy electron beam in SEM. They can be used to obtain information about the topography of samples. In this thesis, secondary electron images (simply referred to as SEM images) are obtained to study the surface of perovskite films.

Another form of luminescence that is produced under high-energy electron bombardment is called CL. It is one of the sub-surface signals generated in SEM while studying luminescent materials such as insulators or semiconductors. CL measurements can be used in a manner similar to CLSM to study samples containing several semiconductors of different bandgaps. Therefore, CL images can provide composition-based contrast, which can offer valuable insights while studying forming perovskite films as mentioned earlier. In some instances in this thesis, using a specialized SEM setup equipped with a CL detector, both SEM and CL images are recorded and superimposed, thereby obtaining a more comprehensive picture of the sample (referred to as SEM-CL images). Therefore, SEM-CL measurements can give spatially resolved compositional information about the surface of perovskite films in high-resolution.

#### **1.6.3 Structural characterization methods**

##### **X-ray diffraction**

Powder diffraction is a powerful and comprehensive technique used to analyse materials in various fields. These measurements provide structural information about crystalline solids not in the form of

single crystals. It is often used for the rapid and non-destructive identification of phase and to obtain unit cell parameters. It can also provide insights into crystallinity, residual stress and texture in samples. In this thesis, powder diffraction measurements are used to study thin films of perovskites that are polycrystalline in nature.

At this point, consider the definition of crystal as published by the International Union of Crystallography which states that it is any solid displaying an essentially discrete diffraction diagram. In this thesis, this definition is considered while using the term 'crystalline'. On the same lines, solids that do not display a discrete diffraction pattern in powder diffraction measurements are henceforth referred to as 'amorphous'.

The profile of the XRD peaks depends on many factors including instrument peak profile, crystallite size and microstrain. The peak width can be determined by identifying the full width at half maximum (FWHM). In this thesis, the FWHM is determined by fitting the peaks to Voigt functions and obtaining the width parameter from the fit. As the presence of small crystallites can cause broadening of the XRD peaks, the FWHM can be used to estimate the average size of crystallites in the perovskite film. This is done using the Scherrer equation[62]:

$$B = \frac{K\lambda}{L\cos\theta}$$

Equation 1:1 – Scherrer equation for estimation of crystallite size[63]

where  $B$  is peak width,  $K$  is the Scherrer constant (taken as 0.89),  $\lambda$  is the wavelength of incident X-rays,  $L$  is the linear dimension of crystallite and  $\theta$  is the Bragg angle.

However, there are limitations in resolving the particle size due to the fact that several factors affect the peak profile as mentioned earlier. The smallest particle that can be detected in measurements in this thesis is estimated to be approximately 10 nm. The peak broadening due to the small size of crystallites is observed up to the upper limit of approximately 100 nm in the measurements here. Beyond this limit, the instrumental contribution dictates the XRD peak width rather than the broadening due to crystal size.

#### 1.6.4 Solar cell characterization

In order to evaluate the photovoltaic performance of perovskite solar cells in this thesis, current density–voltage (J–V) and incident-photon-to-electron conversion efficiency (IPCE) measurements were employed. Before delving into the details of these measurements, the solar spectrum used for the J–V measurements will be discussed. Consider that the direct radiation that reaches the ground passes through the atmosphere or the air mass (AM) above it. The radiation at sea level when the sun is

directly overhead is called the AM1 Direct while the extra-terrestrial one is called AM0 since it does not pass through any air. While defining the standard terrestrial solar spectrum, denoted AM1.5G, a solar zenith angle of  $48.19^\circ$  is taken, which corresponds to an AM of 1.5 under specific atmospheric conditions. The incident plane is a sun-facing inclined plane tilted at  $37^\circ$  towards the equator. For the AM1.5G standard, both direct and diffuse light are taken into account and the integrated irradiance is  $1000 \text{ Wm}^{-2}$ [64].

### J-V measurements

The performance of a solar cell is evaluated through J-V measurements. Different external potentials are applied to the solar cell and the current response is measured. These measurements are conducted in the dark and under illumination. Certain terms are defined for different conditions of the solar cell during the potential sweep. The open-circuit potential ( $V_{oc}$ ) is defined as the applied external potential bias at which the measured current is zero. The short circuit current density ( $J_{sc}$ ) is the current density at which the applied potential is zero volt. These parameters have been indicated in Figure 1:9.

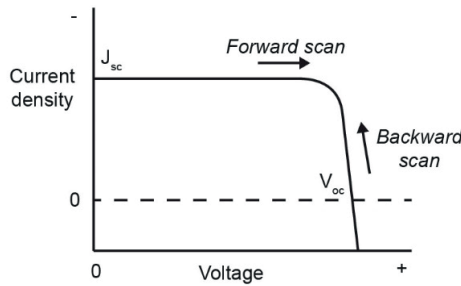


Figure 1:9 A typical example of a J-V measurement of a solar cell measured under illumination.

The power output of the solar cell is a function of the applied potential bias. It increases as the potential increases from zero, passes through a maximum ( $P_{max}$ ) and then decreases as the potential approaches the  $V_{oc}$ . The maxima of the power curve is called the maximum power point (MPP) and the voltage for this point is designated the  $V_{MPP}$ , while the current density at this point is termed the  $J_{MPP}$ . An important aspect while evaluating the solar cell is the fill factor (FF) which is defined as:

$$FF = \frac{J_{MPP} V_{MPP}}{J_{SC} V_{OC}}$$

Equation 1:2 – Equation for fill factor

The power conversion efficiency (PCE) is the fraction of maximum electric power output generated to the incident power:

$$PCE = \frac{P_{max}}{P_{in}} = \frac{J_{sc} V_{oc} FF}{P_{in}}$$

Equation 1:3 – Expression for PCE

At this point, the problem of hysteresis faced in the characterization of perovskite solar cells will be discussed. While performing J–V measurements, the voltage can be either swept from  $V_{oc}$  to zero (called the backward sweep) or from zero to  $V_{oc}$  (called the forward sweep). Both these scan directions are indicated in Figure 1:9. It has been reported that the J–V characteristics obtained for perovskite solar cells are highly dependent on the parameters of the scan. These parameters include the scan speed, operation point before the scan and scan direction. For instance, this phenomenon of hysteresis results in the different PCE for the forward and backward scan directions. So far, this phenomenon has been attributed to very slow electronic and ionic processes taking place in timescales in the order of seconds to minutes[65]. Reports indicate that perovskites have surprisingly high ionic conductivity. This is likely to be the reason behind the polarization observed in perovskite solar cells during their operation that affects charge carrier transport resulting in hysteresis[66, 67]. Thus, J–V measurements in this thesis were conducted keeping the phenomenon of hysteresis in mind and the scan parameters are clearly mentioned.

### Incident-photon-to-electron conversion efficiency measurements

IPCE or the external quantum efficiency is the ratio of the number of electron-hole pairs extracted in the number of photons incident on the active area of the solar cell. It is obtained by measuring the photocurrent under monochromatic illumination (of wavelength  $\lambda$ ) as indicated by Equation 1:4. In this thesis, the IPCE is measured under short-circuit conditions.

$$IPCE(\lambda) = \frac{n_{electrons}(\lambda)}{n_{photons}(\lambda)} = \frac{\frac{I(\lambda)}{e}}{\frac{P_{in}(\lambda)}{h\nu}} = \frac{I(\lambda)}{P_{in}(\lambda)} \frac{hc}{e\lambda}$$

Equation 1:4 – Expression for IPCE

where  $h$  is the Planck constant,  $c$  is the speed of light and  $e$  is the elementary charge.

## 1.7 Outline and organization of the thesis

Given the previously mentioned objectives and experimental approach, the first step is systematically looking at the formation of the perovskite through the sequential deposition method. During preliminary studies, I discovered the unexpected effect of illumination on perovskite formation. I focus on this effect of illumination and elucidate its mechanism in Chapter 2 of this thesis. The main finding of this study is that illumination greatly influences perovskite formation by affecting the nucleation.



Thus, illumination during film formation proves to be an important factor in the reaction that now enables tuning of the morphology of the resulting perovskite film. Moreover, it has a robust effect on perovskite formation in both the sequential deposition and the anti-solvent method, as well as for different perovskite compositions. I also make use of CLSM to study the formation of perovskites of these complex compositions prepared using the anti-solvent method.

While I investigate the effect of illumination in Chapter 2, a comprehensive picture of the sequential deposition is still lacking. A systematic study of the reaction in sequential deposition would shed some light on the salient aspects of the perovskite formation and bring forward the crucial aspects of the kinetics involved. In Chapter 3, I scrutinize the reaction and present a much-needed fundamental understanding of the formation process and its different stages. After careful analysis of kinetic data from a variety of experimental conditions, I identify that the Avrami models explain the nucleation and crystal growth. The cross-sectional CLSM imaging demonstrated here for the first time reveals previously undiscovered aspects of perovskite formation and opens the door for understanding the properties of perovskites in vertical cross sections of solar cells. The ability of CLSM to provide compositional information by exploiting the difference in emission for different semiconductors is extremely valuable in the perovskite field.

Chapters 2 and 3 describe the formation of perovskite through various deposition methods. It is also interesting to take a closer look at spontaneous changes in the perovskite thin film in completely prepared solar cells during storage. This follows as the next logical step after studying perovskite formation and morphological control using illumination in the chapters 2 and 3. Thus, I specifically look into the dynamic nature of the morphology of prepared perovskite films and complete solar cells. I find that smaller crystallites within perovskite films spontaneously coalesce into larger ones when solar cells are stored in the dark under dry air. Chapter 4 describes this phenomenon of coalescence of perovskite crystals and the improvement it brings about in the performance of high efficiency solar cells. Last but not the least, Chapter 5 outlines the main conclusions of the thesis and the future scope of the work described in the thesis.



## Chapter 2 The effect of illumination on the formation of perovskite films

*This chapter was adapted from the following articles with the permission of all co-authors and journals.*

**Postprint version of the article:** [A. Ummadisingu](#), L. Steier, J.-Y. Seo, T. Matsui, A. Abate, W. Tress and M. Grätzel, "The effect of illumination on the formation of metal halide perovskite films," *Nature*, vol. 545, pp. 208-212, May 11 2017. (doi: 10.1038/nature22072)

**My contribution:** Conceptualized and designed the study, analysed the data and prepared the manuscript. Prepared the samples and devices using sequential deposition and conducted the experiments. Captured and processed the CLSM images. Conducted the electrochemical experiments with L.S. Prepared the  $\text{CH}_3\text{NH}_3\text{PbI}_3$  devices using the anti-solvent method with T.M. and A.A.

**Postprint version of the article:** M. Saliba, T. Matsui, K. Domanski, J. Y. Seo, [A. Ummadisingu](#), S. M. Zakeeruddin, J.P. Correa-Baena, W. R. Tress, A. Abate, A. Hagfeldt and M. Grätzel, "Incorporation of rubidium cations into perovskite solar cells improves photovoltaic performance," *Science*, vol. 354, pp. 206-209, Oct 14 2016. (doi: 10.1126/science.aah5557)

**My contribution:** Captured and processed the CLSM images. Conducted SEM, PL and XRD measurements on the perovskite films with M.S., J.-Y.S. and J.-P. C.-B.

This chapter describes the discovery of the light effect on the formation of perovskite in the sequential deposition and anti-solvent methods. The aim is to study the sequential deposition method in detail, and unravel the mechanism behind the unexpected light effect. This chapter also makes use of CLSM to look into the formation of perovskites of complex compositions prepared using the anti-solvent method.

### 2.1 Introduction

Optimizing perovskite film morphology is a key consideration to improve solar cell performance[33], as film homogeneity correlates with superior photovoltaic performance[49, 50]. Many device architectures and processing techniques have been explored to achieve high performance[18], including single-step deposition[23], sequential deposition[31, 32] and anti-solvent methods[33, 34]. Preceding studies have looked into the influence of experimental conditions on film quality[50], such as the concentration of the reactants[68, 69] and the reaction temperature[70]. However to date, the precise mechanism of the reaction and the main factors governing the reaction are poorly understood. This lack of control is the main reason for the large variability observed in perovskite morphology and the related solar cell performance[49, 50].

In this chapter, we show that light has a major influence on the rate of perovskite formation and film morphology in the two main deposition methods currently employed. Using CLSM and SEM, we show that  $\text{PbI}_2$  crystallizes before the intercalation of MAI commences, producing methylammonium lead

iodide perovskite. We find that the formation of perovskite *via* such a sequential deposition is highly accelerated by light. The influence of light on morphology is reflected in a twofold enhancement in solar cell efficiency. Conversely, for the anti-solvent method, we reveal that the best photovoltaic performance is obtained when films are produced in the dark. The discovery of light-activated crystallization not only identifies a previously unknown source of variability in opto-electronic properties, but also opens up new ways of tuning morphology and structuring perovskites for various applications. Finally, various perovskite compositions developed through the anti-solvent method for achieving high solar cell efficiencies are compared with the aim of gaining insights into the differences that composition induces in the perovskite formation.

## 2.2 Results and discussion

### 2.2.1 Conversion in the dark and under illumination

To begin with, we demonstrate the effect of light on perovskite formation in sequential deposition. In this method,  $\text{PbI}_2$  is deposited onto a mesoporous  $\text{TiO}_2$  scaffold, followed by dipping in a MAI solution to convert it to the methylammonium lead iodide perovskite. We monitor the reaction of  $\text{PbI}_2$  films with a  $6 \text{ mg ml}^{-1}$  MAI solution in 2-propanol, both in the dark and under 1 Sun illumination (white Light-Emitting Diode (LED) array supplying approximately  $100 \text{ mWcm}^{-2}$ ), using CLSM to image samples at different dipping times. CLSM spatially maps the emissive chemical constituents by exploiting the differences in their emission spectra. We attribute the emission between 500 and 550 nm to  $\text{PbI}_2$ [71] and assign a green colour to it, while we map the emission between 700 and 800 nm in red colour, attributed to the perovskite[69].

We take up the case of the reaction in the dark, starting with an unreacted  $\text{PbI}_2$  film and progressing to samples at incremental dipping times in the MAI solution. As seen in the CLSM image and the corresponding SEM insert in Figure 2:1a, the freshly spin-coated  $\text{PbI}_2$  film shows no distinct features that can be attributed to crystals. According to the literature[72], crystalline metal halides show stronger luminescence when compared with amorphous components. Spots with a prominent  $\text{PbI}_2$  emission, distinguishable from the surrounding  $\text{PbI}_2$ , are observed in the CLSM image of a sample dipped for 6 s (Figure 2:1b). They correspond in size and shape (hexagonal platelets characteristic of the 2H polytype of  $\text{PbI}_2$ [73-75]) to the crystals seen in the SEM insert, indicating that  $\text{PbI}_2$  crystallizes before the formation of perovskite.

Only with an increased dipping time, do we detect small amounts of perovskite (shown in red), present in the central parts of the crystalline  $\text{PbI}_2$  clusters, in the CLSM image of a sample dipped for 8 s (Figure 2:1c). This indicates that the onset of intercalation[31, 73, 76] of MAI into the  $\text{PbI}_2$  crystals

occurs subsequent to the crystallization of  $\text{PbI}_2$ . This is followed by structural reorganization which results in  $\text{PbI}_2$ -perovskite mixed crystals. These observations have so far never been reported. The progress of the intercalation is apparent in Figure 2:1d and Figure 2:1e, which show a sample dipped for 10 and 60 s, respectively.

We then study the CLSM images of samples dipped under full sun illumination (Figure 2:1f-Figure 2:1i). Comparing these images with those obtained from samples made in the dark, we notice major differences. Firstly, we observe that the intercalation commences and ends much earlier under illumination, indicating that the rate of perovskite formation is greatly increased. Secondly, the crystals are smaller and more in number under illumination. Thirdly, we observe that samples dipped under illumination (Figure 2:1i and Figure 2:1h) show an increase in the number of non-emissive regions, in correlation with the dipping time. However, SEM images (inserts) show full surface coverage in contrast to samples made in the dark, confirming that the non-emissive regions are not gaps in the film. Instead, they are attributed to perovskite grains with more defects and trap states, as reported by deQuilettes et al.[52]. Finally, morphological changes are observed in the perovskite film upon dipping beyond the point of complete conversion (Figure 2:1e and Figure 2:1i). These are partly due to the coarsening process known as Ostwald ripening, as reported in the literature on perovskite films[77]. This phenomenon will be discussed in detail in Chapter 3.



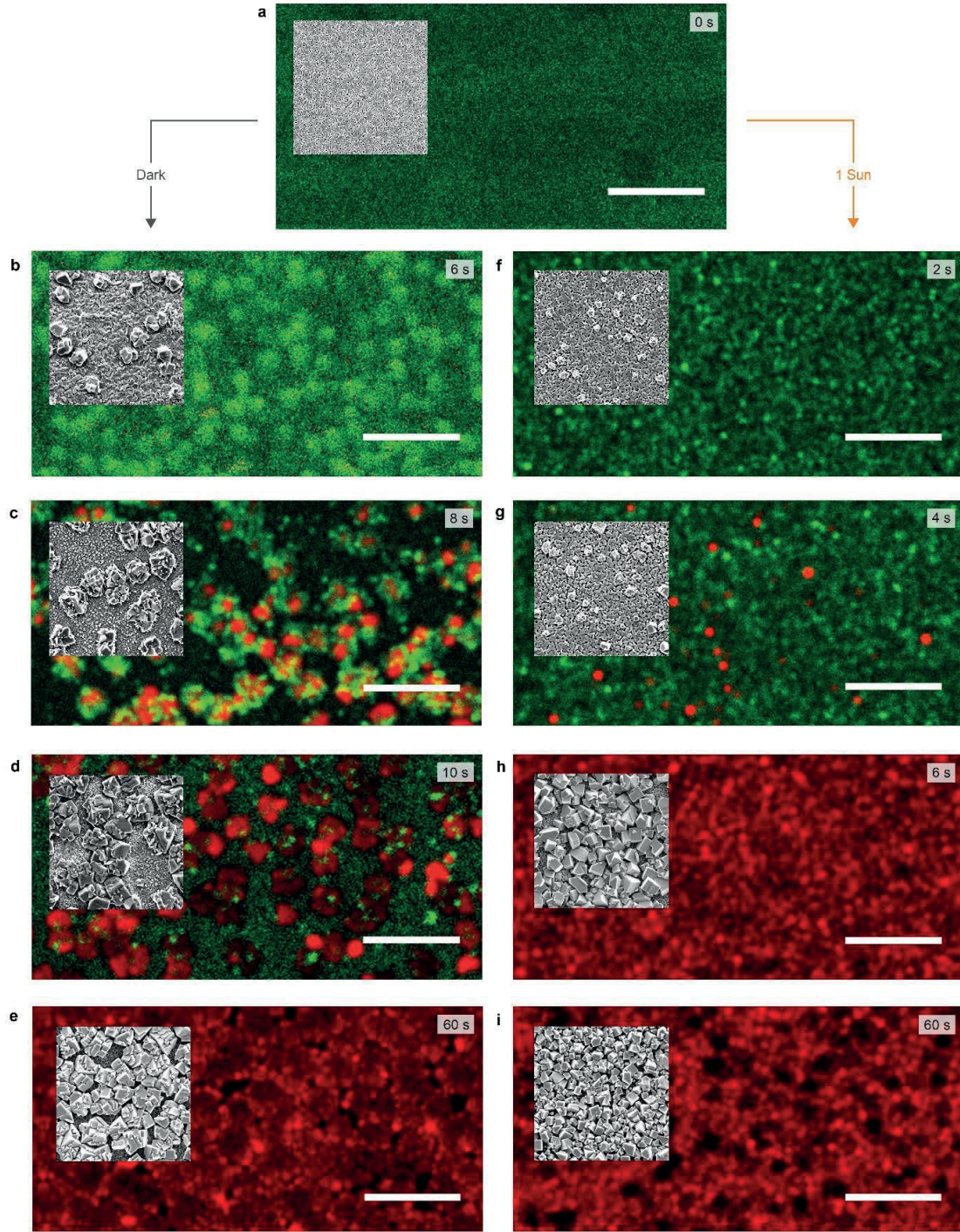


Figure 2:  $\text{CH}_3\text{NH}_3\text{PbI}_3$  formation in sequential deposition in the dark and under 1 Sun illumination. In these CLSM images, the emission between 500 and 550 nm attributed to  $\text{PbI}_2$ [71] is assigned a green colour, while the emission between 700 and 800 nm is attributed to perovskite[69] and assigned a red colour. Colour saturation scales with emission intensity. a, Unreacted  $\text{PbI}_2$  film. b–e, Sample dipped in MAI solution for respectively 6, 8, 10 and 60 s in the dark. f–i, Sample dipped for respectively 2, 4, 6 and 60 s under a light intensity of 1 Sun. Note the shorter dipping times in the right-hand column (under illumination) than in the left (in the dark). Insets show SEM images. All scale bars show 5  $\mu\text{m}$ , and are applicable to both CLSM and SEM images.

### 2.2.2 Nucleation mode and density

It is interesting to classify the nucleation in our system based on the nucleation mode, the class and the phases involved. However, from the discussion so far, it is clear that the formation of perovskite in sequential deposition is a complex system. Moreover, as discussed in detail subsequently, we deal with a specific case that deviates from the classical cases described in the previous chapter. Therefore, the crystallization observed in this process is interpreted by applying a certain level of abstraction to the system, while care is taken to include defining aspects of the system that may affect the explanation.

At this point, we look into identifying the nucleation mode in the  $\text{PbI}_2$  film. The images of the dark case presented in Figure 2:1b, Figure 2:1c and Figure 2:1d show that the number of crystals does not increase after the initial nucleation. This indicates instantaneous nucleation such that new nuclei do not form after the initial seconds of dipping. Therefore, we identify the nucleation mode in  $\text{PbI}_2$  as saturation by pre-existing nuclei as defined at the beginning of the chapter. It is likely that we have the formation of a finite number of potential nuclei during the  $\text{PbI}_2$  deposition step[47]. This can be understood considering the thermal history of the  $\text{PbI}_2$  film. The rapid drying of the film, which was deposited at 70 °C, results in a film that has both amorphous domains and minute crystalline clusters of  $\text{PbI}_2$ [47, 73]. Such a film is metastable at lower temperatures, with an affinity to crystallize further[47]. These crystalline clusters are the potential nuclei that possess the capacity to grow instantaneously upon exposure to an MAI solution by consuming the amorphous component, prior to converting into perovskite. As the nucleation occurs due to the presence of crystals of the material being crystallized, we classify the nucleation of  $\text{PbI}_2$  in our system as secondary nucleation[78]. Interestingly, we observe that well-annealed  $\text{PbI}_2$  films do not show a high nucleation density as they lack the amorphous component needed for the nuclei to grow (see Figure 2:2 for SEM images and X-ray diffraction analysis).

Before we investigate the mechanism of the light-activated nucleation, we quantify the effect of the light intensity. We captured SEM images of samples dipped for 25 s in the dark, and under light intensities of 0.001, 0.01, 0.1 and 1 Sun, as shown in Figure 2:3a. The count of  $\text{PbI}_2$ -perovskite mixed crystals for each sample (Figure 2:3b), corresponds to the nucleation density in each case, since  $\text{PbI}_2$  exhibits instantaneous nucleation. While the nucleation density is low in the dark, it increases logarithmically with the light intensity present during dipping, thus confirming the occurrence of light-activated nucleation.



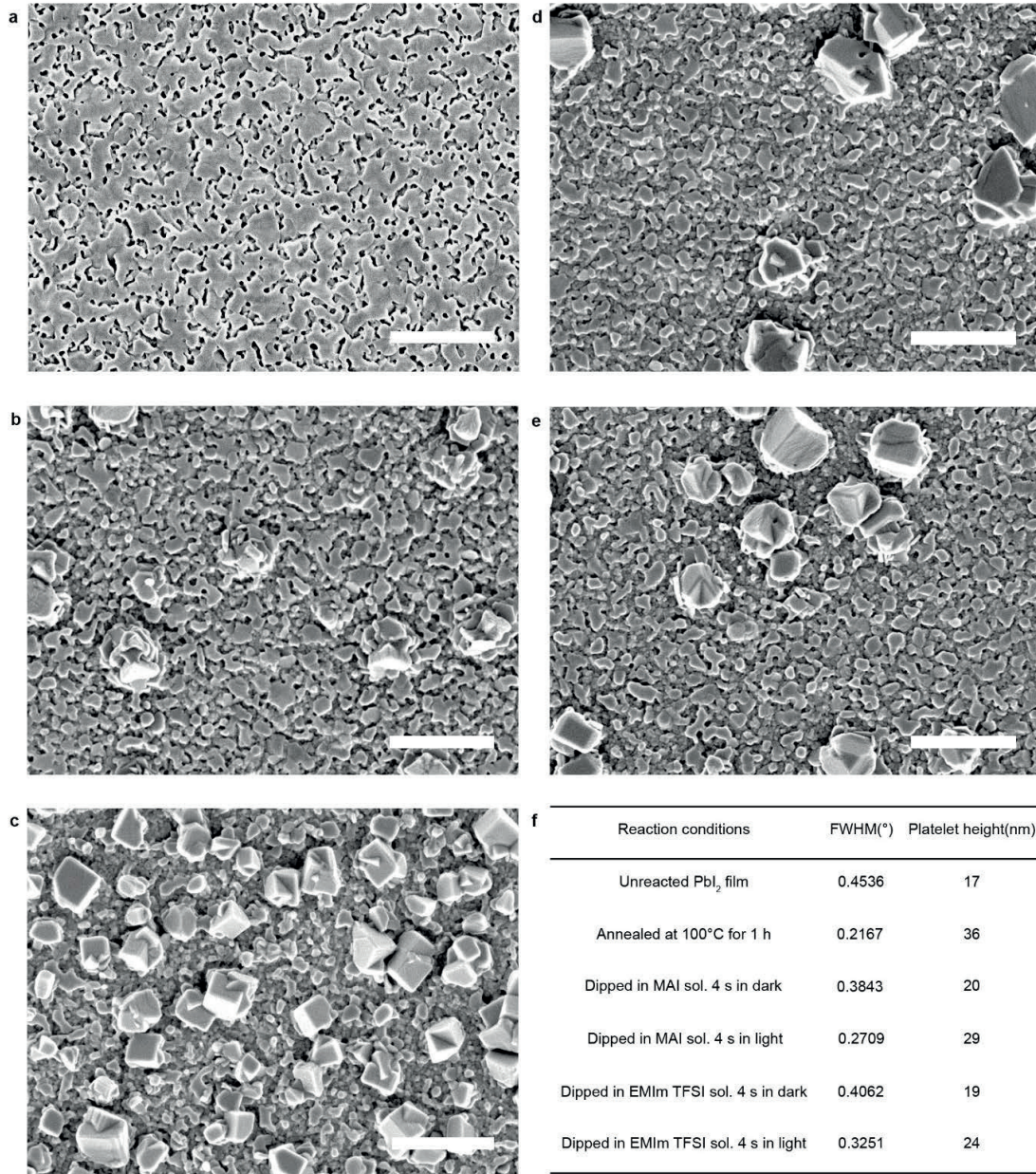


Figure 2:2 Growth of  $\text{PbI}_2$  nuclei under different conditions in sequential deposition. a, SEM image showing a standard unreacted  $\text{PbI}_2$  film (as-deposited). b, c, SEM images of standard  $\text{PbI}_2$  films dipped in MAI solution for 4 s: in the dark showing low crystal density (b) and under 1 Sun light intensity showing high crystal density (c). d, e, SEM images of  $\text{PbI}_2$  films annealed at 100 °C for 1 h, dipped in MAI solution for 4 s: in the dark (d) and under 1 Sun light intensity (e). Scale bars (a–e), 1  $\mu\text{m}$ . It is interesting to compare samples made under 1 Sun light intensity, as the light-activated nucleation is expected to take place and the affinity for nucleation can be assessed. Image (e) shows a sample of initially high crystallinity with substantially fewer crystals growing on the surface after dipping, compared to the analogous standard sample in (c), indicating that amorphous  $\text{PbI}_2$  is required for the growth of nuclei. f, XRD analysis showing the full-width at half-maximum (FWHM) of the Voigt function fits of the (001) reflection of the 2H polytype of  $\text{PbI}_2$  and the corresponding height of the platelet obtained using the Scherrer equation. We observe an increase in platelet height from 17 nm to 36 nm on annealing the standard  $\text{PbI}_2$  sample at 100 °C for 1 h. The platelet height increases from 17 nm in the standard unreacted  $\text{PbI}_2$  film, to 20 nm and 29 nm, on dipping in 0.038 M MAI in 2-propanol in the dark and under 1 Sun illumination, respectively. On dipping standard  $\text{PbI}_2$  films in 0.038 M EMIm TFSI in 2-propanol (for equivalence with 0.038 M MAI in 2-propanol), an increase in the platelet height from 17 nm to 19 nm and 24 nm was observed, for dipping in the dark and under 1 Sun, respectively. This is similar to the trend seen for dipping in MAI. See Materials and methods for details.



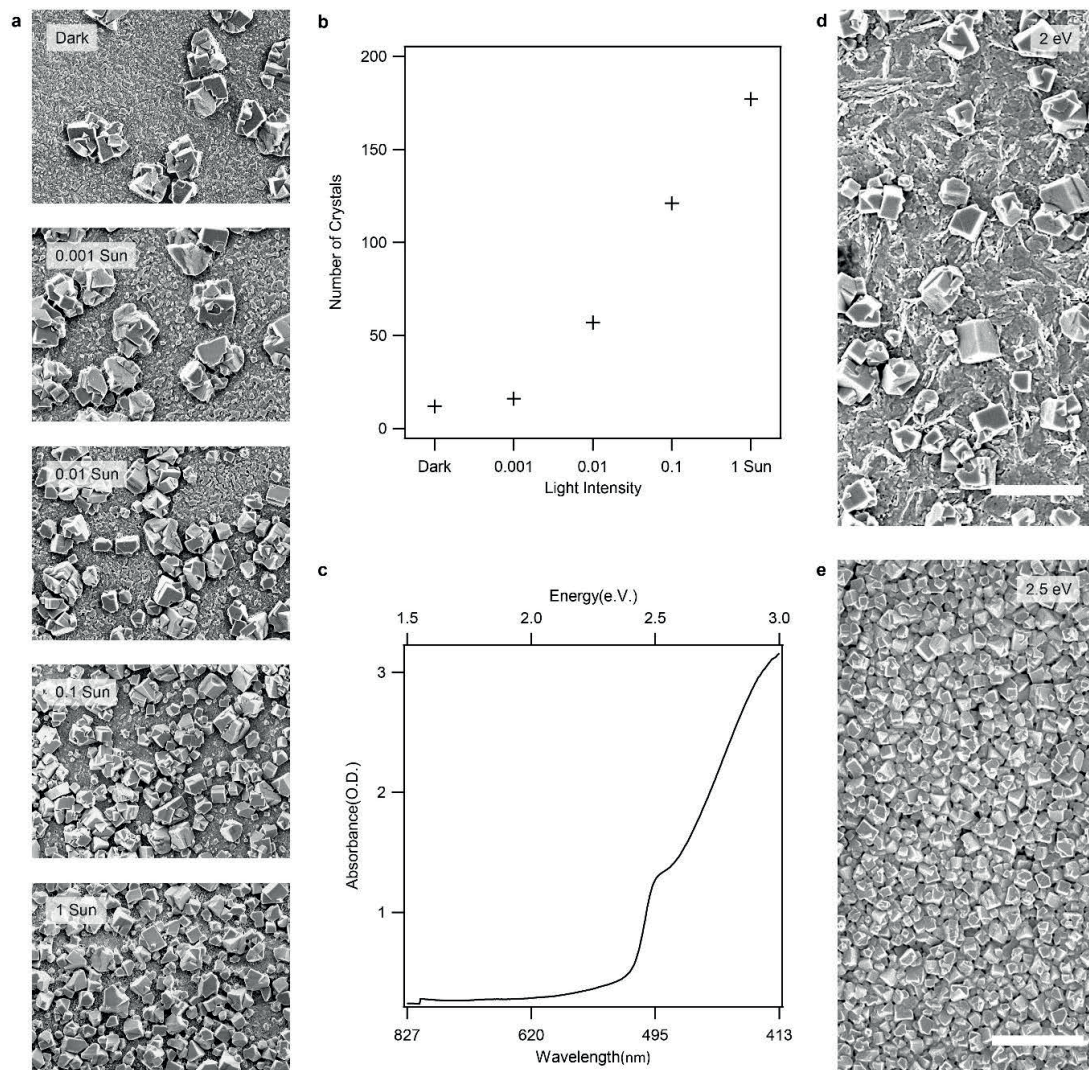


Figure 2:3 Nucleation density under different illumination conditions. a, From top to bottom, SEM images of samples dipped in MAI solution for 25 s in the dark, under 0.001 Sun, 0.01 Sun, 0.1 Sun and 1 Sun. Imaged regions are  $10\ \mu\text{m} \times 7\ \mu\text{m}$ . b, Number of  $\text{PbI}_2$ -perovskite mixed crystals identified from the images shown in (a). c, Absorbance spectrum of an unreacted  $\text{PbI}_2$  film (OD, optical density). Absorption tail states (the 'Urbach tail'), attributed to inherent disorder of the material, are visible. d, SEM image of sample dipped for 25 s under monochromatic illumination of 2.0 eV. e, As (d), but under monochromatic illumination of 2.5 eV. Scale bars (d, e), 2.5  $\mu\text{m}$ .

We considered the possibility that heating due to illumination is the cause of the light-activated nucleation. However, using evidence from a variable temperature and variable light study, we rule out this possibility. By comparing samples made under either 0.01 Sun or 1 Sun light intensity, we see that perovskite formation at higher temperatures results in large crystals due to a higher growth rate (Figure 2:4). This is contrary to the light effect that enhances nucleation and gives numerous small crystals, as observed upon comparing samples made under 0.01 Sun and 1 Sun at the same temperature (Figure 2:3, Figure 2:4). Thus, this also rules out the possibility of illumination changing

the growth rate rather than the nucleation step. Consequently, we attribute the light-activated nucleation to the generation of electron-hole pairs, rather than a thermal phenomenon.

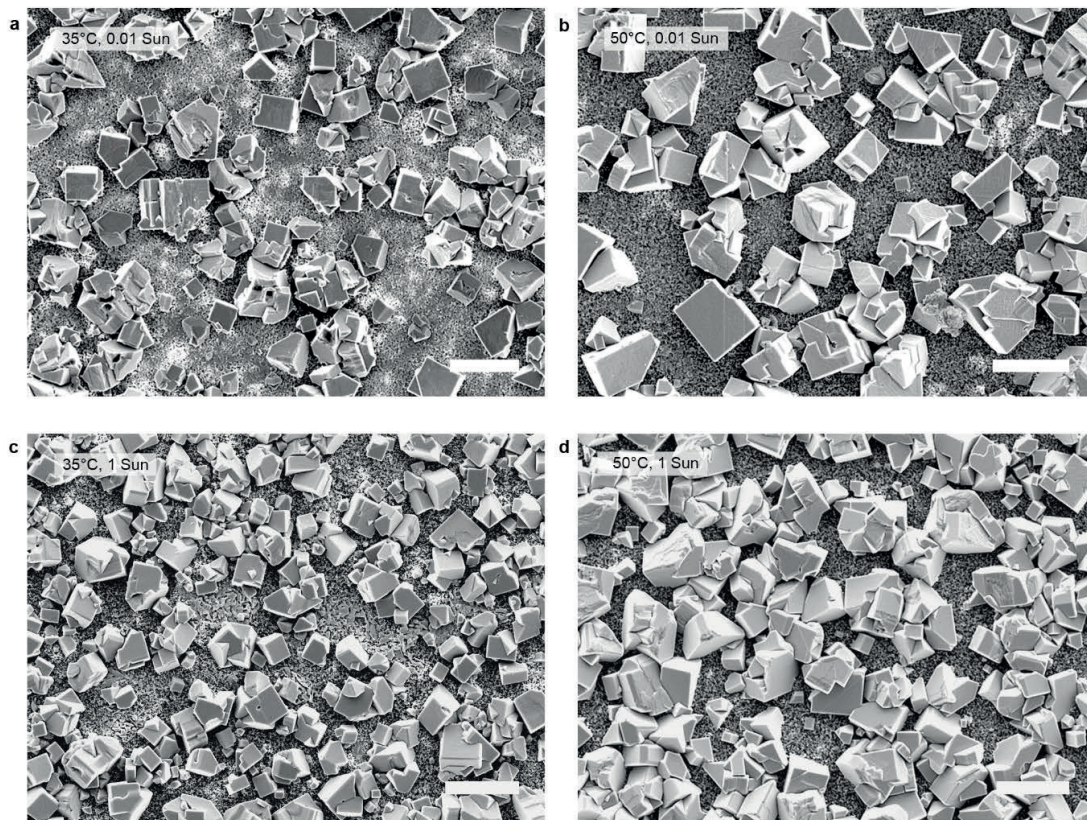


Figure 2:4 SEM images of  $\text{CH}_3\text{NH}_3\text{PbI}_3$  films prepared using sequential deposition under various temperature and light conditions.  $\text{PbI}_2$  films were dipped isothermally in MAI solution for 25 s at the following conditions: a, 35 °C under 0.01 Sun illumination; b, 50 °C under 0.01 Sun; c, 35 °C under 1 Sun; and d, 50 °C under 1 Sun. Dipping at a higher temperature and the same light intensity gives larger perovskite crystals; dipping at a higher light intensity and the same temperature gives a higher nucleation density with small crystals. Scale bars (a–d), 2  $\mu\text{m}$ .

To verify whether photo-generated electron-hole pairs enhance nucleation, we investigate the effect of the photon energy in correlation with the absorbance of a  $\text{PbI}_2$  film. The absorbance of a  $\text{PbI}_2$  film is shown in Figure 2:3c. We consider two photon energy values, 2.0 eV and 2.5 eV, chosen to be on either side of the absorption onset. Samples were dipped in an MAI solution under both conditions of monochromatic illumination. The SEM images of samples dipped for 25 s under these monochromatic illumination conditions are shown in Figure 2:3d and Figure 2:3e respectively. Comparable photon fluxes were used in these experiments. They demonstrate that a higher nucleation density is attained upon above-gap illumination, indicating that photons absorbed by the  $\text{PbI}_2$  and generating electron-hole pairs enhance nucleation.



### 2.2.3 Mechanism of light-activated nucleation

#### Photo-electrochemical experiments characterizing the $\text{PbI}_2$ -electrolyte interface

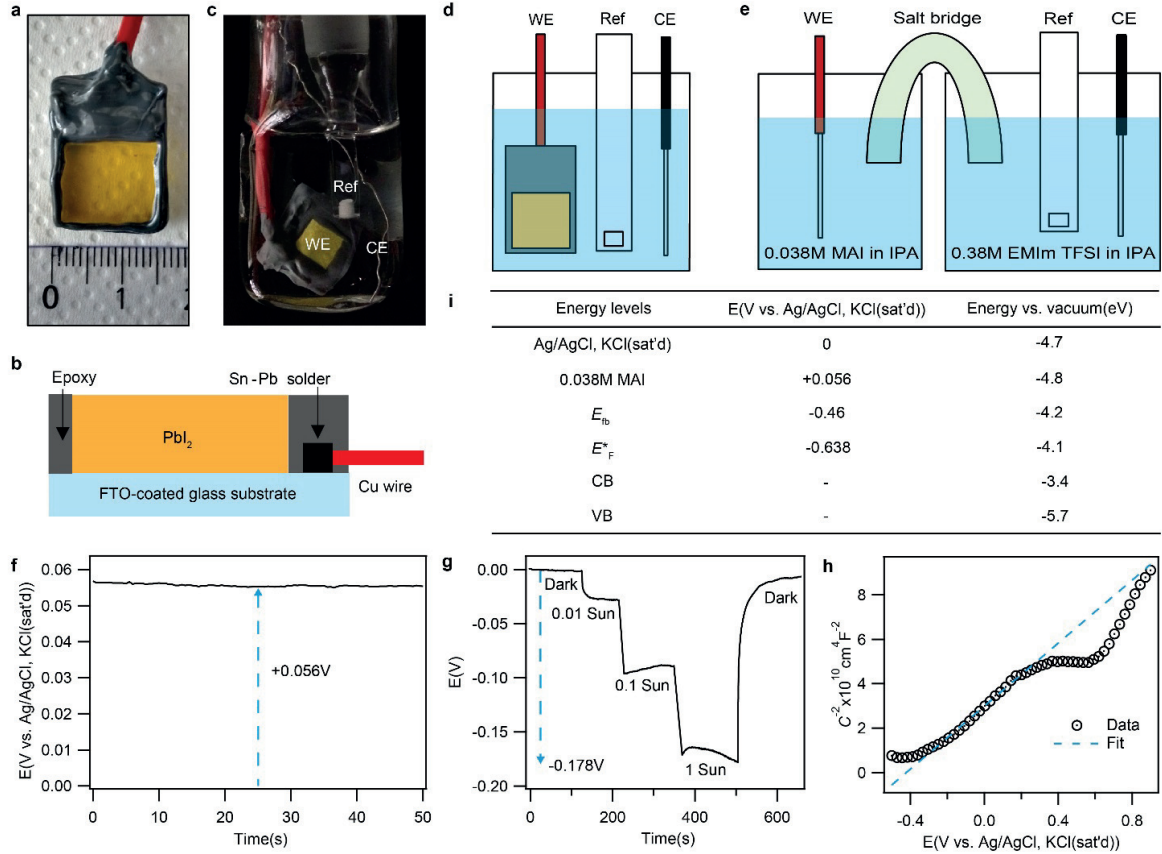


Figure 2.5 Electrochemical experiments. a, b, Photograph (a) and cross-sectional diagram (b) of a  $\text{PbI}_2$  electrode. c, d, Photograph (c) and diagram (d) of set-up with a  $\text{PbI}_2$  electrode in contact with 0.38 M EMIm TFSI in 2-propanol, used for chopped light chronopotentiometry and EIS measurement. WE, working electrode; Ref, reference electrode; CE, counter electrode. e, Diagram of set-up used to determine the chemical potential of the MAI solution in 2-propanol (IPA) solution, and f, the corresponding chronopotentiometry experiment data. The chemical potential of the MAI solution was determined to be +0.056 V versus Ag/AgCl, KCl (saturated). g, Variable light chronopotentiometric photo-voltage measurement at zero applied current (dark, 0.01 Sun, 0.1 Sun, 1 Sun and dark). The potential under the initial dark condition is set to zero. h, Mott-Schottky analysis of  $\text{PbI}_2$  film in the dark, where  $C$  is the space-charge layer capacitance normalized by the area considering a geometrically flat surface (Equation 2:4). A flat band potential ( $E_{fb}$ ) of -0.46 V versus Ag/AgCl, KCl (saturated) was determined from the x-intercept of a fit of the linear region. The upper limit of the charge carrier concentration ( $N_D$ ), considering a geometrically flat surface, was obtained as  $8 \times 10^{19} \text{ cm}^{-3}$ . i, Energy levels versus Ag/AgCl, KCl (saturated) and the equivalent value versus the vacuum level shown. The Ag/AgCl, KCl (saturated) reference electrode was calibrated by dissolving ferrocene (Fc) in the ionic liquid solution and verifying that the position of the  $\text{Fc}/\text{Fc}^+$  couple was +0.4 V versus Ag/AgCl, KCl (saturated), consistent with the literature[79]. The energy levels determined from f, g and h are shown. Electron-quasi-Fermi level under illumination is denoted by  $E_F^*$ . Reported values[80] for the conduction band (CB) and valence band (VB) edges of  $\text{PbI}_2$  are also shown.

To investigate the mechanism through which absorbed light enhances the nucleation of  $\text{PbI}_2$ , we performed photo-electrochemical experiments. First, we determined whether a crystalline  $\text{PbI}_2$  film was photoactive. We used a 0.38M solution of the ionic liquid 1-ethyl-3-methylimidazolium bis(trifluoromethylsulfonyl)imide (EMIm TFSI) in 2-propanol and conducted chopped light chronopotentiometry at zero applied current. Crystalline films were used to improve stability during measurement. We used an ionic liquid solution instead of an MAI solution to avoid perovskite

formation during our experiment. This approach is justified since the ionic liquid solution provides a similar ionic environment as MAI. We show that the  $\text{PbI}_2$  crystallizes in a solution of the ionic liquid, akin to that in a MAI solution (see Figure 2:2 for XRD analysis).

The photo-voltage measured under 1 Sun is -0.178 V, which confirms that the film is photoactive (Figure 2:5g). Moreover, the larger negative value under light compared to that in the dark indicates that the  $\text{PbI}_2$  film is of n-type. The second aspect of interest is the transient behaviour seen in the potential upon switching from 1 Sun to the dark. The potential is persistent, indicating that some generated charges are very long-lived and recombine slowly, possibly due to trapping or accumulation at the  $\text{PbI}_2$ -electrolyte interface.

To further characterize the  $\text{PbI}_2$ -electrolyte interface, we conducted electrochemical impedance spectroscopy (EIS) measurements in the dark (see Figure 2:5 for experimental setups). The Mott-Schottky plot, shown in Figure 2:5h, has a positive slope, which confirms that the  $\text{PbI}_2$  film is an n-type semiconductor[81]. The flat band potential was determined as -0.46 V vs. Ag/AgCl, KCl (sat'd) (calibrated with ferrocene). We observe that the capacitance becomes independent of potential between +0.2 and +0.6 V vs. Ag/AgCl, KCl (sat'd), indicative of Fermi level pinning at the  $\text{PbI}_2$ -electrolyte interface. The pinning points to the presence of surface traps, which are located below midgap. Energy band diagrams of  $\text{PbI}_2$  film and MAI solution, in the dark and under illumination are presented in Figure 2:6. (A table containing the energy levels is also shown in Figure 2:5i.) Below, we further discuss the role of these traps in the light-activated nucleation.

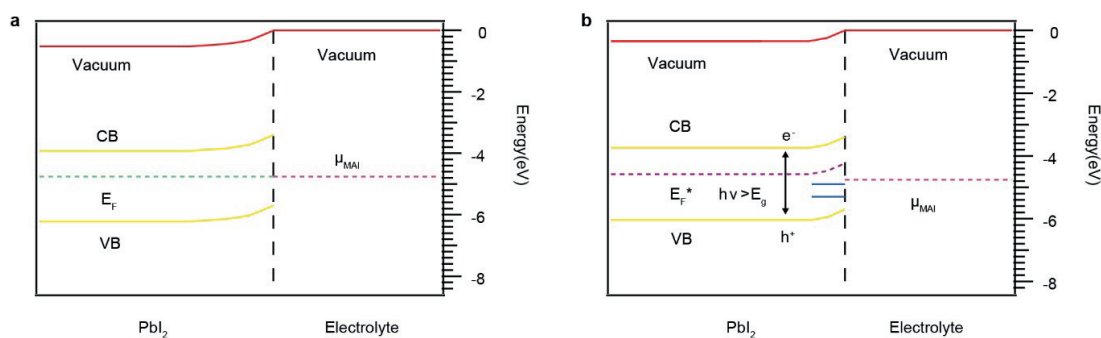


Figure 2:6 Energy band diagrams of  $\text{PbI}_2$  film and 0.038 M MAI in 2-propanol solution in the dark and under 1 Sun illumination. Diagrams constructed using data from Figure 2:5i and band bending assumed in both cases.  $E_F$ , Fermi level;  $\mu_{\text{MAI}}$ , chemical potential of the electrolyte (MAI solution). a, In the dark, after contact and electrostatic equilibration, and b, under 1 Sun illumination, with the limits of surface traps obtained from the Mott-Schottky analysis shown in blue. Quasi Fermi level for holes not shown.

### Mechanism behind the nucleation in the dark and under illumination

At this point, we propose a mechanism for the secondary nucleation of the  $\text{PbI}_2$  film, both in the dark and under illumination. The crucial thermodynamic factors in nucleation are the critical free energy of

nucleation ( $\Delta G^*$ ), which is the height of the nucleation barrier or the work of formation of the critical nucleus, and the critical cluster size ( $N^*$ ). They can be described using Equation 2:1[82] and Equation 2:2[82] in the case of homogeneous nucleation in solids. While heterogeneous nucleation may be a more appropriate description of our system, for simplicity we take up the equations for the homogeneous case. We interpret them by considering the unusual contact with the MAI, as discussed later.

$$\Delta G^* = \frac{4}{27} \frac{(\sum_i \eta_i \Gamma_i)^3}{(\mu_2 - \mu_1)^2}$$

Equation 2:1 – Expression for the critical free energy of nucleation[82]

$$N^* = -\frac{8}{27} \left( \frac{\sum_i \eta_i \Gamma_i}{\mu_2 - \mu_1} \right)^3$$

Equation 2:2 – Expression for the critical cluster size[82]

where  $\mu_1$  and  $\mu_2$  are the chemical potentials of the bulk amorphous and crystalline phases,  $\Gamma_i$  is the interfacial free energy per unit interfacial area for the  $i^{\text{th}}$  area and  $\eta_i$  is the shape factor for the  $i^{\text{th}}$  area, a term dependent on the shape the cluster adopts to minimize its energy.

Reports[31, 73] have shown that a  $\text{PbI}_2$  film is of the 2H polytype and displays a preferential orientation such that the (001) face of the crystalline clusters is in contact with the MAI solution, as shown in Figure 2:7b and Figure 2:7c. We suggest that the amorphous component, apart from crystallizing in situ, is transported, possibly through the MAI solution or along the surface of the film, to add to crystalline clusters resulting in their growth (Figure 2:7c). For the (001) face, the interfacial free energy is a function of the crystal-MAI solution interfacial tension ( $\gamma$ )[83] and influenced by the MAI solution in contact with the face. From Lippmann's equation, we derive the expression for the surface tension as:

$$\gamma = \gamma_0 - \frac{\sigma^2}{2c_0}$$

Equation 2:3 – Equation for surface tension[79, 83]

where  $\gamma_0$  is the surface tension at zero charge,  $\sigma$  is the excess surface charge and  $c_0$  is the double-layer capacitance.

Figure 2:7d shows the relationship between the free energy change and cluster size, depicting the critical free energy of nucleation and critical cluster size in the dark and under illumination. The sum of the interfacial and the volume free energy terms gives the total free energy change in each case. In the dark, there exists a particular value of the critical free energy, denoted  $\Delta G^*_{\text{dark}}$  and the corresponding critical cluster size, denoted  $N^*_{\text{dark}}$ . The metastable  $\text{PbI}_2$  film (standard, as-deposited) is

reported to have a distribution of crystalline clusters of different sizes[84] schematically represented in Figure 2:7e and Figure 2:7f. These are the potential nuclei for secondary nucleation, of which only clusters larger than the critical cluster size, in this case  $N^*_{dark}$  (Figure 2:7e), nucleate, i.e. start growing to form larger crystals.

So far, we have discussed how clusters larger than the critical cluster size survive and grow, consuming the amorphous material in the film. In addition, Ostwald ripening is likely to take place at later stages of the growth process. Here, clusters that were smaller than the critical cluster size and could not grow, are consumed to enable the further growth of those that surpassed the critical cluster size

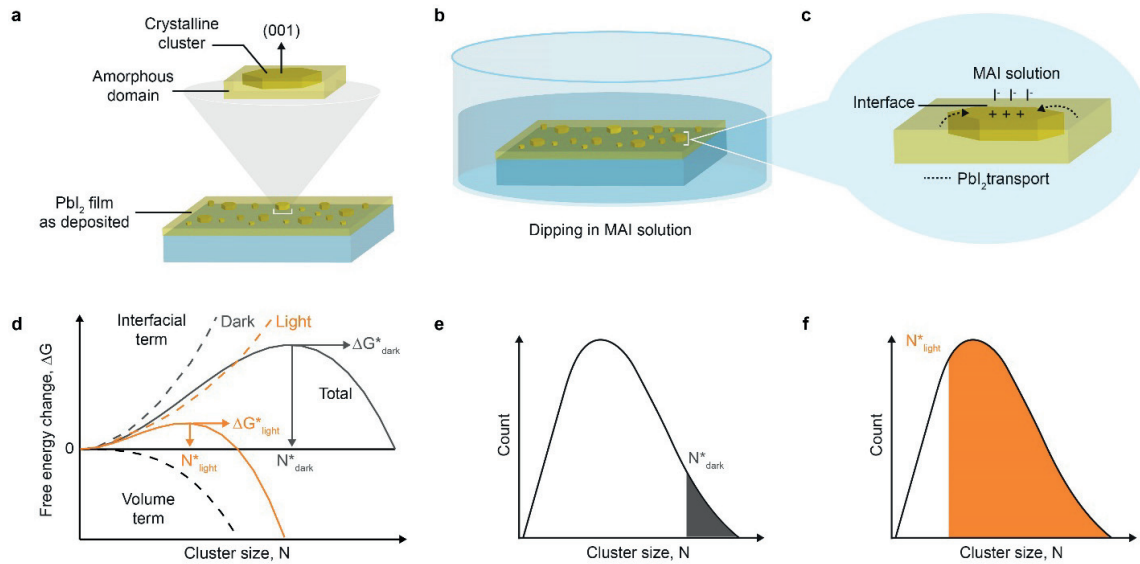


Figure 2:7 Diagrams of the nucleation mechanism in the  $PbI_2$  film. a,  $PbI_2$  film as-deposited, showing amorphous domains and crystalline clusters. A crystalline cluster embedded in the amorphous component is shown with the (001) face exposed. b, Dipping the  $PbI_2$  film in the MAI solution. c, Accumulation of  $I^-$  ions at the interface in the MAI solution due to photo-generated holes trapped at the  $PbI_2$  surface.  $PbI_2$  transport from amorphous domains to a crystalline cluster is shown. d, Dependence of free-energy change on cluster size: contributions from interfacial and volume terms are shown, with the critical free energy of nucleation ( $\Delta G^*$ ) and the critical cluster size ( $N^*$ ) in the dark and under illumination. e, Cluster size distribution in an as-deposited  $PbI_2$  film. The fraction of the clusters acting as nuclei and growing in the dark is shown in grey. f, The fraction of the clusters growing under illumination is shown in orange.

Under illumination, we posit that  $\Delta G^*$  and  $N^*$  are lower and this facilitates more nucleation. We propose that the surface traps in the  $PbI_2$  film are populated with photo-generated carriers, most likely holes (as discussed later) and thereby increase the surface charge. As a response, to compensate for the positive charge on the  $PbI_2$  surface,  $I^-$  ions in the MAI solution would migrate to the interface to form the outer Helmholtz plane (Figure 2:7c). According to Equation 2:3[79, 83], an increase in charge density at the interface decreases the surface tension below the value observed in the dark. This lowers the critical free energy of nucleation and the critical nucleus size such that  $\Delta G^*_{light} < \Delta G^*_{dark}$  and

$N_{light}^* < N_{dark}^*$  (Equation 2:1[82] and Equation 2:2[82]), and smaller crystalline clusters in the  $\text{PbI}_2$  film surpass  $N_{light}^*$  and grow (Figure 2:7f).

The higher the light intensity, the higher the number of charge carriers trapped at the surface and the lower the surface tension. Based on the above discussion, this gives a higher nucleation density under high light intensities, as observed in Figure 2:3b, where the nucleation density scales logarithmically with light intensity. This dependence might be rationalized by the fact that the trapped capacitive charge increases linearly with photo-voltage, which scales logarithmically with light intensity[86] (Figure 2:5g).

### Photo-electrochemical experiments identifying the carrier trapped in the $\text{PbI}_2$ surface traps

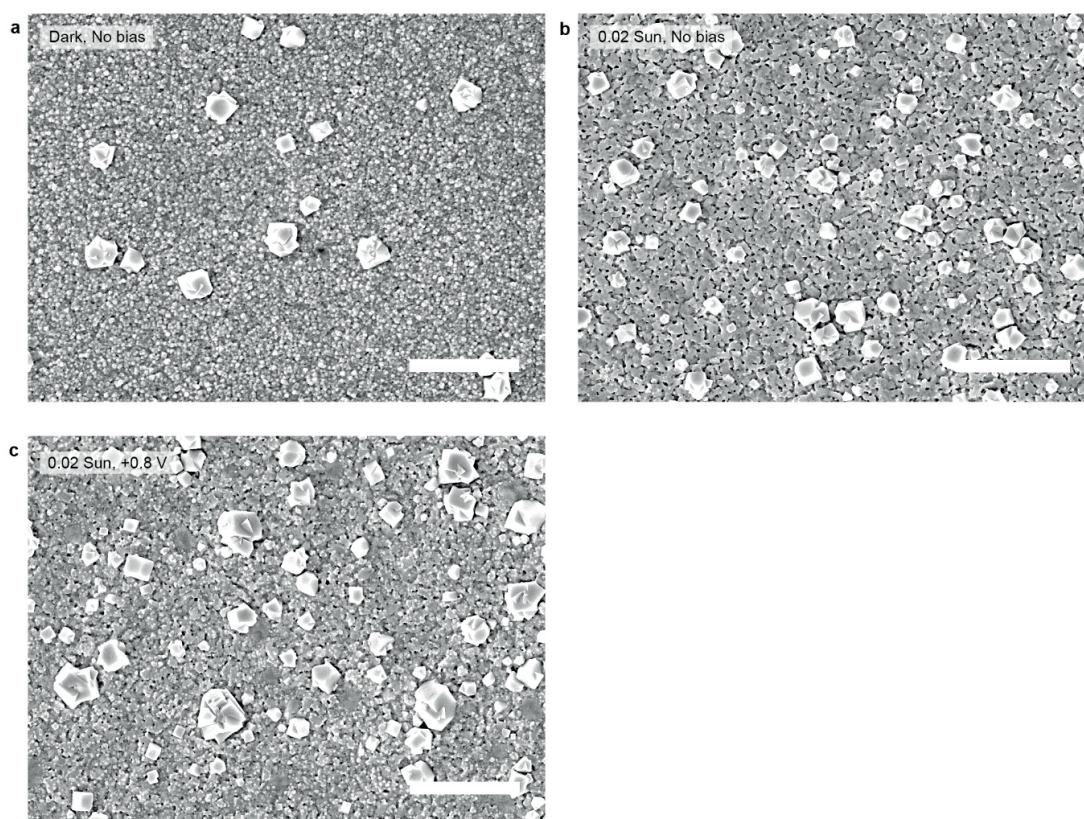


Figure 2:8 Effect of populating surface traps. Shown are SEM images of  $\text{PbI}_2$  films that have been dipped for 6 s in 0.038 M MAI in 2-propanol solution; a, in the dark, no voltage bias; b, under 0.02 Sun illumination, no voltage bias; and c, under 0.02 Sun illumination, bias of + 0.8 V versus the Nernst potential of MAI. Panels (b) and (c) show comparable nucleation density, while that in (a) is low. Scale bars (a–c), 2  $\mu\text{m}$ .

To determine whether the surface traps in the  $\text{PbI}_2$  films are for electrons or holes, we conducted experiments applying an external voltage to a standard (as-deposited)  $\text{PbI}_2$  film during dipping in a MAI solution in the dark, but could not induce a high nucleation density. The external voltage we applied (-0.8 V to +0.8 V) manipulates the electron density on the surface of the film, but does not



generate holes in  $\text{PbI}_2$ . This points to the photo-generated holes being the carrier type instrumental in the nucleation. At a voltage of +0.8 V (reverse bias), the  $\text{PbI}_2$  delaminates. This indicates that more positive potentials are not accessible and inversion cannot be achieved, so it is not possible to have holes as majority carriers on the surface. Films dipped under illumination with an external voltage bias, draining the electrons from the film while the photo-generated holes remain trapped at the surface, show high nucleation density (Figure 2:8). Thus, we conclude that photo-generated holes are indeed involved in lowering the surface tension.

### **Crystallization of $\text{PbI}_2$ in an ionic liquid and alternative photo-redox mechanism**

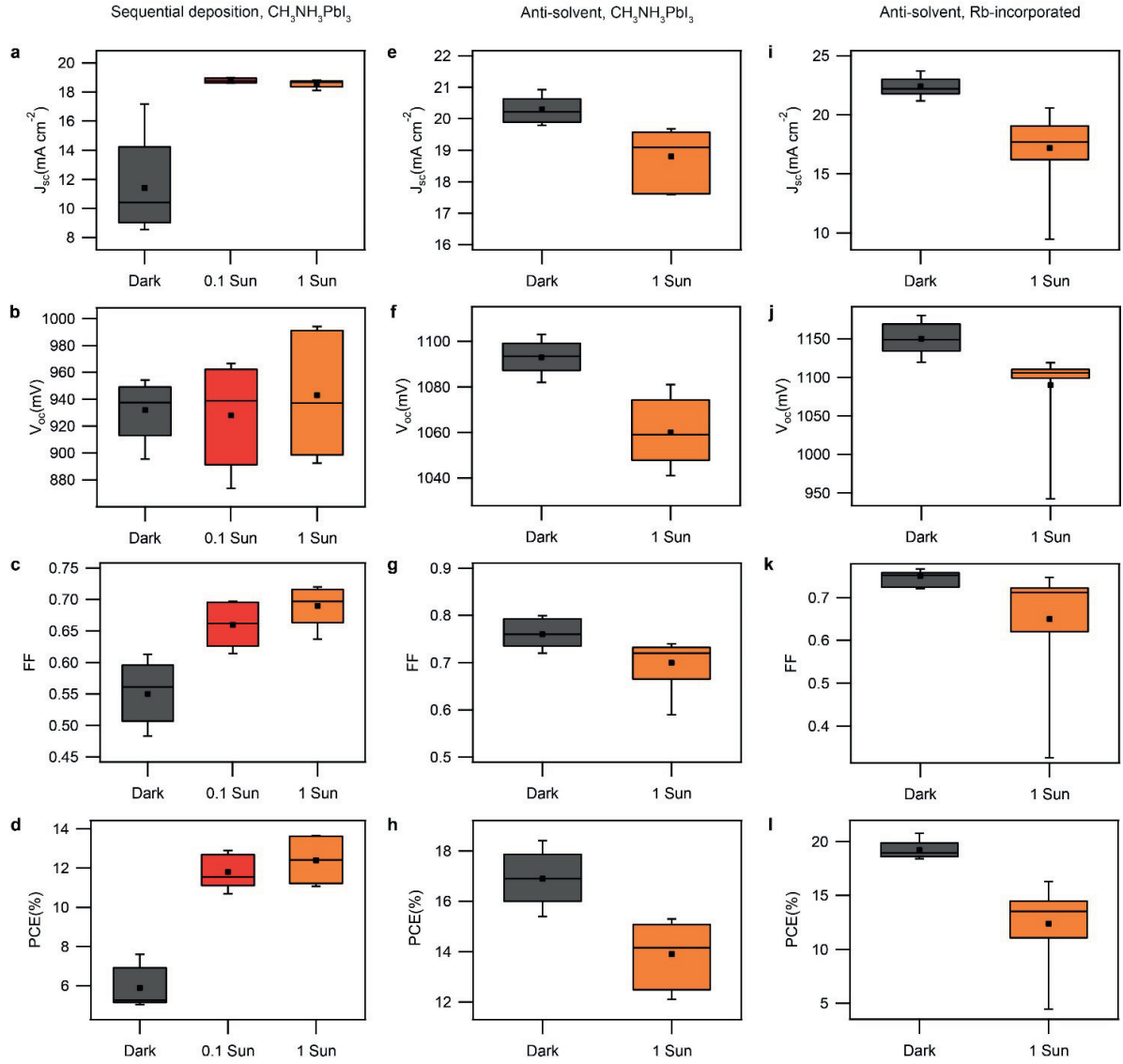
We also studied the crystallization of  $\text{PbI}_2$  in different environments. To begin with, pure 2-propanol does not induce nucleation. As already mentioned, we conducted experiments replacing the MAI solution with an ionic liquid solution as a chemically unreactive alternative that does not form perovskite. Through XRD analysis, we show that light-activated nucleation is facilitated by the ionic liquid solution (see Figure 2:2). At this point, we considered the possibility of an alternative mechanism taking place, namely photo-redox[87] - i.e. oxidation reactions involving the photo-generated holes. However, it is highly unlikely, as the logarithmic dependence of the nucleation density on light intensity, observed in Figure 2:3b, cannot be explained. Moreover, since the ionic liquid, whose ions cannot be oxidized or reduced by  $\text{PbI}_2$ , also enhances the crystallization of  $\text{PbI}_2$ , we rule it out.

## **2.2.4 Photovoltaic devices**

### **Sequential deposition**

In order to demonstrate the practical applicability of the light effect to tune the perovskite morphology, we fabricated photovoltaic devices in the dark, under 0.1 Sun and 1 Sun light intensities (details in section 2.4: Materials and methods). The average value of the PCE was found to increase from 5.9% when cells were made in the dark to 12.4% (with 13.7% obtained for the best-performing cell) when they were made under 1 Sun illumination. Statistical analysis of photovoltaic data is presented in Figure 2:9. Average values of the PCE data and hysteresis data is shown in Table 2:1. In the case of dipping under high light intensity, the presence of smaller crystals that give superior surface coverage and thereby more homogeneity is observed (Figure 2:10, XRD spectra also shown). This allows better absorption of incident light, improving the photocurrent density, as reflected in the IPCE (Figure 2:11).





**The effect of illumination on the formation of perovskite films**

a						
Deposition method, composition	Light intensity during preparation		$J_{sc}$ (mA cm <sup>-2</sup> )	$V_{oc}$ (mV)	Fill factor	PCE(%)
Sequential deposition, CH <sub>3</sub> NH <sub>3</sub> PbI <sub>3</sub>	Dark		11.4 ± 3.4	932 ± 22	0.55 ± 0.05	5.9 ± 1.1
	0.1 Sun		18.8 ± 0.2	929 ± 38	0.66 ± 0.04	11.8 ± 0.9
	1 Sun		18.6 ± 0.3	943 ± 46	0.69 ± 0.03	12.4 ± 1.2
Anti-solvent, CH <sub>3</sub> NH <sub>3</sub> PbI <sub>3</sub>	Dark		20.3 ± 0.4	1093 ± 8	0.76 ± 0.03	16.9 ± 1.1
	1 Sun		18.8 ± 0.9	1060 ± 15	0.70 ± 0.06	13.9 ± 1.3
Anti-solvent, Rb-incorporated	Dark		22.4 ± 0.8	1150 ± 19	0.75 ± 0.02	19.2 ± 0.7
	1 Sun		17.2 ± 3.1	1090 ± 52	0.65 ± 0.13	12.4 ± 3.8
b						
Deposition method, composition	Light intensity during preparation	Scan direction	$J_{sc}$ (mA cm <sup>-2</sup> )	$V_{oc}$ (mV)	Fill factor	PCE(%)
Sequential deposition, CH <sub>3</sub> NH <sub>3</sub> PbI <sub>3</sub>	Dark	Forward	8.5	922	0.60	4.8
		Backward	8.5	944	0.61	5.0
	0.1 Sun	Forward	19.0	954	0.67	12.4
		Backward	19.0	966	0.66	12.4
	1 Sun	Forward	18.8	974	0.71	13.2
		Backward	18.7	987	0.72	13.7
Anti-solvent, CH <sub>3</sub> NH <sub>3</sub> PbI <sub>3</sub>	Dark	Forward	21.2	1075	0.72	16.4
		Backward	20.9	1074	0.73	16.4
	1 Sun	Forward	17.6	987	0.65	11.4
		Backward	17.5	1019	0.71	12.6
Anti-solvent, Rb-incorporated	Dark	Forward	23.7	1141	0.76	20.6
		Backward	23.7	1159	0.75	20.7
	1 Sun	Forward	20.1	1112	0.67	14.9
		Backward	20.2	1109	0.67	15.0

Table 2:1 Photovoltaic device data recorded under simulated AM1.5G illumination. a, Average values of parameters shown with standard deviations from the backward scans of numerous devices (5 CH<sub>3</sub>NH<sub>3</sub>PbI<sub>3</sub> cells made using sequential deposition, 6 CH<sub>3</sub>NH<sub>3</sub>PbI<sub>3</sub> cells made using the anti-solvent method and 10 Rb-incorporated composition cells made using the anti-solvent method) prepared under different illumination conditions. b, Photovoltaic parameters from the forward and backward scans of one device of each preparation condition. The hysteresis of the photovoltaic devices is low.

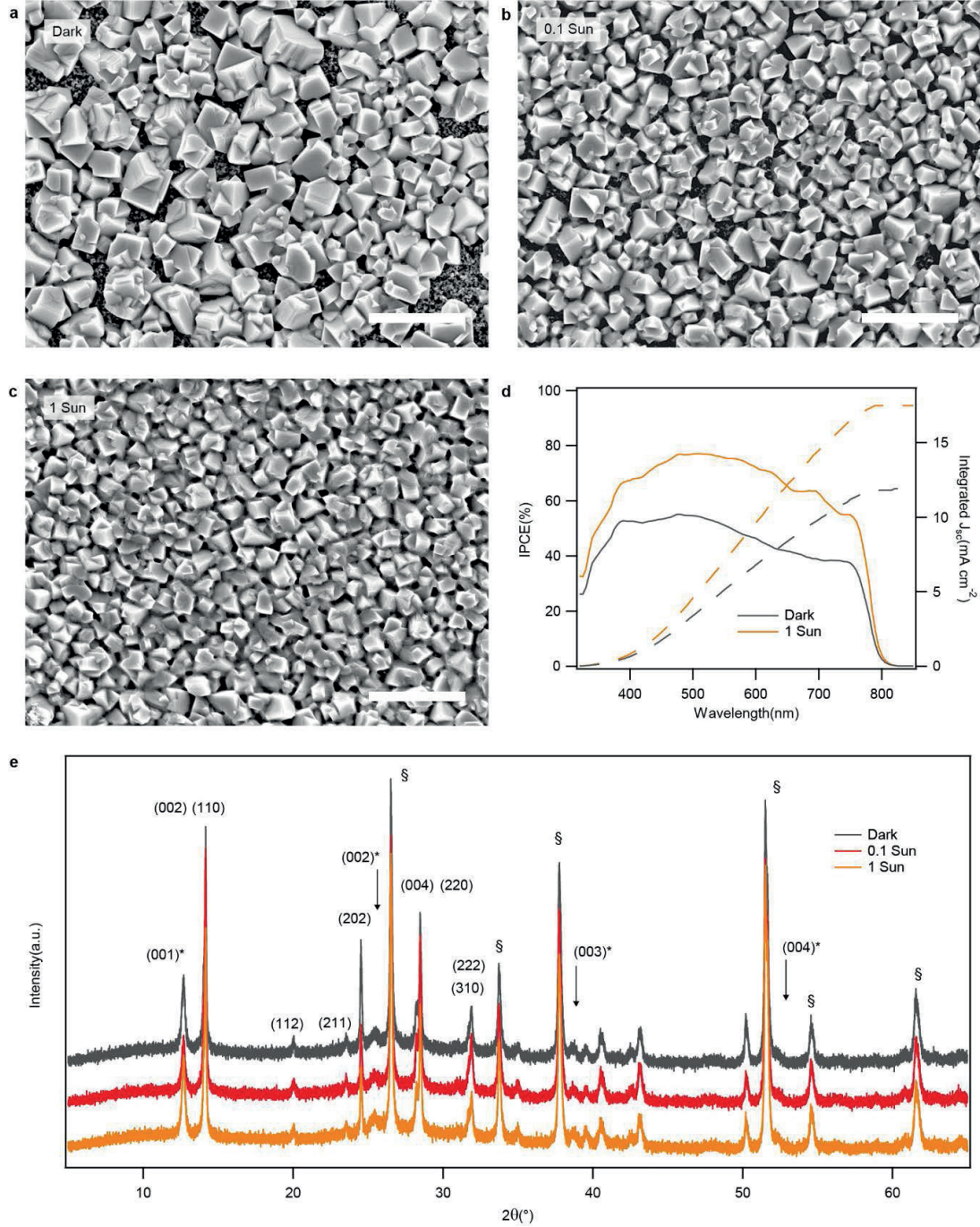


Figure 2:10 Photovoltaic device characterization and analysis of  $\text{CH}_3\text{NH}_3\text{PbI}_3$  samples made using sequential deposition. a-c, SEM images of the perovskite films corresponding to devices dipped into MAI solution in the dark, and under 0.1 Sun and 1 Sun respectively. Scale bars (a-c), 1  $\mu\text{m}$ . d, Absolute IPCE spectra (solid lines) and the integrated current densities (dashed lines) of representative devices dipped into MAI solution in the dark and under 1 Sun. e, XRD spectra of perovskite films dipped into MAI solution in the dark, and under 0.1 Sun and 1 Sun. The main reflections corresponding to the tetragonal perovskite have been indicated. \* Reflections of the  $\text{PbI}_2$  in the 2H polytype;  $\S$  reflections from the FTO. Similar amounts of  $\text{PbI}_2$  remain in all the films.

### Anti-solvent method

The light-effect is a phenomenon present in different film deposition methods, not merely limited to sequential deposition. We investigated the effect of illumination on the film formation in the anti-solvent method, the route employed in the fabrication of high efficiency solar cells[33, 35]. As mentioned earlier, in this method, a perovskite precursor solution was spin-coated, then an anti-solvent was dripped, following which the sample was heated.

$\text{CH}_3\text{NH}_3\text{PbI}_3$  solar cells made in the dark using the anti-solvent method have higher PCE (16.9%, obtaining 18.4% for the best-performing cell) compared to those prepared under 1 Sun illumination (13.9%). The statistical analysis is shown in Figure 2:9, while average values and hysteresis data are in Table 2:1. IPCE spectra are presented in Figure 2:11. In contrast to the sequential deposition method, surface coverage is not an issue for the anti-solvent method. SEM and CLSM images confirm that excellent surface coverage is obtained for  $\text{CH}_3\text{NH}_3\text{PbI}_3$  perovskite films made using the anti-solvent method, both in the dark (Figure 2:12a) and under 1 Sun illumination (Figure 2:12b). However, the large number of crystals obtained under illumination (Figure 2:12b) in the anti-solvent method introduce more grain boundaries in the film, which are detrimental to solar cell performance[88].

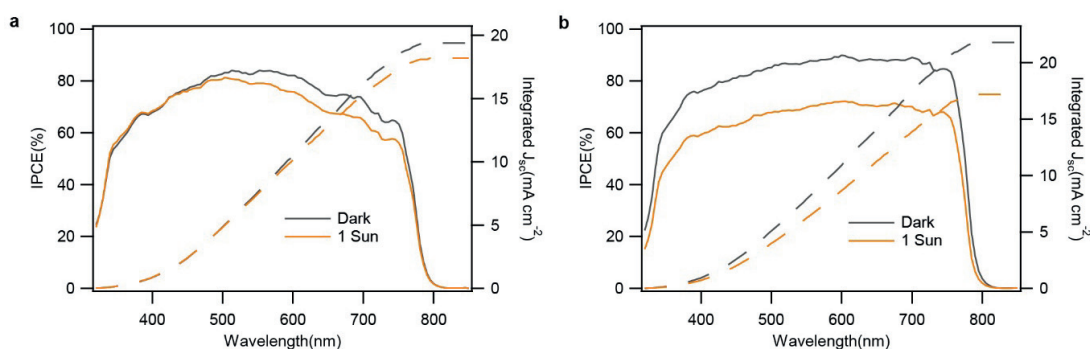


Figure 2:11 Absolute IPCE spectra (solid lines) and the integrated current densities (dashed lines) of representative devices prepared using the anti-solvent method in the dark and under 1 Sun illumination. a,  $\text{CH}_3\text{NH}_3\text{PbI}_3$ ; b, Rb-incorporated composition.

While the increased crystal density under illumination in the anti-solvent method (Figure 2:12) is similar to the observation made for sequential deposition (Figure 2:3), the mechanism of the perovskite formation through the anti-solvent method is more complex due to the various intermediates formed during processing[34]. Reports suggest that clusters of lead halides crystallize in the perovskite precursor solution and represent the first step towards perovskite formation[89]. We posit that the lead halide crystallization is influenced by illumination in a manner analogous to our findings for sequential deposition.



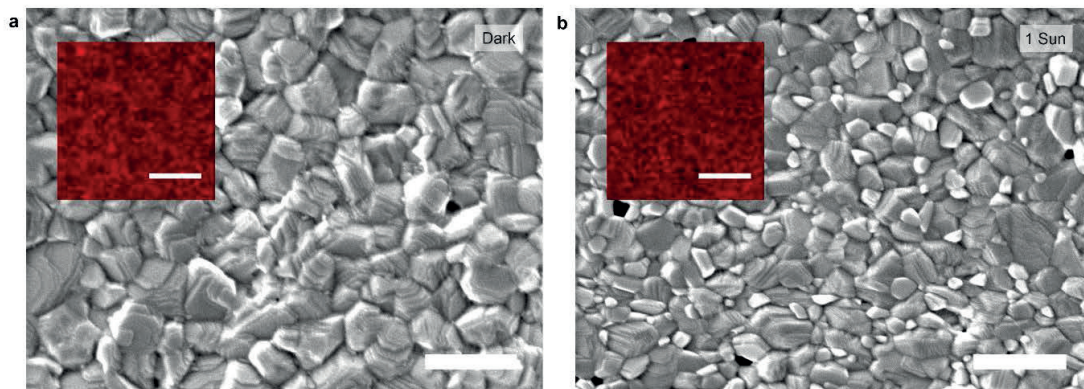


Figure 2:12 Images of  $\text{CH}_3\text{NH}_3\text{PbI}_3$  films made using the anti-solvent method in the dark and under a light intensity of 1 Sun. Main panels, SEM images. a, Film made in the dark showing low perovskite crystal density. b, Film made under 1 Sun illumination showing high perovskite crystal density. Insets show CLSM images with emission between 700 nm and 800 nm attributed to perovskite and assigned a red colour. Colour saturation scales with emission intensity. Scale bars: main panels (a, b), 0.5  $\mu\text{m}$ ; insets (a, b), 5  $\mu\text{m}$ .

The light-effect prevails robustly even in predominantly formamidinium-based[33, 35, 36] compositions of progressively-increasing complexity, such as the double-cation[33], triple-cation[36] and Rb-incorporated compositions[35] described in section 1.3.3. SEM images demonstrating the effect of light on these compositions are shown in Figure 2:13. For the Rb-incorporated composition[35], we observe the superior performance of cells made in the dark (average PCE of 19.2%, best-performing cell PCE of 20.7%) compared to those made under illumination of 1 Sun (average PCE of 12.4%). The statistical analysis is shown in Figure 2:9. The average values and hysteresis data are presented in Table 2:1, while the IPCE spectra are shown in Figure 2:11. We therefore identify that dark conditions are advantageous in the anti-solvent method in contrast to the sequential deposition method.



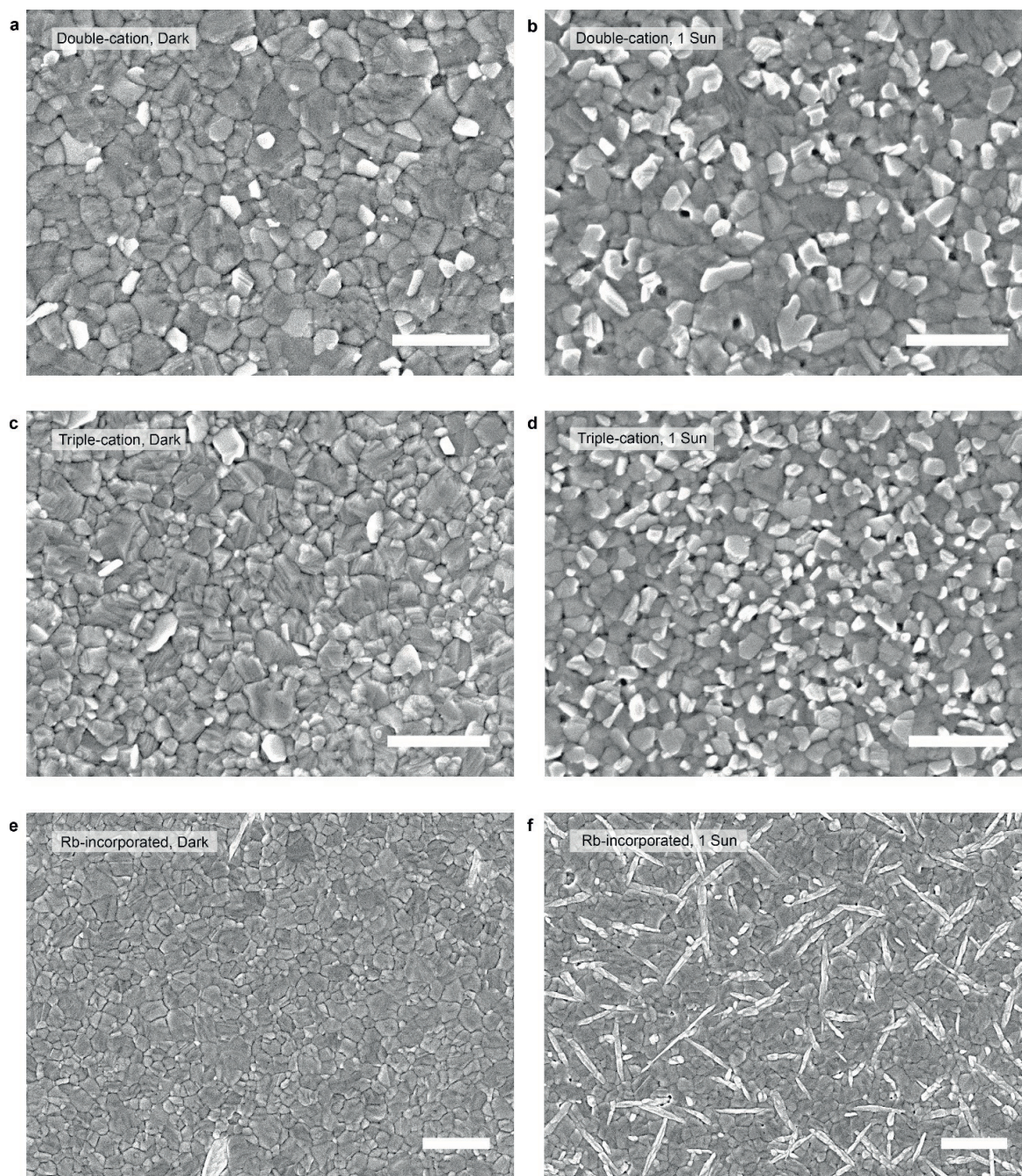


Figure 2:13 SEM images of perovskite films prepared using the anti-solvent method. a, b, Double-cation composition made in the dark (a) and under 1 Sun illumination (b). c, d, Triple-cation composition made in the dark (c) and under 1 Sun (d). Scale bars (a-d), 1  $\mu\text{m}$ . e, f, Rb-incorporated composition made in the dark (e) and under 1 Sun (f). Scale bars (e, f), 2  $\mu\text{m}$ .

### 2.2.5 CLSM study of formation of complex perovskites in anti-solvent method

So far, we looked into the final morphology of the double-cation, the triple-cation and the Rb-incorporated perovskite films when they are prepared with and without illumination through the anti-solvent method. When perovskites of these compositions are prepared using the anti-solvent method,

film formation requires different amounts of time based on the composition. Progressively smaller periods are needed after dripping the anti-solvent for the perovskite film to form for methylammonium lead iodide, the double-cation composition, the triple-cation composition and the Rb-incorporated perovskite respectively[36]. This indicates that there are likely to be differences in the process of formation of these perovskites. As these compositions were developed for achieving increasingly higher photovoltaic performance, it is interesting to investigate these differences in perovskite formation and identify the reason behind the superior film quality obtained while using compositions that are more complex.

Keeping this goal in mind, we look into these compositions, focusing on comparing the crystallization process in the anti-solvent method after the precursor solution has been spin-coated and anti-solvent has been dripped on the sample. Such samples that have not been exposed to any heat treatment are referred to as unannealed samples hereafter. These unannealed samples are examined using various characterization techniques such as optical measurements and CLSM imaging.

### Optical measurements

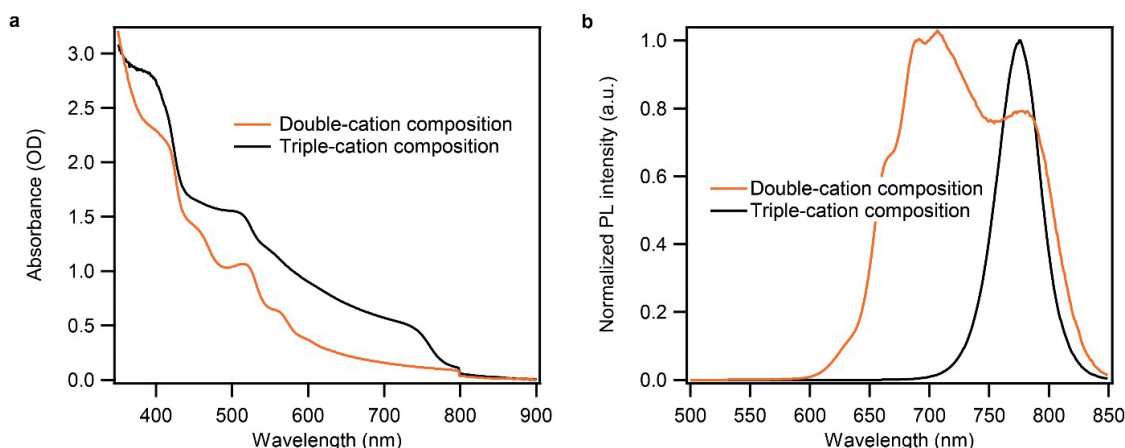


Figure 2:14 Optical measurements of unannealed perovskite films of the double-cation and the triple-cation compositions. a, Absorption spectra (OD, optical density). b, Steady-state photoluminescence (PL) measurements (a.u., arbitrary units).

To begin with, we perform optical measurements on unannealed films of the double-cation and triple-cation compositions. Absorption spectra shown in Figure 2:14a reveal that multiple peaks are present between 400 and 600 nm for the double-cation composition. On the other hand, for the triple-cation composition, we observe the onset of absorption close to 780 nm which is characteristic of the perovskite of this composition[36]. From the steady state PL measurements in Figure 2:14b, we observe that several emissive species (with maxima at 645, 685, 700 and 775 nm) are formed in the unannealed sample for the double-cation composition. On the contrary, we observe the formation of a single emissive species for a film of the triple-cation composition with the emission maxima at 770 nm,



attributable to the perovskite[36]. The optical measurements for the Rb-incorporated composition are nearly identical to those shown here for the triple-cation composition. The measurements for the Rb-incorporated composition have been reported in detail in our work[35].

### **Confocal laser scanning fluorescence microscopy**

In order to investigate the various species observed above in further detail, we use CLSM to map the surfaces of unannealed films of the double-cation, triple-cation and Rb-incorporated compositions. These CLSM images are shown in Figure 2:15. The first row in Figure 2:15 shows CLSM images capturing the emission between 640 and 650 nm, assigned green colour. The second row shows the emission between 680 and 690 nm, assigned the colour blue, while the third row shows the emission between 725 and 735 nm, assigned red colour. These ranges were chosen based on the observations made in the steady state PL measurements. We attempted to study as many of the emissive species present in the double-cation composition as possible. The last row consists of composite images showing the emission from all three ranges.

In Figure 2:15 a-c showing the double-cation composition, we observe that emission is detected in all three images corresponding to three different wavelength ranges. This observation is consistent with the presence of many emission peaks originating from different chemical species as in the optical measurements discussed above. The composite image in Figure 2:15d shows these different chemical species in the double-cation composition and they are localized as discrete regions. This indicates that unannealed double-cation film begins perovskite formation with inhomogeneous starting conditions, which need to form the perovskite during the annealing step that follows.

On the other hand, the analogous images for the triple-cation composition (Figure 2:15e, Figure 2:15f) and the Rb-incorporated composition (Figure 2:15i, Figure 2:15j) show that there is no emission in the 640-650 nm range and the 680-690 nm range. However, the films are emissive between 725 and 735 nm (Figure 2:15g shows the triple-cation composition, Figure 2:15k shows the double-cation composition) and this emission is attributable to the perovskite[36]. Therefore, we observe that triple-cation and Rb-incorporated composition films are emissive in a narrow range and begin to form the final perovskite film from a homogeneous film obtained after treatment with anti-solvent. In other words, for these compositions we see the rapid formation of a photoactive perovskite phase instead of a mixture of different species that need to finally form the perovskite as in the case of the double-cation composition. Such circumstances involving homogenous starting conditions and the apparently rapid formation of the perovskite phase are likely to result in the formation of homogenous perovskite films of high quality upon annealing for the triple-cation and Rb-incorporated compositions. This is posited to be one of the advantages leading to superior photovoltaic performance of solar cells with



these complex formulations. This improvement in solar cell performance was presented in our report[35].

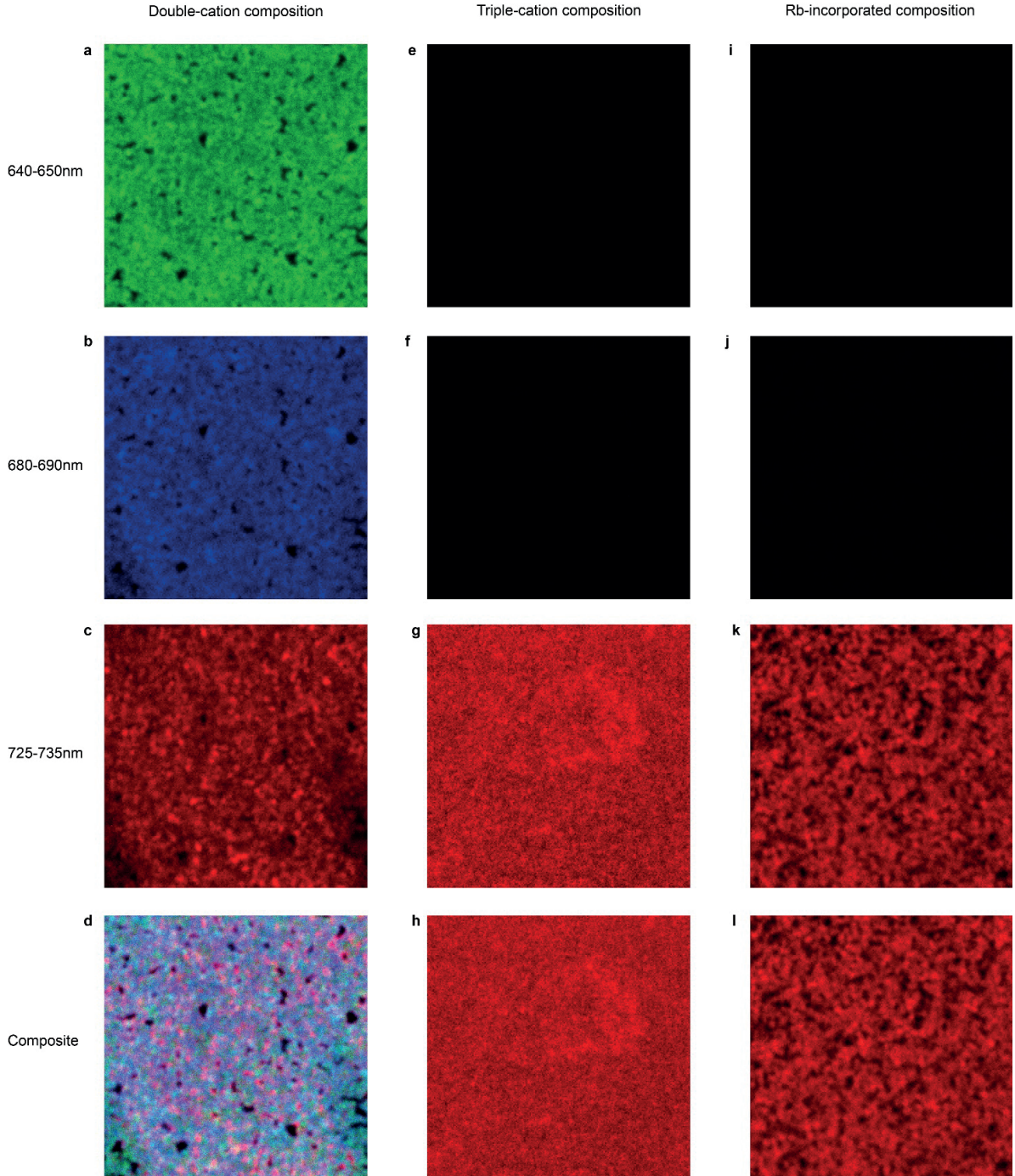


Figure 2:15 Unannealed perovskite films of a–d, the double-cation, e–h, the triple-cation and i–l, the Rb-incorporated compositions. In these CLSM images, the emission between 640 and 650 nm is assigned a green colour (images a, e, i), while the emission between 680 and 690 nm is assigned a blue colour (images b, f, j) and the emission between 725 and 735 nm is assigned a red colour (images c, g, k). Composite images showing all three emissions for each sample are shown in images (d), (h) and (l). Colour saturation scales with emission intensity. Images are 26.36x26.36  $\mu\text{m}^2$  each.

## 2.3 Conclusion

Recent progress in perovskite solar cell performance has been mainly due to engineering of deposition methods, with limited effort directed at understanding reaction mechanisms. In the sequential deposition method, we show that the  $\text{PbI}_2$  film crystallizes prior to the intercalation of MAI to form perovskite. Light absorbed by  $\text{PbI}_2$  induces a higher nucleation density. We propose that surface traps capture photo-generated holes, thus decreasing the surface tension. This decrease lowers the height of the nucleation barrier and the critical cluster size, enabling a larger fraction of the potential nuclei in the  $\text{PbI}_2$  film to grow. It enhances surface coverage and in turn device efficiency, attesting that light is an effective tool for tailoring perovskite morphology in sequential deposition.

In the anti-solvent method, we obtain a higher number of crystals under illumination and demonstrate that the photo-effect is robust as it is unmitigated by changing variables, such as composition, in processing. Dark conditions are identified as optimal for the anti-solvent method, as fewer but larger crystals are beneficial for photovoltaic performance. Our results establish illumination as a major factor in various deposition methods, which should always be considered while preparing perovskite films for opto-electronic applications.

Finally, we use CLSM to study and compare the formation of perovskites of increasingly complex compositions made using the anti-solvent method. In the unannealed double-cation film, perovskite formation proceeds from inhomogeneous starting conditions due to the presence of various emissive species that form early on after the anti-solvent is dripped. On the contrary, for the triple-cation and Rb-incorporated compositions, the rapid formation of the perovskite phase directly and the homogeneity of the film after treatment with anti-solvent possibly result in the formation of high quality films. This is likely to be one of the reasons for the superior photovoltaic performance of solar cells made using these complex perovskite compositions.

## 2.4 Materials and methods

### 2.4.1 Materials

Materials used in the study were purchased from Sigma-Aldrich, Acros Organics or TCI Chemicals while spiro-MeOTAD, employed as the hole conductor in our devices, was sourced from Merck KGaA. MAI was prepared in-house as described in the report by Im et al.[23] or obtained from Dyesol. The  $\text{Al}_2\text{O}_3$  paste of 23 nm diameter particles was prepared in-house. Commercial  $\text{TiO}_2$  pastes (18 NR-T and 30 NR-D) were obtained from Dyesol. Films used to study the effect of photon energy and the role of the illumination spectrum employed FTO-coated glass substrates (Tec15, Pilkington) while the remaining samples were made using Nippon sheet glass.

#### 2.4.2 Sequential deposition sample preparation

Standard samples included a mesoporous  $\text{Al}_2\text{O}_3$  layer (300 nm thick), processed as mentioned in the report by Burschka et al.[31] A 1.3 M  $\text{PbI}_2$  (Sigma-Aldrich) in N, N-dimethylformamide (Acros) solution at 70 °C, was spin-coated at 6500 rpm for 20 s and the films dried at 70 °C for 10 min. A low concentration of MAI (prepared in-house) solution in 2-propanol ( $6 \text{ mg ml}^{-1}$  or 0.038 M) was used in all experiments except the device preparation. This was in order to keep the reaction rate sufficiently low so that kinetic features could be monitored and analysed effectively. Samples of specific reaction times were prepared by dipping  $\text{PbI}_2$  films in MAI solution at 25 °C for the required period, followed by washing in 2-propanol to halt the reaction. A calibrated white LED array (LXM3-PW51 4000K, Philips), where integration over wavelength gave the required light intensity (for instance  $100 \text{ mW cm}^{-2}$ , which we mention as 1 Sun), was used for illumination during dipping. The light was incident normal to the sample surface while submerged in MAI solution. The films were dried at 70 °C for 10 min.

#### 2.4.3 Confocal laser scanning fluorescence microscopy and image processing

Images were obtained using Leica Application Suite X software on a confocal laser scanning microscope (Leica TCS SP8), using a HC PL APO oil objective (63x/1.40). A 440 nm pulsed diode laser was used for excitation with the excitation power and the gain chosen to optimize the dynamic range of the detector (PMT, HyD or HyD SMD).

Single plane 512x512 images were acquired at 25°C from a unidirectional scan of 400 Hz speed with a pinhole size of 1 Airy unit. They were acquired at a resolution of 72 nm in xy with an image bit depth of 8. Fiji was used for image processing: Different emissions mapped to different channels were pseudo-coloured, with linear brightness and contrast adjustments done equally across all images for each channel. Images were set to a size of  $8 \times 8 \text{ cm}^2$  at 600 dpi using bicubic interpolation and cropped to  $8 \times 4 \text{ cm}^2$  for display (Figure 2:1).

#### 2.4.4 Ultraviolet–visible spectroscopy and experiments

Samples used to study the effect of photon energy were prepared in a Horiba Jobin Yvon Fluorolog spectrofluorometer. Each film was exposed to a 0.038 M MAI solution for 25 s, under illumination of the required energy and comparable photon flux. The photon flux was adjusted using OD filters. The absorbance data was collected in transmission mode using a Varian Cary 5 spectrophotometer.

#### 2.4.5 Electrochemical experiments

350 nm thick  $\text{PbI}_2$  films were deposited on Nippon sheet glass using the standard parameters. While the films used in the experiments shown in Figure 2:8 were dried under standard conditions, the films

used for steady state experiments were annealed at 100 °C for 1 h to crystallize them and improve stability. The films were contacted and encapsulated using epoxy or hot glue. A photograph of the sample is shown in Figure 2:5a and a cross sectional schematic in Figure 2:5b.

Chronopotentiometry measurement under chopped light and EIS measurements were carried out in a 3-electrode configuration using an Ag/AgCl, KCl (sat'd) reference electrode, a Pt wire as the counter electrode and the PbI<sub>2</sub> film as the working electrode in a 0.38 M 1-Ethyl-3-methylimidazolium bis(trifluoromethylsulfonyl)imide (EMIm TFSI) in 2-propanol solution (Figure 2:5c and Figure 2:5d). To determine the chemical potential of the MAI solution, two half cells connected by a salt bridge were employed, one containing a Pt wire (working electrode) in the 0.038 M MAI solution and the other a Pt wire (counter electrode) and the reference electrode in 0.38M EMIm TFSI in 2-propanol (Figure 2:5e). In the experiment to study the effect of populating traps, we used standard PbI<sub>2</sub> films as the working electrode and a Pt wire as a counter electrode. The films were dipped for 6 s in 0.038 M MAI solution under bias.

The calibrated white LED array (LXM3-PW51 4000K, Philips) mentioned earlier was used for illumination, with the light incident normal to the film surface. A SP-200 potentiostat (BioLogic Science Instruments) equipped with a frequency analyser was used for the electrochemical measurements. Full impedance spectra were measured at frequencies from 100 kHz to 10 Hz with a sinusoidal potential perturbation of 10 mV. The range of the bias potential was -0.5 to +0.9 V vs. Ag/AgCl, KCl (sat'd). The EIS data was modelled using a simple RC circuit in series with a resistance (series resistance) using Zview (Scribner Associates). The extracted capacitance was plotted in a Mott-Schottky plot according to the equation[90]:

$$\left(\frac{A_S}{C_{SC}}\right)^2 = \frac{2}{e\epsilon_r\epsilon_0 N_D} \left(V - V_{fb} - \frac{k_B T}{e}\right)$$

Equation 2:4 – Expression used for Mott-Schottky analysis[81]

where  $(C_{SC}/A_S)$  is the surface-area-corrected space-charge layer capacitance,  $e$  is the elementary charge,  $\epsilon_r$  is the dielectric constant of PbI<sub>2</sub>,  $\epsilon_0$  is the vacuum permittivity,  $N_D$  is the charge carrier density (in cm<sup>-3</sup>),  $V$  is the applied potential,  $V_{fb}$  is the flat band potential,  $k_B$  is the Boltzmann constant and  $T$  is the temperature (in K).

#### 2.4.6 X-ray diffraction measurements

XRD measurements were carried out on an X'Pert MPD PRO (PANalytical) operated in Bragg-Brentano geometry. It consisted of a ceramic tube (Cu anode,  $\lambda=1.54060$  Å), a secondary graphite (002) monochromator and a real-time multiple strip X'Celerator detector. The automatic divergence slit and

beam mask were adjusted to the dimensions of the films. A step size of  $0.008^\circ$  and an acquisition time of  $1.5 \text{ min deg}^{-1}$  were chosen for data collection.

#### 2.4.7 Sequential deposition device preparation

Devices were prepared following the procedure outlined in Burschka et al.[31] A mesoporous  $\text{TiO}_2$  layer (18 NR-T, Dyesol) was deposited, a  $1.3 \text{ M PbI}_2$  (Sigma-Aldrich) solution in N, N-dimethylformamide (Acros) was spin-coated and  $8 \text{ mg ml}^{-1}$  MAI (prepared in-house) in 2-propanol solution were used for dipping. Dipping under various light intensities was implemented using the calibrated white LED array (LXM3-PW51 4000K, Philips), where the light was incident normal to the sample surface, while it was submerged in a MAI solution for 20 s. Isothermal conditions at  $25^\circ\text{C}$  were maintained for dipping using a climatic chamber (ST16, Angelantoni) and controlled relative humidity of 5% achieved by flushing the chamber with dry air. The perovskite films were rinsed using 2-propanol and dried at  $70^\circ\text{C}$  for 10 min. A Spiro-MeOTAD solution was spin-coated<sup>6</sup> on top and 80-100 nm thick gold electrodes were deposited through thermal evaporation under high vacuum. The solar cells had an active area of  $0.56 \text{ cm}^2$ .

#### 2.4.8 Sequential deposition device characterization

The current voltage characteristics were obtained by recording the generated photocurrent with a digital source meter (Model 2400, Keithley) under an externally-applied potential bias such that the scan speed was  $10 \text{ mV s}^{-1}$ . No device preconditioning, such as light soaking or voltage biasing in the dark, was applied before measurement. The light source was a 450-W xenon lamp (Oriel) fitted with a Schott K113 Tempax sunlight filter (Praezisions Glas & Optik GmbH) to match the emission spectrum of the lamp to the AM1.5G standard. Prior to each measurement, the light intensity was determined using a calibrated Si reference diode equipped with an infrared cut-off filter (KG3, Schott). Based on the intensity of the lamp, which varied between  $(91 \text{ and } 101 \text{ mW cm}^{-2})$ , the reported  $J_{sc}$  was linearly scaled to that for  $100 \text{ mW cm}^{-2}$ . IPCE spectra were recorded using the Ariadne system (Cicci Research). A non-reflective metallic mask with an aperture of  $0.16 \text{ cm}^2$  was used during both measurements.

#### 2.4.9 Anti-solvent method sample and device preparation

Li-doped  $\text{TiO}_2$  mesoporous films[35] were used to prepare devices in a nitrogen glove box maintained at  $25^\circ\text{C}$ , using the anti-solvent method. A  $\text{TiO}_2$  paste of 30 nm diameter particles was used to prepare the mesoporous layer (30 NR-D, Dyesol).  $\text{CH}_3\text{NH}_3\text{PbI}_3$  perovskite films were deposited from a precursor solution containing MAI ( $1.2 \text{ M}$ , Dyesol) and  $\text{PbI}_2$  ( $1.2 \text{ M}$ , TCI Chemicals) in anhydrous dimethylsulfoxide (Acros). The precursor solution was spin-coated using two steps, spinning at 1000 rpm for 10 s, and then at 4000 rpm for 30 s. 15 s prior to the end of the program, 200  $\mu\text{L}$  of

chlorobenzene was dripped on to the spinning substrate. After spin-coating, the films were kept either under 1 Sun illumination or in the dark for 15 min at room temperature, before heating at 100 °C for 40 min. As timeframes for perovskite formation depend on the composition used, the illumination time was chosen such that light was present until perovskite formation was complete[36].

The Rb-incorporated perovskite precursor solution was prepared as reported in the literature[35]. A two-step spin-coating procedure was used which involved spinning at 1000 rpm for 10 s, and then at 4000 rpm for 30 s. 200 µL of chlorobenzene was dripped on to the spinning substrate 20 s prior to the end of the program. The spin-coating was done either in the dark or under 1 Sun illumination. For the latter, illumination was continued for 1 minute after the sample was transferred onto the hot plate for heating at 100 °C for 40 min. The previously mentioned calibrated white LED array (LXM3-PW51 4000K, Philips) was used for illumination. The solar cells had an active area of 0.25 cm<sup>2</sup>.

#### 2.4.10 Anti-solvent method device characterization

The current voltage characteristics were obtained as mentioned above for the devices made using sequential deposition. However, for CH<sub>3</sub>NH<sub>3</sub>PbI<sub>3</sub> cells made using the anti-solvent method, a non-reflective metallic mask with an aperture of 0.1225 cm<sup>2</sup> was used for masking. A similar non-reflective metallic mask with an aperture of 0.16 cm<sup>2</sup> was used for all remaining measurements including IPCE spectra. IPCE spectra were recorded using the Ariadne system (Cicci Research).



# Chapter 3 The detailed path of sequential deposition for perovskite formation

*This chapter was adapted from the following article with the permission of the co-author and the journal.*

**Postprint version of the article:** [A. Ummadisingu](#) and M. Grätzel, "Revealing the detailed path of sequential deposition for metal halide perovskite formation," *Science Advances*, In press.

**My contribution:** Conceptualized the study, conducted the experiments excluding CL imaging, analyzed the data and prepared the manuscript.

Sequential deposition has been extensively employed for the fabrication of perovskite solar cells. However, fundamental aspects of the kinetics of methylammonium lead iodide perovskite formation still remain obscure. This chapter focuses on understanding methylammonium lead iodide perovskite formation in sequential deposition, which goes hand in hand with the results described in the previous chapter. It builds on some preliminary observations made in the study of the light effect that were not fully explored at that point.

To begin with, we scrutinize the individual stages of the reaction and investigate the crystallization of the lead iodide film which occurs before the intercalation of methylammonium iodide commences. Our study identifies the presence of mixed crystalline aggregates composed of perovskite and lead iodide during intercalation and structural reorganization. Moreover, Ostwald ripening occurs in the film for reaction times beyond the point of conversion to perovskite. Using cross-sectional confocal laser scanning fluorescence microscopy for the first time, we reveal that lead iodide in the over-layer and at the bottom of the mesoporous layer converts first. We identify unreacted lead iodide, trapped in the mesoporous layer for samples of complete conversion. We acquire kinetic data by varying different parameters and find that the Avrami models best represent them. The model facilitates the rapid estimation of the reaction time for complete conversion for a variety of reaction conditions, thereby ascertaining a major factor previously determined by extensive experimentation. This comprehensive picture of the sequential deposition is essential for control over the perovskite film quality, which determines the solar cell efficiency. Our results provide key insights to realize high quality perovskite films for opto-electronic applications.

## 3.1 Introduction

In the search for superior materials for use as light harvesters in mesoscopic heterojunction solar cells, organic-inorganic lead halide perovskites have emerged as strong contenders[18, 31]. Numerous researchers have been investigating solar cells based on methylammonium lead iodide ( $\text{CH}_3\text{NH}_3\text{PbI}_3$ ),

which possesses remarkable optical and electronic properties[18]. The various methods for the preparation of the perovskite films have been mentioned earlier. Here, we take a closer look at sequential deposition, one of the main methods used for depositing perovskite films for various applications.

Research on this method has been focused on improving photovoltaic performance by controlling the perovskite morphology through optimization of the processing conditions[91, 92] or via the use of additives[93, 94]. Some work focused on particular stages of the perovskite formation. For instance, Wu et al.[84] and Tu et al.[95] have looked into controlling the morphology and crystallinity of the  $\text{PbI}_2$  film to achieve better solar cell efficiency. Others have controlled the concentration of reactants:  $\text{PbI}_2$ [69] and MAI[68] to optimize the perovskite cell performance. Despite the efforts invested in this method, given the complexity of the reaction, it is difficult to control selected aspects of the deposition process and achieve reproducible results, while details of the remaining stages of the reaction are poorly understood. Thus, it is critical to scrutinize the various stages of perovskite formation and obtain a comprehensive picture of the path of sequential deposition.

In particular, fundamental aspects of the kinetics of  $\text{CH}_3\text{NH}_3\text{PbI}_3$  formation, such as the evolution of the film with the reaction coordinate (in other words with time), remain obscure. Characterization tools and techniques with the capacity to identify different chemical components need to be employed to study the surface of the film during perovskite formation. In addition, there is little insight available into the directionality of the reaction in the cross section of the film during or after the dipping. Furthermore, the role of unreacted  $\text{PbI}_2$  in the film has been well studied as it affects solar cell performance[77, 96]. However, the residual  $\text{PbI}_2$ , likely to be trapped at some regions in the film, has not been imaged so far.

Knowledge about these aspects of perovskite film formation would allow better control over perovskite film quality, thereby enhancing the solar cell performance[49]. A convenient way to determine the optimal reaction parameters, that are currently determined through rigorous experimentation, would aid in achieving reproducible film quality. Thus, systematic kinetic studies and a robust model that represents the kinetic data for a variety of reaction conditions are necessary.

In this chapter, we studied the individual stages of the reaction using various spectroscopic and analytical techniques such as XRD, SEM, CL and CLSM. We demonstrate that the stages of the reaction are the unexpected crystallization of partially amorphous  $\text{PbI}_2$  followed by MAI intercalation and structural reorganization, ending with Ostwald ripening. We demonstrate the use of SEM-CL to study perovskite films, specifically looking at mixed  $\text{PbI}_2$ -perovskite crystals. We show the innovative application of CLSM to look at cross sections of perovskite films at different stages of the reaction and obtain new insights into the various layers that compose the film. Lastly, we examine kinetic data



obtained under different reaction conditions and identify that Avrami models best represent the reaction kinetics. This model allows predicting the dipping time for a particular degree of conversion, including the point of complete conversion, as required for solar cell fabrication.

## 3.2 Results and discussion

### 3.2.1 Stages of the reaction

#### Crystallization of $\text{PbI}_2$

To begin with, we use XRD to examine  $\text{PbI}_2$  films dipped in  $6 \text{ mg ml}^{-1}$  MAI solution for different times between 2 s and 400 s.  $\text{PbI}_2$  films were prepared by spin coating from a 1.3 M solution in N, N-dimethylformamide at  $70^\circ\text{C}$ , onto a FTO-coated glass substrate covered with a mesoporous  $\text{Al}_2\text{O}_3$  layer, followed by heating at the same temperature for 10 min. XRD spectra of these films are presented in Figure 3:1a. We find that the unreacted  $\text{PbI}_2$  film is of the 2H polytype and the (001) reflection at  $12.66^\circ$  is the most prominent[31, 97]. The perovskite is detected at  $14.01^\circ$  and  $14.07^\circ$ , corresponding to the (002) and the (110) reflections of the tetragonal phase of the perovskite respectively[98, 99].

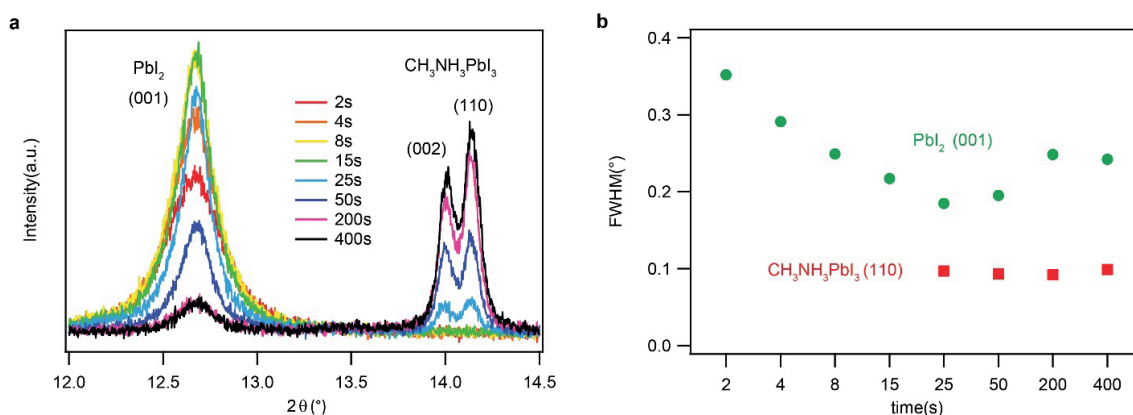


Figure 3:1 XRD analysis of  $\text{PbI}_2$  crystallization and perovskite formation. a, XRD spectra of  $\text{PbI}_2$  samples dipped in MAI for 2, 4, 8, 25, 50, 200 and 400 s, showing the (001) reflection of the 2H polytype of  $\text{PbI}_2$ , the (002) and (110) reflections of the tetragonal perovskite. b, FWHM of the (001) reflection of  $\text{PbI}_2$  and of the (110) reflection of the perovskite vs. time for the spectra shown in (a).

Remarkably, the perovskite formation is delayed, with the peaks detected only after 25 s. Instead, the (001) reflection of  $\text{PbI}_2$  undergoes changes. In order to investigate the observations further, we analysed the XRD data in detail. The FWHM from the Voigt function fits of the (001) reflection of  $\text{PbI}_2$  and the (110) reflection of the perovskite, are shown in Figure 3:1b. We observe a narrowing of the (001) reflection of  $\text{PbI}_2$  up to 25 s, which indicates that the reaction commences with an increase in the crystallinity of  $\text{PbI}_2$ . After 25 s, we observe a slight broadening in the  $\text{PbI}_2$  reflection coinciding with the formation of the perovskite, whose reflections are detected from 25 s onward, indicating that the broadening of the  $\text{PbI}_2$  reflection is due to the consumption of the crystalline  $\text{PbI}_2$  as it forms

perovskite. Thus, upon dipping into MAI, the crystallinity of  $\text{PbI}_2$  increases prior to perovskite formation (depicted in Figure 3:2a). This conclusion is consistent with suggestions reported by Harms et al.[73] and with our previous report[60] where PL imaging indicated that  $\text{PbI}_2$  crystallization is the first step in the sequential deposition, occurring before MAI intercalation commences.

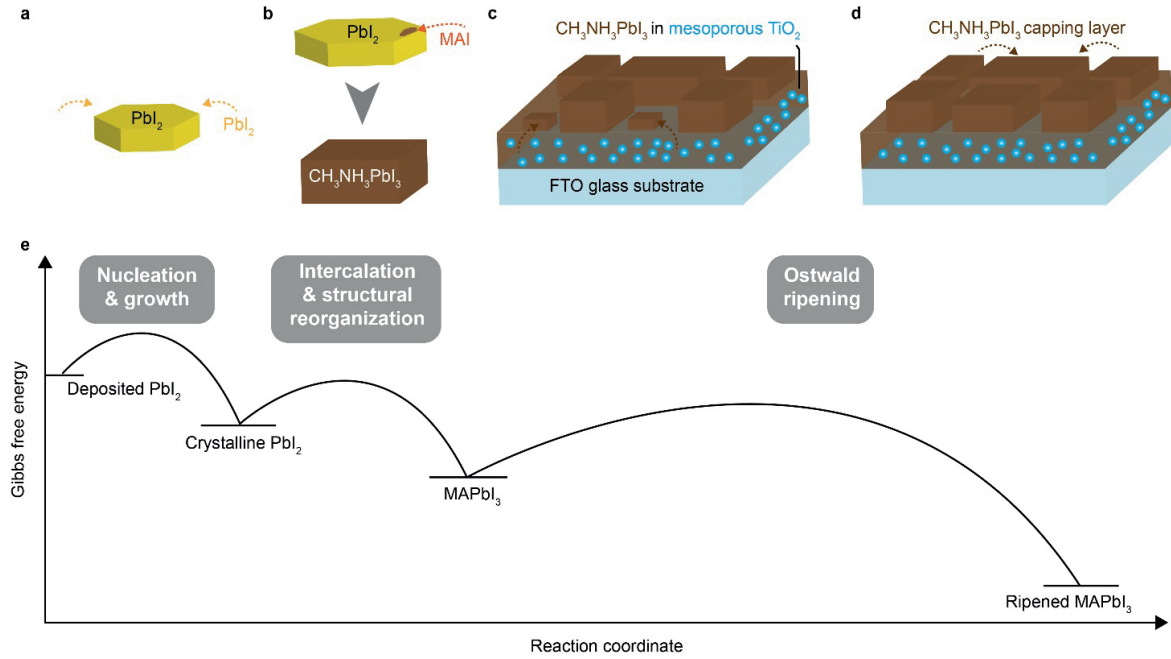


Figure 3:2 Schematic depicting the stages of the reaction in sequential deposition. Dashed arrows indicate mass transfer. a, Nucleation and growth of  $\text{PbI}_2$ . b, Intercalation of MAI and structural reorganization to form  $\text{CH}_3\text{NH}_3\text{PbI}_3$  perovskite. c, Ostwald ripening where perovskite from the mesoporous layer is transported to the capping layer. d, Further Ostwald ripening at longer dipping times where perovskite from the small crystals in the capping layer is transported to larger ones. e, Gibbs free energy shown as a function of the reaction coordinate.

We considered the possibility that the observed changes in the XRD patterns attributed to crystallization could be due to a reorientation of the  $\text{PbI}_2$  crystals in the film upon dipping. To explore this option, we conducted further XRD measurements. Figure 3:3 shows the XRD spectra of unreacted  $\text{PbI}_2$  sample and sample dipped for 4 s in the dark. The (001), (002), (003) and (004) reflections of the 2H polytype of  $\text{PbI}_2$  was assigned and they are in agreement with the literature[97]. For each of these reflections, an increase in the intensity and area with a decrease in the FWHM was observed for the sample dipped for 4 s, as compared to the unreacted  $\text{PbI}_2$  sample. No other reflections, corresponding to other orientations or polytypes of  $\text{PbI}_2$ , are present in the XRD spectra of unreacted  $\text{PbI}_2$  sample, nor do they appear in the sample dipped for 4 s. Therefore, the changes in the XRD profile point to an increase in crystallinity of the  $\text{PbI}_2$  film, rather than a reorientation of crystals in the film.

We also investigated whether a solvent effect involving a lower solubility of  $\text{PbI}_2$  in 2-propanol increases crystallinity upon dipping. XRD measurements and analysis were conducted on an unreacted  $\text{PbI}_2$  film and a film dipped in pure 2-propanol for 25 s. The FWHM from the Voigt function fits of the

(001) reflection of the 2H polytype of  $\text{PbI}_2$  and the corresponding height of the platelet obtained using the Scherrer equation are presented in Table 3:1. No significant increase in the height of the platelets was seen upon dipping in pure 2-propanol for 25 s, upon comparison with the unreacted  $\text{PbI}_2$  film. This confirms that the crystallization phenomenon is not due to an effect of the solvent.

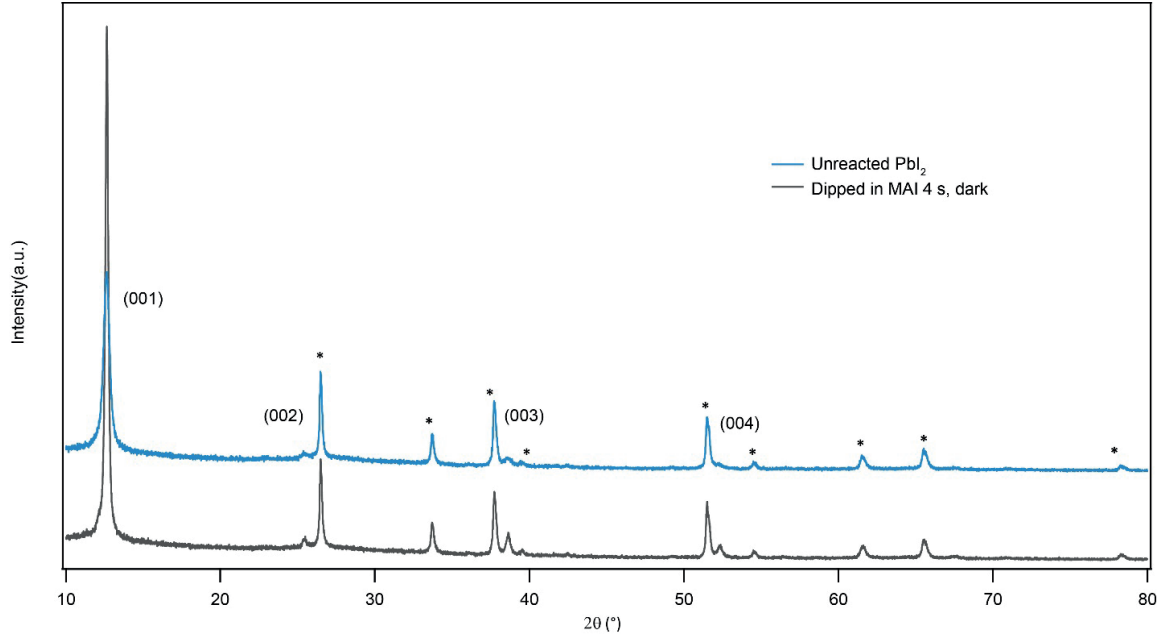


Figure 3:3 XRD spectra of unreacted  $\text{PbI}_2$  sample and sample dipped in MAI solution for 4 s in the dark. The (001), (002), (003) and (004) reflections of the 2H polytype are indicated and reflections from the FTO have been indicated with \*.

Conditions	FWHM(°)	Platelet height(nm)
Unreacted $\text{PbI}_2$ film	0.3531	22
Dipped in 2-propanol for 25 s	0.3441	23

Table 3:1 FWHM of the (001) reflection of the 2H polytype of  $\text{PbI}_2$  and the corresponding height of the platelet from the Scherrer equation.

The crystallization of the partly amorphous  $\text{PbI}_2$  film, rather than the direct formation of the crystalline perovskite, is explained by Ostwald's step rule. It states that the final stable phase is formed through consecutive steps with increasing thermodynamic stability[46]. In our case, the  $\text{PbI}_2$  is the phase that nucleates first, as depicted in Figure 3:2. The nucleation mechanism in the  $\text{PbI}_2$  film was investigated in detail in the previous chapter and report[60].

### Intercalation and structural reorganization

At this point, we look at the progress of the reaction using SEM images of  $\text{PbI}_2$  films dipped in a MAI solution for different periods. The unreacted  $\text{PbI}_2$  film is planar as seen in Figure 3:4a. The growth of

nuclei in the hexagonal platelet structure characteristic of the 2H polytype of  $\text{PbI}_2$ [73-75], is clearly visible in Figure 3:4b which shows a sample dipped in MAI for 2 s. After the partial crystallization of  $\text{PbI}_2$ , the reaction of the crystalline  $\text{PbI}_2$  proceeds via the intercalation of MAI between the layered  $\text{PbI}_2$  and structural reorganization to form the perovskite, as mentioned in the literature[31, 73]. Ahmad et al.[100] investigated the phenomenon of intercalation and showed that controlling reactant concentrations is crucial for optimal intercalation. The report by Liu et al.[101] indicates that the intercalation of MAI starts at grain boundaries and defects in the crystalline  $\text{PbI}_2$ . This onset and the subsequent structural reorganization to form the perovskite are shown schematically in Figure 3:2b.

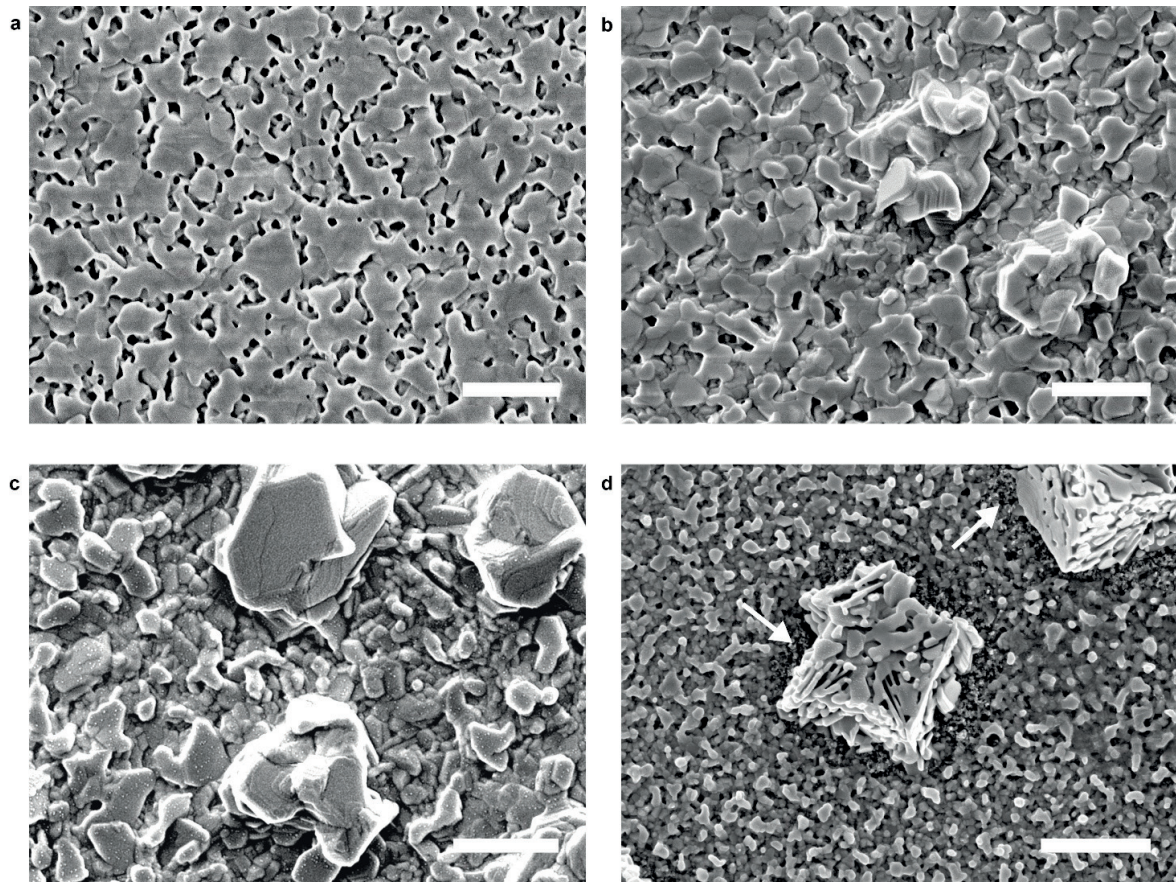


Figure 3:4 Perovskite formation with time studied using SEM. a, Unreacted  $\text{PbI}_2$  film. b, Sample dipped for 2 s showing the growth of nuclei as hexagonal platelets of  $\text{PbI}_2$ . c, Sample dipped for 4 s showing hexagonal platelets of  $\text{PbI}_2$  on the crystal surfaces. d, Sample dipped for 8 s showing the textured crystals. Scale bars (a-c), 0.5  $\mu\text{m}$ . (d), 1  $\mu\text{m}$ .

In Figure 3:4c, we observe that platelets are visible after dipping for 4 s indicating that intercalation has not commenced. The texturing seen in Figure 3:4d, on a sample dipped for 8 s, is investigated further subsequently. We see that areas in the image, which are localized around the crystals, are devoid of  $\text{PbI}_2$  and the mesoporous scaffold is exposed (indicated with arrows). This points to the transport of  $\text{PbI}_2$  during its crystallization, through the MAI solution or along the sample surface, in



addition to in situ crystallization. This finding is in agreement with the nucleation and growth mechanism proposed in the previous chapter and publication[60].

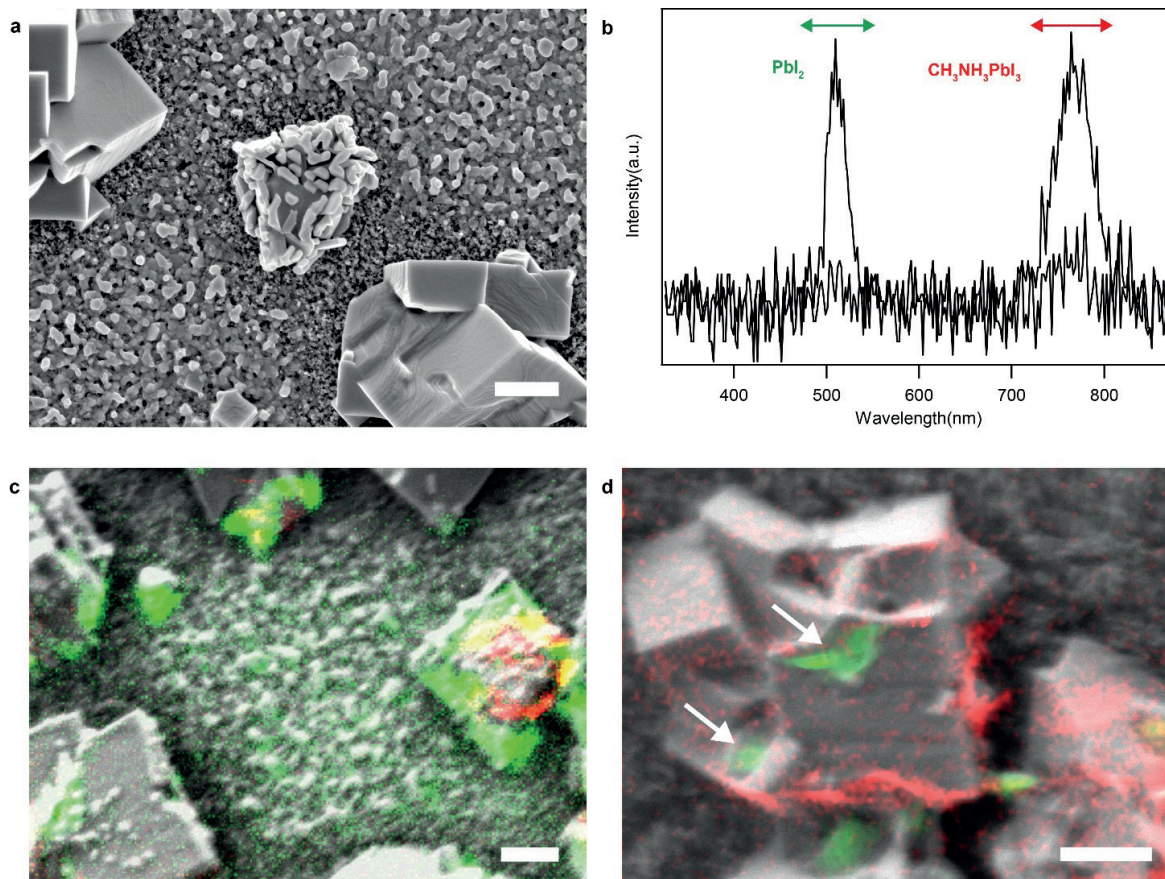


Figure 3:5 Cathodoluminescence study on films of intermediate conversion. a, SEM image of sample dipped for 10s with clusters visible on the crystals. Scale bar, 0.5  $\mu\text{m}$ . b, CL spectra taken at two different points on the same sample.  $\text{PbI}_2$  emission between 480 and 550 nm is assigned green and perovskite emission between 720 and 810 nm is assigned red. c, Pseudocolour CL image overlay on SEM image of the same sample showing mixed crystalline aggregates composed of perovskite and  $\text{PbI}_2$ . Scale bar, 0.5  $\mu\text{m}$ . d, Pseudocolour CL image overlay on SEM image. The crystal is perovskite while the clusters (indicated with arrows) on it are identified as  $\text{PbI}_2$ . Scale bar, 0.5  $\mu\text{m}$ .

Looking at a sample dipped for 10 s, distinct clusters are seen on the surface of the crystal in Figure 3:5a. SEM-CL measurements were made on the same sample to identify the composition of these clusters that evolved from the textured crystals seen in Figure 3:4d. CL spectra obtained at two different positions on the sample have been shown in Figure 3:5b. The emission between 480 and 550 nm, attributed to  $\text{PbI}_2$ , is assigned green and the emission between 720 and 810 nm, attributed to perovskite, is assigned red. In Figure 3:5c, we see that both red and green emissions originate from the textured crystals, showing that these are mixed crystalline aggregates composed of perovskite and  $\text{PbI}_2$ , formed due to partial MAI intercalation and structural reorganization. These mixed crystalline aggregates have so far never been reported. Green emission, indicated with the arrows in Figure 3:5d,

identifies the clusters on the crystal as  $\text{PbI}_2$ , while the red emission from the underlying crystal shows that it is perovskite.

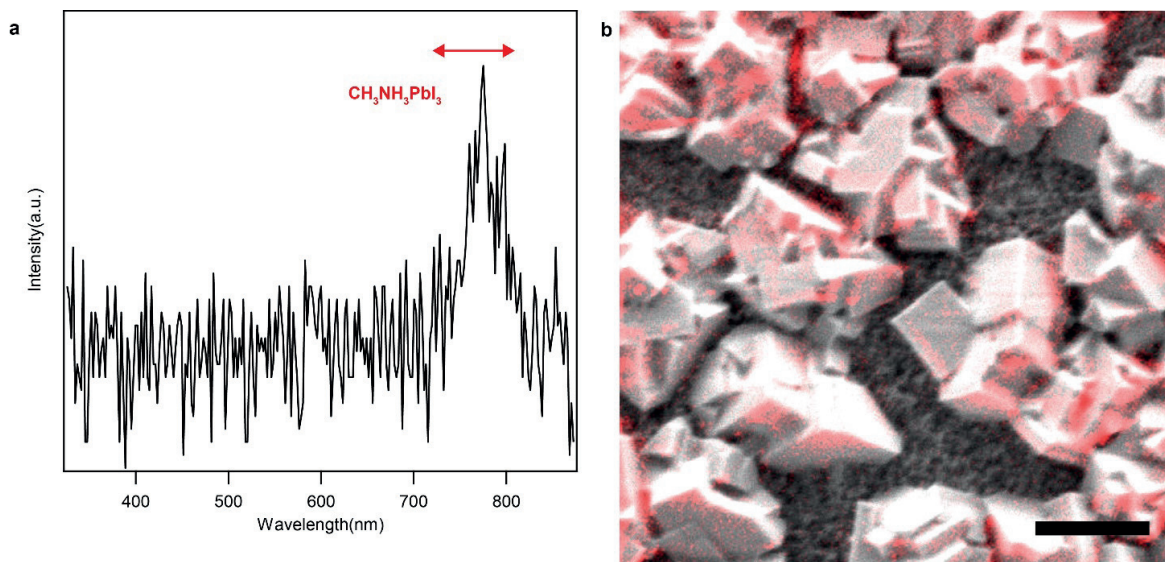


Figure 3:6 Cathodoluminescence study on a sample dipped for 60 s for nearly complete conversion. a, CL spectrum at a point on a sample. The emission between 720 and 810 nm, attributed to perovskite, is assigned red. b, Pseudocolour CL image overlay on a SEM image of the same sample. Scale bar, 1  $\mu\text{m}$ .

The perovskite emission is strongest at the edges of the perovskite crystals, as seen in Figure 3:5d and in the sample of nearly complete conversion shown in Figure 3:6b. The CL signal arises primarily from the excitation volume due to the electron beam on the sample and the electron penetration depth is indicative of the excitation volume. Reports on other semiconductors indicate that while operating at low voltages, which give rise to lower penetration depths, the contribution of the surface is higher as compared to the bulk[102]. In the present study, a low voltage of 2 kV was chosen since the clusters of  $\text{PbI}_2$ , which were of interest, were present on the surface of the crystals. Therefore, lower CL intensity was anticipated from the faces of the perovskite crystals compared to their edges.

### Ostwald ripening

It is interesting to look into samples dipped in a MAI solution for extended periods, long after most of the  $\text{PbI}_2$  has been converted to perovskite. The presence of residual  $\text{PbI}_2$  is investigated later. Cuboids of perovskite lying over the mesoporous layer, make up the capping layer[103] and SEM images in Figure 3:7 show the capping layer of successive samples of long dipping times of 400 s and 800 s. Comparing these images, we observe an increase in the surface coverage of the capping layer, though dipping times are well beyond the point of complete  $\text{PbI}_2$  conversion. These findings support the hypothesis of Ostwald ripening taking place in the film, as previously suggested in the literature[31, 77]. This thermodynamically driven phenomenon involves the transport of matter from smaller

crystals to larger ones. During the initial stages of Ostwald ripening, depicted in Figure 3:2c, perovskite formed in the mesoporous layer is transported to add to minute crystals on the surface, thereby increasing the surface coverage.

Upon dipping even longer (i.e. for thousands of seconds), small crystals in the capping layer dissolve to add to the growth of the larger ones as shown in Figure 3:2d. The disappearance of the smaller crystals would decrease the surface coverage. Cao et al.[77] investigated Ostwald ripening for very long dipping times and showed that the large crystals with low surface coverage were indeed obtained as a result of the extensive ripening phenomenon and this decreased the solar cell efficiency. Thus, dipping beyond the point of complete conversion of  $\text{PbI}_2$  to perovskite, which results in Ostwald ripening, is unfavourable. Further discussion on this aspect will be taken up subsequently.

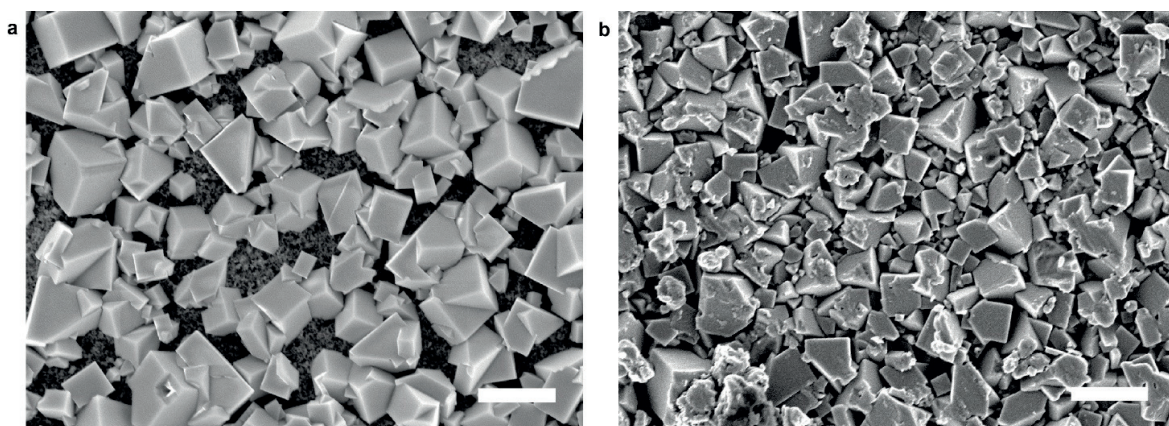


Figure 3:7 SEM images of perovskite films with increasing dipping times showing Ostwald ripening. a, Dipped for 400 s. b, Dipped for 800 s. Scale bars (a- b), 1  $\mu\text{m}$ .

### 3.2.2 Confocal laser scanning fluorescence microscopy

At this point, we delve further into the directionality of the reaction and limitations that result in the presence of residual  $\text{PbI}_2$  in the film. To spatially resolve the conversion of  $\text{PbI}_2$  within mesoporous layers in addition to the capping layer, we used CLSM innovatively to obtain cross-sectional images. Cross-sectional CLSM images allow us to study the different layers in vertical cross sections of solar cells, not just the perovskite film surface. Figure 3:8a shows the different parts of a sample that can be mapped using both, standard surface imaging and our cross-sectional imaging technique together, to obtain a complete description of the sample. Such cross-sectional CLSM imaging for perovskite films will be demonstrated here for the first time.

Samples with a larger  $\text{Al}_2\text{O}_3$  mesoporous layer, approximately 2.5  $\mu\text{m}$  thick, were imaged since standard samples could not be imaged due to the resolution limit of the technique. Nevertheless, insights obtained here, such as any directionality of the conversion reaction, would be applicable to standard

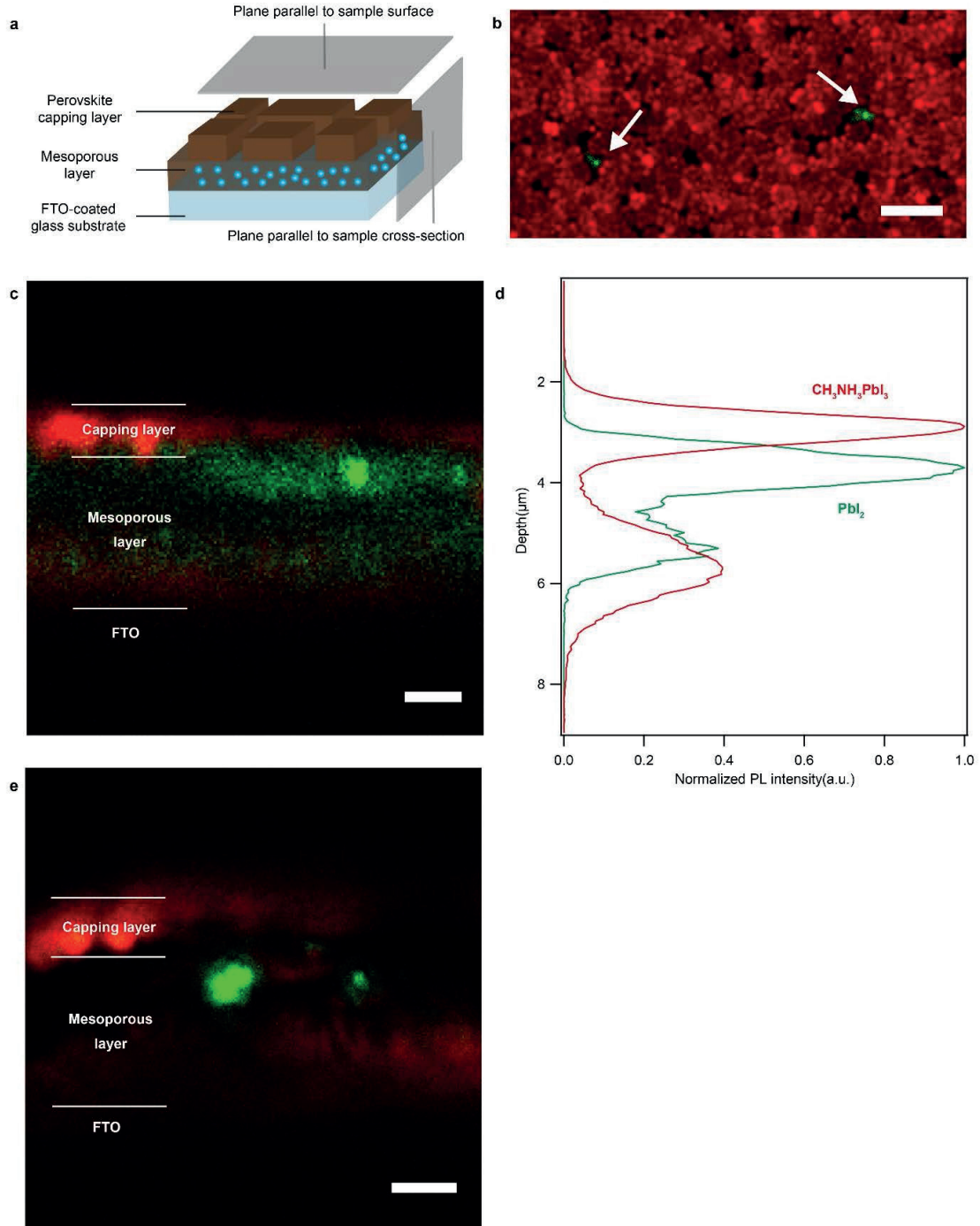


samples in a similar manner. The difference in the reaction for these two samples would possibly be that more time is needed to fully convert a thicker  $\text{PbI}_2$  layer as demonstrated below. Moreover, our results are particularly relevant for preparing solar cells in the architecture proposed by Mei et al.[28] Their cells have a double layer of mesoporous  $\text{TiO}_2$  and  $\text{ZrO}_2$  amounting to about  $3\ \mu\text{m}$ , as a scaffold infiltrated with perovskite and covered by a porous carbon film instead of a hole conductor.

Images of our thick sample, dipped for 60 s, resulting in intermediate conversion, are shown in Figure 3:8b and Figure 3:8c. Emission collected between 500 and 550 nm is attributed to  $\text{PbI}_2$  and represented as green, while the emission between 700 and 800 nm is attributed to perovskite and assigned red[60]. In the surface view shown in Figure 3:8b, unconverted  $\text{PbI}_2$ , indicated with arrows, is visible inside the mesoporous layer, which is exposed between the perovskite crystals of the capping layer.  $\text{PbI}_2$  underneath the perovskite capping layer is not detectable, due to the strong absorption of the perovskite. However, it is seen in the cross-sectional image in Figure 3:8c. This is feasible as the plane chosen for cross-sectional imaging is perpendicular to that used for obtaining surface images (Figure 3:8a) and the perovskite crystals of the capping layer are not in the way to hamper detection of the  $\text{PbI}_2$  emission. Thus, our novel cross-sectional CLSM imaging technique has enabled the mapping of unreacted  $\text{PbI}_2$  in the mesoporous layer for the first time (Figure 3:8c). Obtaining such information was not feasible with standard surface imaging, where layers lying beneath one another are often inaccessible.

The image was analysed by horizontally averaging the  $\text{PbI}_2$  and perovskite emission, followed by normalization of the two curves that are plotted as a function of depth in Figure 3:8d. The consumption of  $\text{PbI}_2$  in the over-layer results in the formation of the highly emissive perovskite capping layer. Strikingly, the  $\text{PbI}_2$  at the bottom of the mesoporous scaffold converts to perovskite, before the  $\text{PbI}_2$  located directly below the perovskite capping layer. These observations are consistent with the proposal in the report by Harms et al.[73], that the perovskite forms a compact layer, denying the MAI solution access to the underlying  $\text{PbI}_2$  for conversion.

As mentioned earlier, several reports[33, 77] have demonstrated that residual  $\text{PbI}_2$  is beneficial for solar cell performance. However, residual  $\text{PbI}_2$  has so far never been imaged or localized. Figure 3:8e shows a sample of long dipping time, expected to have nearly complete conversion. We see that unconverted  $\text{PbI}_2$  is clearly visible in green, trapped in the mesoporous layer. This finding addresses long-standing questions regarding the location of the unreacted  $\text{PbI}_2$  in the film[77]. In the cross-sectional images shown in Figure 3:8c and Figure 3:8e, low emission from the  $\text{PbI}_2$  or perovskite in the mesoporous layer may be due to the small size of the crystals, as they are restricted by the pores of the mesoporous layer.



### 3.2.3 In-situ isothermal kinetic monitoring and solid-state kinetic model

To quantify the kinetics of perovskite formation, in-situ isothermal experiments were conducted at reaction temperatures of 10, 15 and 25 °C. Standard  $\text{PbI}_2$  samples, made using a 1.3 M solution as mentioned earlier, were used. The absorbance of the perovskite at 700 nm, was monitored during conversion (see section 3.4: Materials and methods). The ratio of the absorbance at time  $t$  and that after complete conversion is defined as the conversion fraction ( $\alpha(t)$ ;  $0 \leq \alpha(t) \leq 1$ ). It represents the fraction of perovskite formed from the  $\text{PbI}_2$  at time  $t$ . Remnant  $\text{PbI}_2$  that cannot be converted, in spite of further dipping as discussed earlier, is neglected in the present analysis. Smoothed data, represented in terms of the conversion fraction ( $\alpha$ ) vs. time, is presented in Figure 3:9a.

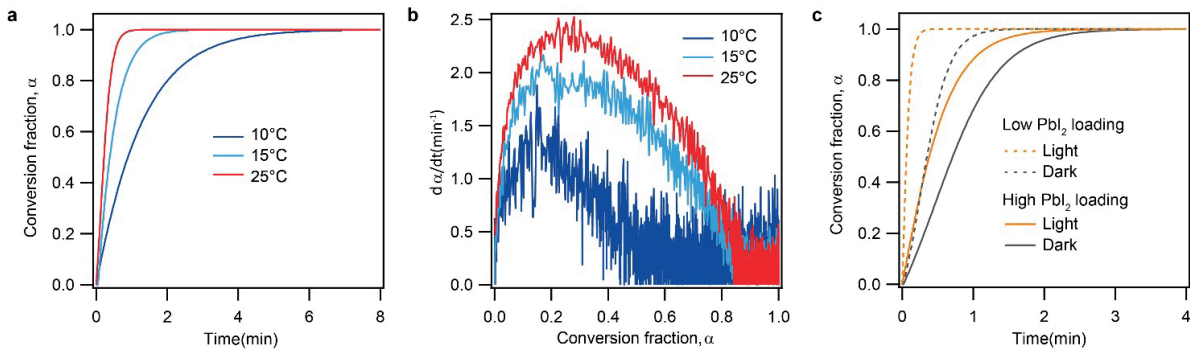


Figure 3:9 In-situ kinetic data of perovskite formation. a, Isothermal kinetic data at 10, 15 and 25°C shown as the conversion fraction ( $\alpha$ ). b, Isothermal reaction rate ( $d\alpha/dt$ ) shown as a function of conversion fraction ( $\alpha$ ) for data in (a). c, Kinetic data for samples of low and high  $\text{PbI}_2$  loading dipped under light and in the dark, shown as the conversion fraction ( $\alpha$ ).

Several solid-state kinetic models have been developed in the literature and they have been summarized in the work by Khawam and Flanagan[104]. They describe a general expression whose mathematical form represents a large number of kinetic models :

$$kt = \alpha^l (1 - \alpha)^m (-\ln(1 - \alpha))^{1/n}$$

Equation 3:1 – General expression for solid-state kinetic models[104]

where  $k$  is the effective reaction rate constant,  $\alpha$  is the conversion fraction,  $t$  is time, and  $l$ ,  $m$  and  $n$  are constants. Numerous models can be expressed based on the values assigned to  $l$ ,  $m$  and  $n$ .

This general equation was taken up to determine the most appropriate model to represent perovskite formation in sequential deposition. The kinetic data shown in Figure 3:9a was fitted by means of non-linear regression with  $k$ ,  $l$ ,  $m$  and  $n$  taken as variables for the fit. We assume that the model parameters ( $l$ ,  $m$ ,  $n$  and  $k$ ) are constant throughout the reaction. Constraints were placed on the variables  $l$ ,  $m$  and  $n$  based on the values they could practically be assigned as reported by Khawam and Flanagan[104]. Data fitting revealed that values of  $l$  and  $m$  were 0, while the values of  $n$  for these reactions were found

to be very close to 1. This showed that the Avrami models were the most suitable to describe the experimental data. Their general form under isothermal conditions is:

$$kt = (-\ln(1 - \alpha))^{1/n}$$

Equation 3:2 – Avrami models under isothermal conditions[104]

where  $n$  is the Avrami exponent;  $k$  is the effective reaction rate constant,  $\alpha$  is the conversion fraction, and  $t$  is time.

The value of  $k$  is expected to increase with temperature and they were found to be 0.8, 2.2 and 3.5 min<sup>-1</sup> for increasing reaction temperatures of 10, 15 and 25 °C respectively. The change in the isothermal reaction rate ( $d\alpha/dt$ ) with the conversion fraction ( $\alpha$ ) has been represented in Figure 3:9b. It is seen that the reaction is accelerating in the initial stages and decelerating in the final stages, with a maxima at an intermediate conversion. This is a characteristic feature of sigmoidal models such as the Avrami models, thereby verifying the aptness of the choice[105]. The advantage of identifying the appropriate model is that upon determining the model parameters once for a temperature of choice, the reaction time can be rapidly determined using the model equation for any degree of conversion. The implications of determining the reaction time are discussed further below. The applicability of this model for a variety of reaction conditions will be taken up next.

### 3.2.4 In-situ kinetic monitoring in the dark and under illumination

In our previous work[60], we demonstrated the effect of light on the perovskite formation and the resulting film morphology. To quantify the impact of illumination on the perovskite formation, in-situ kinetic experiments were conducted at room temperature, in the dark and under illumination (see Materials and methods: section 3.4).

Bi et al.[69] demonstrated that increasing the concentration of the PbI<sub>2</sub> solution would lead to better pore filling of the mesoporous scaffold, resulting in higher PbI<sub>2</sub> loading. Using PbI<sub>2</sub> solutions of concentrations greater than 1 M gives such high PbI<sub>2</sub> loading that it results in the formation of an over-layer of PbI<sub>2</sub>. This over-layer of PbI<sub>2</sub> forms a capping layer of perovskite upon dipping in an MAI solution[69]. Thus, differences between perovskite formation in the mesoporous and the capping layer can be studied using samples of different PbI<sub>2</sub> loading. Moreover, we expect thicker PbI<sub>2</sub> layers to take longer to convert to perovskite, which indicates that the kinetic data collected for the two cases is likely to be quite different. Thus, we also include samples of two different levels of PbI<sub>2</sub> loading in this experiment to ensure that these diverse conditions are investigated in the study. We are interested in verifying if their kinetics can be represented well by the model identified earlier.

Samples of low  $\text{PbI}_2$  loading were prepared using a very low concentration  $\text{PbI}_2$  solution (0.25 M, details in section 3.4: Materials and methods) to ensure that the  $\text{PbI}_2$  is present only in the mesoporous layer and in small quantities. After dipping such a sample in a MAI solution, the  $\text{CH}_3\text{NH}_3\text{PbI}_3$  formed remains restricted to the mesoporous layer. On the other hand, samples with high  $\text{PbI}_2$  loading, prepared using a high concentration  $\text{PbI}_2$  solution (1.3 M, details in section 3.4: Materials and methods), have an additional over-layer of  $\text{PbI}_2$ . This results in the presence of perovskite within the mesoporous scaffold and as a capping layer upon dipping in a MAI solution. Such samples of high  $\text{PbI}_2$  loading are the standard samples used throughout this report. The smoothened data, represented as the conversion fraction, is shown in Figure 3:9c.

For the samples of high  $\text{PbI}_2$  loading, the time to achieve 99% conversion was found to be around 2.1 min under light bias and 2.9 min in the dark. The analogous values for the samples of low  $\text{PbI}_2$  loading are 0.3 min and 1.2 min respectively. As expected, we found that under identical illumination conditions, samples of high  $\text{PbI}_2$  loading take longer to convert to perovskite compared to those of low  $\text{PbI}_2$  loading. Remarkably, the conversion is reached in less time upon biasing the samples with light, compared to the reaction in the dark, for both samples. Thus, light accelerates the perovskite formation within the mesoporous scaffold, as well as in the capping layer. Upon fitting the data for samples of high  $\text{PbI}_2$  loading with the Avrami models, the value of  $n$  was obtained as 1.4 and 1.1 for the dark and light bias cases respectively. A higher value of  $k$ ,  $1.8 \text{ min}^{-1}$  is obtained for the reaction under light bias, as compared to the value of  $1.0 \text{ min}^{-1}$  in the dark. This is consistent with the observations in our earlier report[60] where the reaction under light was rapid compared to the dark.

We identified that the Avrami models are the most suitable to represent the in-situ kinetic data for the reaction. They appropriately represent the reaction for various  $\text{PbI}_2$  loading levels and light intensities, in addition to our previous demonstration for different reaction temperatures, indicative of robustness.

The model facilitates the estimation of the reaction time for a given conversion at different reaction conditions, including the point of complete conversion. The loss in solar cell performance due to Ostwald ripening, as discussed earlier, can be eliminated by identifying the point of complete conversion for a given set of reaction conditions and choosing that as the dipping time. Thus, the model presents a convenient and rapid option for ascertaining the reaction time for complete conversion, a previously uncertain parameter in sequential deposition. This helps address a major source of irreproducibility in perovskite film formation.

### 3.3 Conclusion

Although the sequential deposition method is widely used, studies have focused on optimizing the photovoltaic performance, rather than examining the pathway of the reaction and its kinetics. Our present investigation allowed unravelling the salient features of this intriguing and widely applied conversion process. Importantly, contacting the  $\text{PbI}_2$  film deposited on a mesoscopic oxide support with a MAI solution first induces the crystallization of the  $\text{PbI}_2$  film. This is followed by the intercalation of MAI into the  $\text{PbI}_2$  crystal lattice and structural reorganization forming mixed crystalline aggregates of perovskite and  $\text{PbI}_2$  as intermediates.

Cross-sectional CLSM imaging revealed the directionality of the conversion of the  $\text{PbI}_2$  film, showing that the  $\text{PbI}_2$  in the mesoporous scaffold, underneath the capping layer, is the last to convert and that unreacted  $\text{PbI}_2$  is trapped there even after long reaction times. Our identification of trapped, unreacted  $\text{PbI}_2$  in the film addresses open questions raised in the literature[77, 96] regarding the location of residual  $\text{PbI}_2$  in perovskite solar cells. These insights obtained from our pioneering cross-sectional imaging technique were otherwise inaccessible through the traditional surface imaging technique. On a broader note, our innovative demonstration of this technique's potential opens the door for understanding the properties of perovskites in cross sections of solar cells, not just the perovskite surface as presented in the literature[52].

Dipping beyond the point of complete conversion results in Ostwald ripening, which is detrimental to solar cell performance[77]. Thus, identifying the dipping time corresponding to the point of complete conversion is warranted. We found that the Avrami models are best suited to represent the kinetic data and we verified its robustness under different reaction conditions of temperature, film thickness and illumination. The model allows rapid estimation of the dipping time for any conversion, eliminating the need for extensive experiments. We thereby address critical problems in batch-to-batch reproducibility in perovskite film fabrication.

This comprehensive picture of the sequential deposition is essential for control over perovskite film quality, which is critical as it determines device performance[49]. Our findings provide the foundation for the improvement of perovskite film fabrication through sequential deposition for various applications.

### 3.4 Materials and methods

#### 3.4.1 Materials

Materials used in the study were purchased from Sigma-Aldrich or Acros Organics. MAI was prepared as reported in the report by Im et al.[23]. The  $\text{Al}_2\text{O}_3$  paste of particles of 23 nm diameter was prepared in-house. Films for the in-situ kinetic experiments were made using FTO-coated glass substrate (Tec15, Pilkington), while Nippon sheet glass was used for the remaining experiments.

#### 3.4.2 Sample preparation

Films used for experiments, with the exception of CLSM, had a mesoporous layer of 300 nm thickness made using the  $\text{Al}_2\text{O}_3$  nanoparticles. The mesoporous layer was deposited and processed as described by Burschka et al.[31]. A thicker mesoporous  $\text{Al}_2\text{O}_3$  layer of approximately 2.5  $\mu\text{m}$  was deposited for samples for CLSM. For standard samples, a 1.3 M solution of  $\text{PbI}_2$  in N, N-dimethylformamide, kept at 70 °C, was deposited by spin coating at 6500 rpm for 20 s. The sample was then heated at 70 °C for 10 min. A low concentration of MAI solution in 2-propanol (6 mg  $\text{ml}^{-1}$ ) was used in all the kinetic experiments presented, rather than 8 or 10 mg  $\text{ml}^{-1}$  as employed for solar cell fabrication[31], in order to keep the reaction rate sufficiently low so that kinetic features could be monitored and analysed effectively. Samples of specific reaction times were prepared by dipping  $\text{PbI}_2$  films in MAI for the required period, followed by washing in 2-propanol to halt the reaction. They were then heated at 70 °C for 10 min.

#### 3.4.3 X-ray diffraction measurements

The XRD measurements were carried out on an X'Pert MPD PRO from PANalytical operated in the Bragg-Brentano geometry. It has a ceramic tube (Cu anode,  $\lambda=1.54060 \text{ \AA}$ ), a secondary graphite (002) monochromator and a real-time multiple strip X'Celerator detector. The automatic divergence slit and beam mask were adjusted to the dimensions of the films. A step size of 0.002 ° and an acquisition time of up to 5 min  $\text{deg}^{-1}$  was chosen for the scan in Figure 3:1, while a step size of 0.008 ° and an acquisition time of up to 1.5 min  $\text{deg}^{-1}$  was chosen for the scan in Figure 3:3.

#### 3.4.4 Scanning electron microscopy-cathodoluminescence

The SEM-CL measurements were conducted at room temperature using an Attolight Rosa 4634 CL microscope, with a beam probe of 5 nm, an accelerating voltage of 2 kV and a beam current of 20 nA. The CL microscope tightly integrates a high numerical aperture (NA 0.72) achromatic reflective lens within the objective lens of a field emission gun scanning electron microscope (FEG-SEM). The focal plane of the light lens matches the FEG-SEM optimum working distance. The CL collection efficiency is



constant over a 300  $\mu\text{m}$  field of view so that the CL emission can be compared quantitatively between two distinct points. The CL emission was spectrally resolved with a Czerny-Turner spectrometer (320 mm focal length, 150 grooves/mm grating) and detected by an UV-Vis CCD camera.

#### 3.4.5 Confocal laser scanning fluorescence microscopy and image processing

CLSM images were captured using the Leica Application Suite X software on a confocal laser scanning microscope (Leica TCS SP8), using a HC PL APO oil objective (63x/1.40). A pulsed diode laser (440 nm) was used for excitation. The excitation power and the gain were chosen to optimize the dynamic range of the detector (PMT, HyD or HyD SMD). Single plane 512x512 images were acquired at 25°C from a unidirectional scan of 400 Hz speed. Figure 3:8b and Figure 3:8c were imaged using a pinhole size of 1 Airy unit. A pinhole size of 0.628 Airy unit was used to improve signal strength for capturing Figure 3:8e. Figure 3:8b was acquired at a resolution of 72 nm in xy, while it was 46 nm for Figure 3:8c and Figure 3:8e. Image bit depth was 8. Fiji was used for image processing: The two components mapped to different channels were pseudo-coloured. Linear brightness and contrast adjustments were applied to the entire image for each channel. For display, the image in Figure 3:8b was cropped to 36.9x18.45  $\mu\text{m}^2$ , while the images in Figure 3:8c and Figure 3:8e were cropped to show an area of 8x8  $\mu\text{m}^2$  and 14x14  $\mu\text{m}^2$  respectively.

#### 3.4.6 Spectroscopy

The isothermal kinetic data was recorded through absorbance spectroscopy in transmission mode, in a Varian Cary 5 spectrophotometer. The amount of perovskite formed was quantified by monitoring the absorbance of the perovskite at 700 nm wavelength.

The kinetic data of the perovskite formation, in the dark and under light bias, was recorded through absorbance spectroscopy in transmission mode (also at 700 nm), using an integrating sphere of 110 mm diameter in the same spectrophotometer. Dark conditions indicate as dark as achievable with attenuated probe light, while light biasing was achieved using a white LED that supplemented the maximum intensity of the probe light.

A 1.3 M solution of  $\text{PbI}_2$  in N, N-dimethylformamide was used to prepare samples of high  $\text{PbI}_2$  loading. These samples are similar to the standard samples used throughout the report. Thus, these samples were used to conduct the isothermal kinetic study as well. A 0.25 M  $\text{PbI}_2$  in N, N-dimethylformamide solution was used to prepare samples of low  $\text{PbI}_2$  loading for some of the in-situ kinetic experiments.

For both the experiments, mesoporous films infiltrated with  $\text{PbI}_2$  were placed in a cuvette. Using pipettes, MAI solution was added to start the reaction and the reaction was stopped by rapidly replacing the MAI solution in the cuvette with 2-propanol.



# Chapter 4 Crystal coalescence in highly efficient perovskite solar cells

*This chapter was adapted from the following article with the permission of all co-authors and the journal.*

**Postprint version of the article:** B. Roose\*, [A. Ummadisingu](#)\*, J. P. Correa-Baena, M. Saliba, A. Hagfeldt, M. Grätzel, U. Steiner and A. Abate, "Spontaneous crystal coalescence enables highly efficient perovskite solar cells," *Nano Energy*, vol. 39, pp. 24-29, Sep 2017. (doi: 10.1016/j.nanoen.2017.06.037) \*These authors contributed equally to this work.

**My contribution:** Designed the study with B.R. and A.A. Wrote the first version of the paper with B.R. with inputs from A.A. Analysed the XRD data with B.R. Developed the thermodynamic aspects, measured and analysed the TCSPC data.

Perovskite solar cells have recently reached staggering efficiencies, through efforts focused on reducing grain boundaries, by enlarging the size of the crystallites that constitute the perovskite films. This chapter demonstrates that smaller crystallites within perovskite films spontaneously coalesce into larger ones due to the maturation of complete devices stored in the dark at room temperature. We show that crystal coalescence greatly improves the performance of state-of-the-art perovskite solar cells in a planar architecture. Our results reveal the dynamic nature of the morphology of perovskite films and highlight the crucial role that coalescence plays in producing highly efficient devices.

## 4.1 Introduction

As mentioned earlier, perovskite solar cells have rapidly become one of the most promising prototype technologies for low-cost and efficient harvesting of solar energy[35]. Recent reports demonstrated outstanding solar-to-electric PCEs above 22%[29]. Since the first demonstrations by Kim et al.[24] and Lee et al.[25], the main advances have been achieved through engineering the perovskite deposition, with the aim of forming a compact film with homogenous crystallites on the micrometer scale[106, 107]. Several reports have indicated that small crystallites present between larger perovskite domains result in suboptimal charge extraction under stabilized working conditions, such as in maximum power point tracking, or in larger hysteresis under non-stabilized current-voltage ( $J$ - $V$ ) scans[88, 108]. Nevertheless, hysteresis is frequently found to decrease several hours to weeks after device preparation and is often accompanied by an increase in the stabilized PCE[42, 62, 109, 110]. Improved performance or self-healing activated by light is well documented and it has been associated with the passivation of defects within the perovskite[61, 111]. However, performance improvements have also been observed in devices stored in the dark at room temperature[42]. This is consistent with the common and often undisclosed practice of storing devices for several hours to a few days after

preparation, and before measuring the first J-V curve[112]. The absence of any external influence suggests that a spontaneous mechanism is actively improving the devices during storage.

Here, we show that coalescence of small perovskite crystallites into larger crystallites takes place in perovskite films stored in the dark at room temperature. SEM and XRD were employed to investigate the evolution of the perovskite film morphology. This study demonstrates that small perovskite crystallites in the film decrease in number and the average crystal size increases over the timescale of a few weeks. We have prepared state-of-the-art perovskite solar cells and then used TCSPC, intensity modulated photocurrent spectroscopy (IMPS) and photovoltaic performance measurements to demonstrate that perovskite crystal coalescence is a spontaneous, self-healing mechanism, which is inadvertently exploited to achieve high stabilized efficiencies.

## 4.2 Results and discussion

### 4.2.1 Photovoltaic performance

We prepared state-of-the-art perovskite solar cells in an inert atmosphere, using a lead-based mixed halide (bromine and iodine) and cation (methylammonium and formamidinium) perovskite in a planar device architecture, as reported in the literature[113]. Figure 4:1 shows the J-V curves of the same perovskite solar cell collected under identical conditions, 2 days and again 28 days after preparation and storage in dry air (below 1% relative humidity) at room temperature in the dark. The device performance parameters are listed in Table 4:1. It is evident that hysteresis is reduced and performance has improved with storage. As previously reported, we observed the opposite trend, i.e. reduced performances and improved hysteresis, when J-V curves were collected every day or when devices were stored in ambient light[29]. Table 4:2 shows the photovoltaic performance of an initially poor-performing batch. In some cells, the PCE can increase by up to 25% after a few days or weeks of storage in the dark. Interestingly, devices with an initial lower PCE show more improvement and they tend to come closer to the highest performing ones.

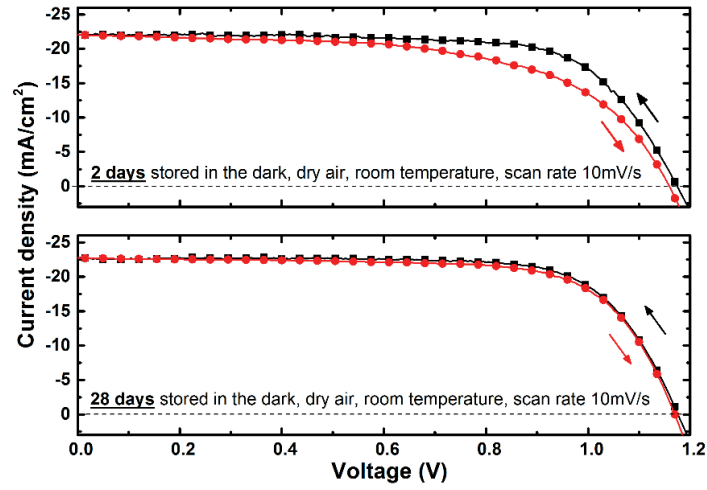


Figure 4:1 Current density-voltage (J-V) curves for a perovskite solar cell at a, 2 and b, 28 days after preparation, storing the device in the dark and in dry air at room temperature. The J-V curves were measured at a scan rate of  $10 \text{ mV s}^{-1}$  from forward bias to short circuit condition and from short circuit condition to forward bias under AM1.5 simulated solar light illumination. The device was not preconditioned under light or voltage bias before each J-V scan. The active area was defined by a shadow mask with an aperture of  $0.16 \text{ cm}^2$ .

Storage	Light intensity ( $\text{mW cm}^{-2}$ )	Scan direction	$J_{sc}$ ( $\text{mA cm}^{-2}$ )	$V_{oc}$ (mV)	Fill factor	PCE(%)
2 days	97.1	Forward	21.9	1159	0.60	15.6
		Backward	22.0	1175	0.70	18.7
28 days	100.5	Forward	22.7	1170	0.71	18.7
		Backward	22.7	1176	0.73	19.3

Table 4:1 Photovoltaic performance parameters: open-circuit voltage ( $V_{oc}$ ), short circuit current ( $J_{sc}$ ), fill factor (FF) and maximum power conversion efficiency (PCE) extracted from the forward and backward J-V scans in Figure 4:1.

Having eliminated the influences of light, water and applied voltage during storage, oxygen remains as the only external agent that may potentially affect the device performance. Oxygen is known to interact with metal oxides, organic semiconductors and the perovskites employed in these devices and modifies their electronic properties[114-118]. However, oxygen permeation within the device takes place on the timescale of a few hours and is likely to saturate before the first J-V curve is collected[116, 119, 120]. Therefore, oxygen and other external stimuli can be ruled out as playing an important role in the improvement of PCEs during storage in the dark at room temperature.

Storage	$J_{sc}$ ( $\text{mA cm}^{-2}$ )	$V_{oc}$ (mV)	Fill factor	PCE(%) Forward scan	PCE(%) Backward scan
2 days	$21.1 \pm 1.4$	$1133 \pm 11$	$0.63 \pm 0.10$	$13.3 \pm 1.2$	$15.1 \pm 2.7$
28 days	$21.9 \pm 0.5$	$1160 \pm 13$	$0.66 \pm 0.03$	$16.5 \pm 0.5$	$16.7 \pm 0.9$

Table 4:2 Averaged photovoltaic parameters from 5 identically-prepared devices: open-circuit voltage ( $V_{oc}$ ), short circuit current ( $J_{sc}$ ), fill factor, power conversion efficiency (PCE) as measured in the forward and backward direction. A  $0.148 \text{ cm}^2$  aperture was placed on the active area for measurement. Devices were stored in the dark and in dry air (below 1% relative humidity) at room temperature.

## 4.2.2 Opto-electronic characterization

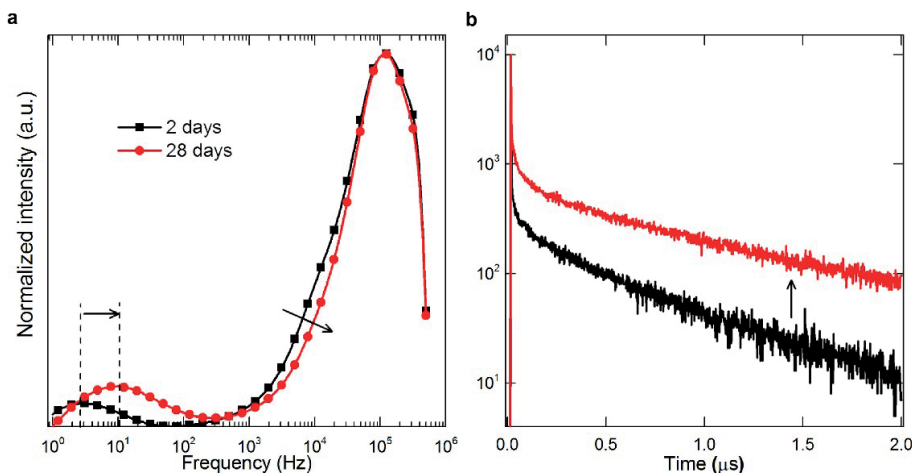


Figure 4:2 Data collected 2 and 28 days after the sample preparation. The samples were stored in the dark and in dry air at room temperature. a, Imaginary part of the intensity modulated photocurrent spectra of a complete perovskite solar cell. The spectra were normalized to the highest peak at  $10^5$  Hz. b, TCSPC measurement of a perovskite film deposited on a microscope glass slide. The sample was excited at 480 nm from the perovskite side and the emission at 760 nm from the same side was monitored.

To shed light on the origin of the PCE improvement due to dark storage, we performed IMPS measurements on a complete device. Figure 4:2a shows the imaginary component frequency spectra of the current response to the light modulated intensity (10% of the stationary value) around  $100 \text{ mW cm}^{-2}$ , collected from the same device 2 and 28 days after preparation. The spectra show three main features, which have been reported earlier by Correa-Baena et al.[88] and Seo et al.[108] for similar perovskite solar cells. The feature at low frequencies ( $10^0 - 10^2$  Hz) stems from the resonant frequencies of ion and ion vacancy migration within the perovskite lattice[88, 108, 121]. Here, we note that this feature is shifted towards higher frequencies or faster responses in the spectrum for the 28-day-old sample. According to the study of Correa-Baena et al.[88], a faster ionic response is correlated with the presence of larger crystallites within the perovskite film. Moving to higher frequencies, there are two more features that have been assigned to the resonant frequencies of the charges within the perovskite film and the other device components, such as the hole and the electron transporting layers. While the peak at the highest frequency ( $10^5$  Hz) is unaffected, the shoulder at  $10^4$  Hz is less pronounced after a long period of storage in the dark. Seo et al.[108] demonstrated that this behaviour is correlated to a reduced concentration of smaller crystallites within the perovskite film, which results in better device performance.

To further investigate the changes in the perovskite film due to storage in the dark, we performed TCSPC measurements. Figure 4:2b displays the decay traces measured 2 and 28 days after preparation of the perovskite film, which was deposited on a glass microscope slide. The data between  $0.15 \mu\text{s}$  and



1.95  $\mu\text{s}$  was fitted to the exponential function shown below (fits shown in Figure 4:3). The parameters obtained from the fits are shown in Table 4:3.

$$y = y_o + A_o e^{\frac{-t}{\tau}}$$

Equation 4:1 – Mono-exponential function used for fitting TCSPC data

where  $y$  is the intensity as a function of time,  $y_o$  is the baseline intensity,  $A_o$  is the pre-exponential constant,  $t$  is time and  $\tau$  is the decay time.

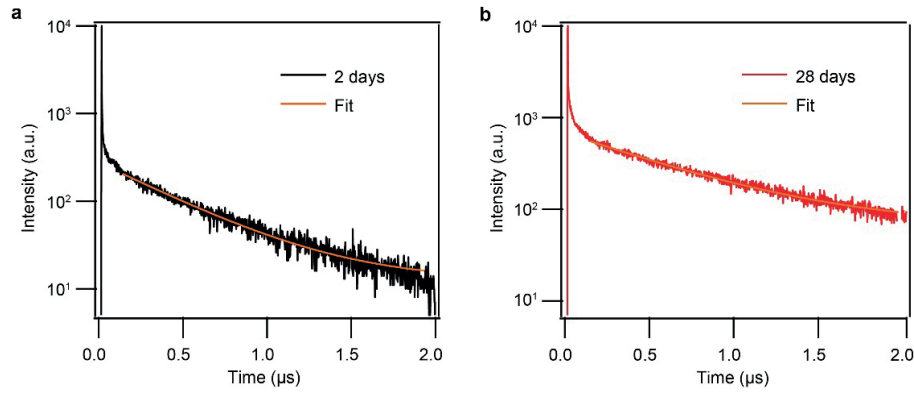


Figure 4:3 Mono-exponential function fits of the TCSPC data of the perovskite film a, after 2 days and b, after 28 days of storage in the dark.

Storage	$y_o$	$A_o$	$\tau(\mu\text{s})$
2 days	$12.45 \pm 0.66$	$264.68 \pm 2.05$	$0.452 \pm 0.006$
28 days	$64.66 \pm 2.20$	$616.25 \pm 2.99$	$0.643 \pm 0.009$

Table 4:3 Mono-exponential function fit parameters of the perovskite film 2 days and 28 days after storage in the dark.

The photoluminescence decay time was indeed found to be longer after 28 days of storage in the dark and in dry air (0.64  $\mu\text{s}$ ) compared to that after 2 days (0.45  $\mu\text{s}$ ). This points to a reduction in the non-radiative recombination through electronic defects or trap states within the perovskite film[122]. We have excluded from our experiment any external agent capable of passivating defects, such as water and light[52]. Therefore, the increase in crystallite size with storage appears to be the most plausible explanation for the increase in photoluminescence decay time. As defects are more numerous at or near grain boundaries[123, 124], the number of trap states is greatly reduced by enlarging the size of crystallites within the perovskite film.

Therefore, the opto-electronic characterization suggests that storing perovskite solar cells under dry conditions in the dark for a few weeks results in reduced non-radiative charge recombination and improved charge transport, which may be correlated to morphological changes in the perovskite film.

### 4.2.3 Film morphology

To look into this possibility, we studied the morphological evolution of the perovskite film by top-view SEM analysis. The images were collected from the same area of the film 2 days (Figure 4:4a) and 28 days after preparation and storage (Figure 4:4b) at room temperature in the dark under dry conditions. Two adjacent crystals in the centre of Figure 4:4a have merged to form a larger single crystal in Figure 4:4b, eliminating one grain boundary. To show the statistical relevance of this effect and to exclude electron-beam-induced changes to the surface, the distribution of grain areas (Figure 4:4c) was extracted from larger SEM top-view images (Figure 4:4d and Figure 4:4e) that were collected several  $\mu\text{m}$  apart. A statistical analysis revealed a significant reduction in the number of small crystallites (*i.e.*  $<0.025\mu\text{m}^2$ ). We found that the number of grains per surface area is 66% lower and the average crystal size almost doubles after 28 days storage. Detailed data is presented in Table 4:4, including the size distribution for a sample aged for 14 days. We attribute this observation to the phenomenon of coalescence, where adjoining crystals fuse to form larger crystals.

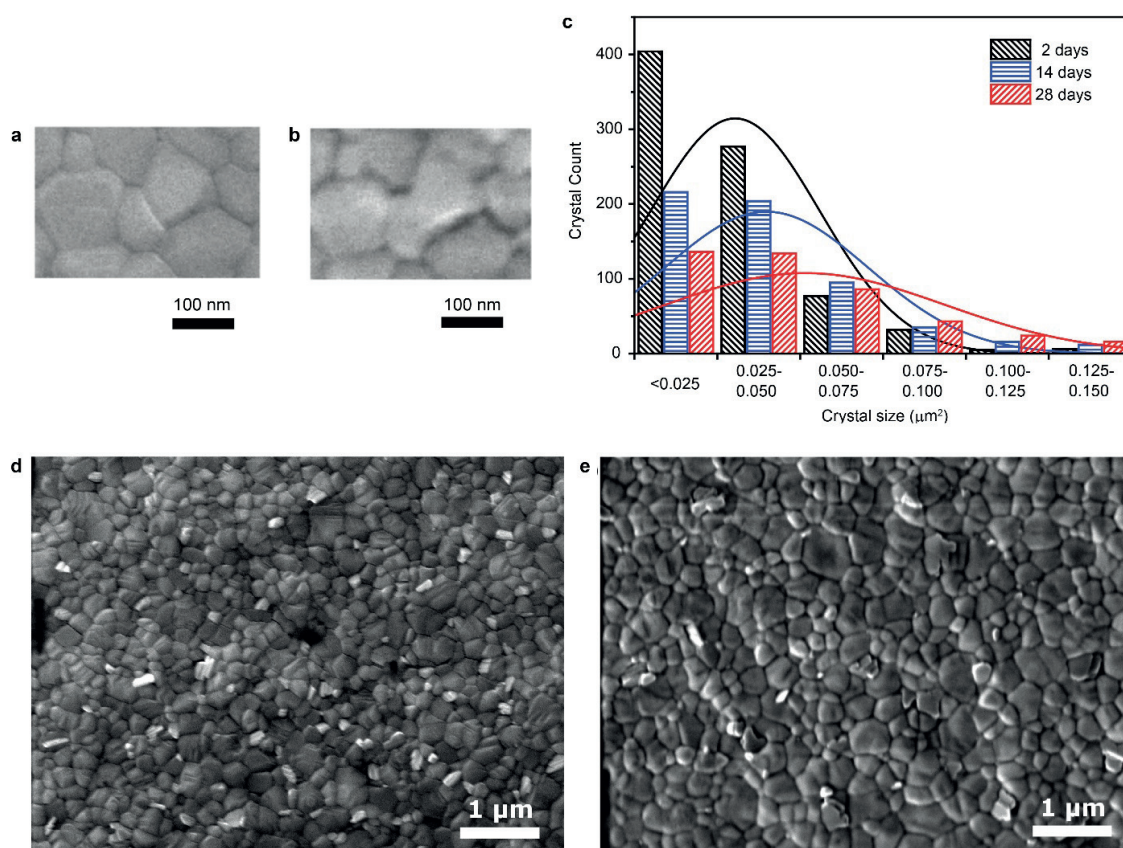


Figure 4:4 SEM images of a perovskite film stored for a, 2 days and b, 28 days in dark and dry air at room temperature. c, Statistical distribution of areas of crystals for 2, 14 and 28 days. Data for 2 and 28 days extracted from the SEM top views in d, 2 days and e, 28 days respectively.

This phenomenon has been reported to take place in thin films of various materials including metals[125] and polymers[126] during processes such as aging and sintering[127]. Solvent annealing[128] and Ostwald ripening[129] were systematically exploited to increase the average crystal size and thus the photovoltaic performance in perovskite solar cells. Recently, Sheng et al.[130] also reported a spontaneous increase in the average crystal size in  $\text{CH}_3\text{NH}_3\text{PbBr}_3$  perovskite film stored in the dark at room temperature, but its potential impact on perovskite solar cells performance remained unexplored.

Days	<0.025	0.025 - 0.050	0.050 - 0.075	0.075 - 0.100	0.100 - 0.125	0.125 - 0.150	Average size
2	404	277	77	32	5	6	0.030
14	216	204	95	35	16	12	0.040
28	136	134	86	43	24	16	0.052

Table 4:4 Number of crystals extracted from SEM top view images of a sample after 2, 14 and 28 days of storage. All crystal surface areas are in  $\mu\text{m}^2$ .

To prove that the observed increase in crystal size in the SEM micrographs is not merely a surface effect, XRD measurements, which provide information about the crystallinity of the film, were performed. XRD measurements of the perovskite film conducted 2 and 28 days after preparation are shown in Figure 4:5.

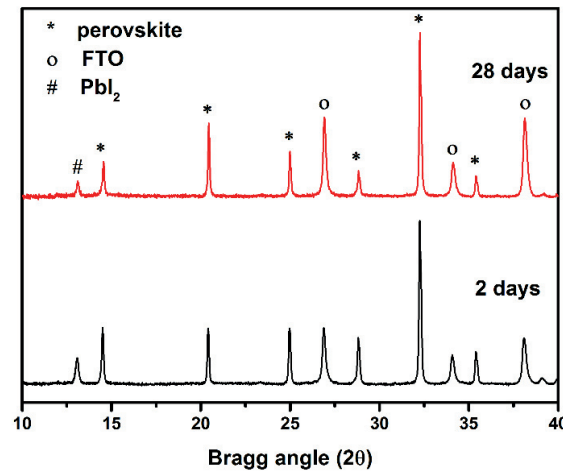


Figure 4:5 X-ray diffraction patterns collected 2 and 28 days after perovskite film preparation. The samples were stored in the dark and in dry air at room temperature.

All peaks can be assigned to the tetragonal phase of the perovskite, the 2H polytype of  $\text{PbI}_2$  (present as excess in the perovskite film) and the FTO from the substrate[99]. The Miller indices, the relative intensity of the peaks and the extracted crystal sizes are given in Table 4:5. The average crystallite size of perovskite crystals was extracted for both measurements by subtracting the instrumental broadening and then using the Scherrer equation[63]. For most of the crystal orientations shown in

Table 4:5, the crystallite size significantly increases after storage in the dark. This is in agreement with the SEM results discussed earlier. The changes in the relative peak intensities suggest that the coalescence is preferential in certain crystallographic orientations compared to others. A theoretical discussion of these observations based on thermodynamic considerations will be taken up next.

Angle(2 $\theta$ )	hkl	Intensity 2 days	Intensity 28 days	Size(nm) 2 days	Size(nm) 28 days
14.5	002, 110	0.34	0.21	270 $\pm$ 10	380 $\pm$ 10
20.4	112, 020	0.34	0.44	440 $\pm$ 10	840 $\pm$ 10
25.0	022	0.34	0.27	340 $\pm$ 10	1400 $\pm$ 10
28.8	004, 220	0.28	0.16	330 $\pm$ 10	340 $\pm$ 10
32.3	114, 222, 130	1.00	1.00	300 $\pm$ 10	380 $\pm$ 10
35.4	024, 132	0.20	0.12	160 $\pm$ 10	190 $\pm$ 10

Table 4:5 Miller indices (hkl), peak intensity normalized to the intensity of the perovskite peak at 32.3 2 $\theta$  and the crystal size extracted from the spectra in Figure 4:5.

#### 4.2.4 Thermodynamics of coalescence

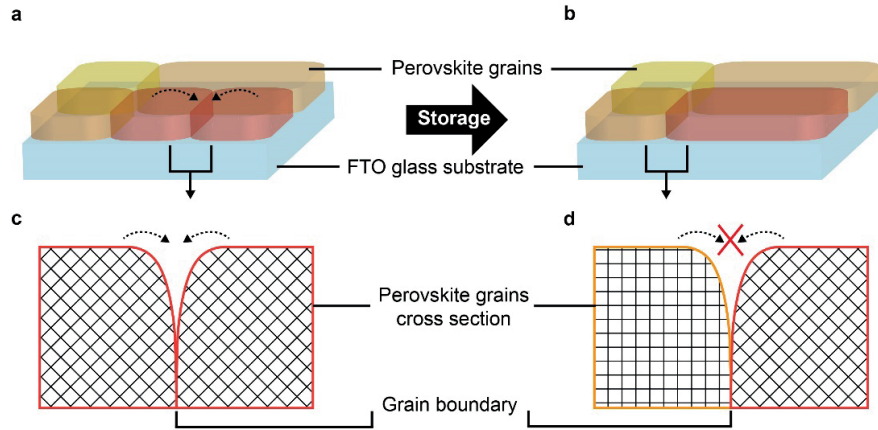


Figure 4:6 Schematic of crystal coalescence in a perovskite film. a, An as-prepared film of crystals with a small crystallographic misorientation at the grain boundary shown in red. Arrows indicate the grain boundary of interest between these crystals. b, Film after dark storage, showing the coalescence of these crystals. c, Cross sectional view of crystals with a small crystallographic misorientation at the grain boundary which preferentially coalesce. d, Cross sectional view of crystals with a large crystallographic misorientation at the grain boundary which do not coalesce.

The grain-grain orientation is of importance for coalescence, since the surface energy associated with each grain boundary varies based on the crystallographic misorientation between the contacting faces[126]. If the degree of misorientation at the grain boundary is low, the energy of the grain boundary is also low and these crystals preferentially coalesce, as shown in the schematic in Figure 4:6a and Figure 4:6c. On the other hand, a high degree of misorientation at the grain boundary, as shown in Figure 4:6b and Figure 4:6d, is unfavourable for coalescence. This explains the directional selectivity of coalescence shown in Table 4:5. On this basis, we distinguish coalescence from the Ostwald ripening phenomena reported in the literature[130], which also causes the average size of

perovskite crystals to increase. Ostwald ripening involves the transfer of material from the smaller crystals to the larger ones through an external phase, which acts as a transfer medium (for instance, 2-propanol solution[130]). In contrast, coalescence involves the selective fusion of adjacent crystals at their grain boundary.

### 4.3 Conclusion

This chapter elucidates the coalescence of perovskite crystals in perovskite solar cells stored in the dark at room temperature, showing that perovskite films within complete devices are highly dynamic as small crystals spontaneously coalesce to form larger crystals. This brings about a reduction in the number of grain boundaries and the associated trap states, which suppresses non-radiative recombination, resulting in increased PCE and reduced hysteresis upon storage. This self-repair ability, which improves the opto-electronic properties of perovskite films, provides an important insight into the success of perovskites as photovoltaic materials.

### 4.4 Materials and methods

#### 4.4.1 Scanning electron microscopy

The SEM micrographs were recorded on a Tescan MIRA 3 LMH with a field emission source operated at an acceleration voltage of 10 kV. SEM micrographs were further analysed using ImageJ.

#### 4.4.2 Time-correlated single-photon counting measurement

TCSPC data was collected using Florolog 322 spectrofluorometer (Horiba Jobin Yvon Ltd). A NanoLED-405LH (Horiba) laser diode (406 nm) (operated at a 400 kHz repetition rate) was used for excitation. The samples were mounted at 60° and the emission collected at 90° from the incident beam path. The detection monochromator was set to 760 nm with a 14 mm slit width and the photoluminescence was recorded using a picosecond photodetection module (TBX-04, Horiba Scientific).

#### 4.4.3 X-ray diffraction measurements

X-ray diffraction measurements were conducted using a Rigaku Ultima IV with a Cu K $\alpha$  source ( $\lambda = 0.154060$  nm) equipped with a dual position graphite diffracted beam monochromator and a scintillation counter detector, operating in the Bragg-Brentano geometry. A step size of 0.01° was chosen and an acquisition time of 2 min deg<sup>-1</sup> was used for the measurements. A baseline correction was applied. The angle dependent instrumental broadening was determined using a LaB<sub>6</sub> reference and subtracted from the full width at half maximum to determine the crystal size.

#### 4.4.4 Solar cell preparation

Fluorine doped tin oxide coated glass slides (Sigma-Aldrich,  $\sim 7/\square$ ) were cleaned by sonication in 2% Hellmanex solution for 15 min. After rinsing with deionised water and ethanol, the substrates were sonicated again with isopropanol and rinsed with acetone. The substrates were treated with UV-ozone for 15 min. For flat devices, a  $\text{SnO}_2$  compact layer was deposited by atomic layer deposition[42]. Mixed halide-mixed cation perovskite films were deposited from a precursor solution containing FAI (1 M),  $\text{PbI}_2$  (1.1 M),  $\text{CH}_3\text{NH}_3\text{Br}$  (0.2 M),  $\text{PbBr}_2$  (0.2 M) and CsI (0.075 M) in anhydrous DMF:DMSO 4:1 (v:v). The perovskite solution was spin-coated using a two-step program, 1000 and 6000 rpm for 10 and 20 s respectively. During the second step, 100  $\mu\text{l}$  of chlorobenzene was pipetted onto the spinning substrate 5 s before the end of the program. The substrates were then annealed at 100  $^\circ\text{C}$  for 1 hour in a nitrogen glove box. Subsequently, the substrates were cooled down for a few minutes and a spiro-OMeTAD (Merck) solution (70 mM in chlorobenzene) doped with bis(trifluoromethylsulfonyl)imide lithium salt (Li-TFSI, Aldrich), tris(2-(1H-pyrazol-1-yl)-4-tert-butylpyridine)-cobalt(III)tris(bis(trifluoromethylsulfonyl)imide) (FK209, Dyenamo) and 4-tert-butylpyridine (TBP, Aldrich) was spun at 4000 rpm for 20 s. The molar ratio of additives for spiro-OMeTAD was: 0.5, 0.03 and 3.3 for Li-TFSI, FK209 and TBP, respectively. Finally, 70 nm of gold was thermally evaporated under high vacuum on top of the HTM.

#### 4.4.5 Opto-electronic measurements

For photovoltaic measurements, a solar simulator from ABET Technologies (Model 11016 Sun 2000) with a xenon arc lamp was used and the solar cell response was recorded using a Metrohm PGSTAT302N Autolab. The intensity of the solar simulator was calibrated to 100  $\text{mW cm}^{-2}$  using a silicon reference cell from ReRa Solutions (KG5 filtered). J-V-curves were measured in reverse and forward bias at a scan rate of 10  $\text{mV s}^{-1}$ . A shadow mask was used to define the device active area (the area is given in the J-V figures). Maximum power point tracking was used to perform stability experiments. IMPS was performed according to the procedure described in the literature[108], using a 625 nm or blue LED driver at short circuit conditions and a light intensity of 100  $\text{mW cm}^{-2}$  and a Metrohm PGSTAT302N Autolab.



# Chapter 5 Conclusion

## 5.1 Achieved results

This thesis aimed to study the formation of perovskite thin films prepared via the main deposition routes used for preparing prototype solar cells — sequential deposition and the anti-solvent method. I also attempted to address related open questions regarding some specific changes that take place in perovskite films in solar cells during storage and operation.

Firstly, the thesis looked into the formation of perovskite in the sequential deposition. In Chapter 2, a previously undiscovered factor in the reaction, viz. illumination during film formation was shown to have a considerable influence on the rate of perovskite formation and the final perovskite film morphology. This surprising factor affects the perovskite formation by increasing the nucleation density of  $\text{PbI}_2$ , which is one of the reactants. I established that the increase in nucleation under illumination is due to a quantum effect rather than the heating effect of light. The aspects underlying this effect of illumination on nucleation were examined using photo-electrochemistry and a mechanism was proposed wherein photo-generated holes trapped in surface traps in  $\text{PbI}_2$  lower the surface tension, thus facilitating nucleation. The effect was demonstrated for  $\text{CH}_3\text{NH}_3\text{PbI}_3$  perovskite film made using sequential deposition. However, it was also shown to be robust for the anti-solvent method and for more complex perovskite compositions used in state-of-the art solar cells. While illumination is beneficial in the sequential deposition to obtain the highest solar cell performance, dark conditions are preferred for the anti-solvent method. Therefore, the main implication of this study is that awareness and control of the effect of illumination is crucial to obtain reproducible film quality and results.

In Chapter 2, CLSM was used to study perovskite formation in sequential deposition and it proved to be a valuable tool due to its ability to provide composition-based contrast in samples containing two or more semiconductors. In the same chapter, I also employed CLSM imaging to examine the formation of perovskites of increasing complex compositions deposited using the anti-solvent method. In unannealed double-cation film, due to the formation of various emissive species after the anti-solvent is dripped, perovskite formation proceeds from inhomogeneous starting conditions. However, for the triple-cation and Rb-incorporated compositions, the rapid formation of the perovskite phase directly and homogeneity of the film after the anti-solvent is dripped are likely to result in the formation of high quality films. This could contribute to the superior photovoltaic performance of solar cells made using these complex perovskite compositions.

Secondly, I systematically examined the path of the sequential deposition reaction as described in Chapter 3. I presented a fundamental understanding of the formation process and its different stages. SEM-CL imaging was used to unravel features on the nanometer scale in the formation of perovskite films. The novel cross-sectional CLSM technique revealed the directionality of the conversion reaction in an unprecedented way by showing that the  $\text{PbI}_2$  in the mesoporous scaffold, underneath the capping layer, is the last to convert and that unreacted  $\text{PbI}_2$  is trapped there even after long reaction times. Obtaining such information was not feasible with standard surface imaging, where layers lying underneath are inaccessible. I demonstrated that using both standard surface imaging and the new cross-sectional imaging technique together, we can obtain a complete picture of the solar cell. After analysis of kinetic data from different experimental conditions, we identified a model that explains the nucleation and crystal growth. Using the Avrami model, we could describe the formation kinetics under different reaction conditions of temperature, film thickness and illumination.

Finally, in Chapter 4, I described morphological changes that take place in solar cells during storage in the dark. I showed the spontaneous coalescence of perovskite crystals in the film where smaller crystals merge to form larger ones. This phenomenon improves the quality of the film as reflected in improvements in the opto-electronic properties and the solar cell performance. The dynamic nature of the perovskite film is an interesting piece in the puzzle to understand the performance of high efficiency solar cells.

In summary, this thesis provides an in-depth understanding of perovskite formation through different deposition methods and for different compositions. Such a comprehensive picture is indeed required to have adequate control over film quality and the related solar cell performance.

## 5.2 Future development

In this thesis, I demonstrated that illumination is an efficient and convenient way to control perovskite morphology thereby achieving higher photovoltaic performance. Future work that builds on this is likely to make use of illumination as a constructive tool. I foresee that it can be used for structuring perovskites and lead halides for various applications.

It would also be interesting to examine whether illumination can tune nucleation in other instances of perovskite formation such as the synthesis of perovskite nanocrystals[131] and nanowires[132] or the inverse-solubility crystallization of single crystals[133]. On another note, I anticipate that the light effect will gain interest during the implementation of the large-scale deposition of perovskite solar cells such as in roll-to-roll processing. As it affects the perovskite film morphology, illumination can be used to improve nucleation and thus surface coverage in cases where such bottlenecks arise. Thus, it

would be an important factor to consider for consistently producing high efficiency solar panels for the market.

In addition to the specific applications demonstrated in this thesis, CLSM has the potential to provide more insights into perovskite films and devices. Our innovative demonstration of cross-sectional CLSM opens the door for understanding the properties of perovskites in vertical cross sections of solar cells, not just the perovskite surface as in the literature. As CLSM allows one to image samples containing several semiconductors and obtain compositional contrast, it can provide interesting information in the design of opto-electronic devices in general.

The fundamental findings in this thesis pave the way for controlling perovskite morphology for fabricating high performance opto-electronic devices on the laboratory scale. This thesis aimed to contribute towards the long-term goal of establishing solution-based roll-to-roll production of perovskite solar cells for commercial purposes. On a broader note, in the quest for renewable energy technologies that can meet future energy needs, I hope that perovskite solar cells provide a part of the answer we need.



# References

1. Breyer, C. *et al.* On the role of solar photovoltaics in global energy transition scenarios. *Progress in Photovoltaics: Research and Applications* **25**, 727-745 (2017).
2. Ummadisingu, A. & Soni, M. S. Concentrating solar power – Technology, potential and policy in India. *Renewable and Sustainable Energy Reviews* **15**, 5169-5175 (2011).
3. Moriarty, P. & Honnery, D. What is the global potential for renewable energy? *Renewable and Sustainable Energy Reviews* **16**, 244-252 (2012).
4. U.S. Energy Information Administration, International Energy Outlook 2017, [www.eia.gov/ieo](http://www.eia.gov/ieo) (2017).
5. Valentine, S. V. Emerging symbiosis: Renewable energy and energy security. *Renewable and Sustainable Energy Reviews* **15**, 4572-4578 (2011).
6. Kittel, C. *Introduction to Solid State Physics*, 7<sup>th</sup> ed. 174-175, 199-201 (John Wiley and Sons, 1996).
7. Marchioro, A. *et al.* Unravelling the mechanism of photoinduced charge transfer processes in lead iodide perovskite solar cells. *Nature Photonics* **8**, 250-255 (2014).
8. Razykov, T. M. *et al.* Solar photovoltaic electricity: Current status and future prospects. *Solar Energy* **85**, 1580-1608 (2011).
9. El Chaar, L., Lamont, L. A. & El Zein, N. Review of photovoltaic technologies. *Renewable and Sustainable Energy Reviews* **15**, 2165-2175 (2011).
10. Bagnall, D. M. & Boreland, M. Photovoltaic technologies. *Energy Policy* **36**, 4390-4396 (2008).
11. Conibeer, G. Third-generation photovoltaics. *Materials Today* **10**, 42-50 (2007).
12. Ameri, T., Dennler, G., Lungenschmied, C. & Brabec, C. J. Organic tandem solar cells: A review. *Energy & Environmental Science* **2**, 347-363 (2009).
13. Grätzel, M. Dye-sensitized solar cells. *Journal of Photochemistry and Photobiology C: Photochemistry Reviews* **4**, 145-153 (2003).
14. Bach, U. *et al.* Solid-state dye-sensitized mesoporous TiO<sub>2</sub> solar cells with high photon-to-electron conversion efficiencies. *Nature* **395**, 583-585 (1998).
15. Klaus-Werner Benz, W. N. *Introduction to Crystal Growth and Characterization* 1-5, 171-173 (Wiley-VCH, 2014).
16. Nam-Gyu Park, M. G., Tsutomu Miyasaka (ed.) *Organic-Inorganic Halide Perovskite Photovoltaics*, 1<sup>st</sup> ed. 1-2 (Springer International Publishing, Switzerland; 2016).

17. Green, M. A., Ho-Baillie, A. & Snaith, H. J. The emergence of perovskite solar cells. *Nature Photonics* **8**, 506-514 (2014).
18. Gratzel, M. The light and shade of perovskite solar cells. *Nature Materials* **13**, 838-842 (2014).
19. Dar, M. I. *et al.* Origin of unusual bandgap shift and dual emission in organic-inorganic lead halide perovskites. *Science Advances* **2** (2016).
20. De Wolf, S. *et al.* Organometallic halide perovskites: Sharp optical absorption edge and its relation to photovoltaic performance. *The Journal of Physical Chemistry Letters* **5**, 1035-1039 (2014).
21. Herz, L. M. Charge-carrier mobilities in metal halide perovskites: Fundamental mechanisms and limits. *ACS Energy Letters* **2**, 1539-1548 (2017).
22. Kojima, A., Teshima, K., Shirai, Y. & Miyasaka, T. Organometal halide perovskites as visible-light sensitizers for photovoltaic cells. *Journal of the American Chemical Society* **131**, 6050-6051 (2009).
23. Im, J. H., Lee, C. R., Lee, J. W., Park, S. W. & Park, N. G. 6.5% efficient perovskite quantum-dot-sensitized solar cell. *Nanoscale* **3**, 4088-4093 (2011).
24. Kim, H. S. *et al.* Lead iodide perovskite sensitized all-solid-state submicron thin film mesoscopic solar cell with efficiency exceeding 9%. *Scientific Reports* **2**, 591 (2012).
25. Lee, M. M., Teuscher, J., Miyasaka, T., Murakami, T. N. & Snaith, H. J. Efficient hybrid solar cells based on meso-superstructured organometal halide perovskites. *Science* **338**, 643-647 (2012).
26. Etgar, L. *et al.* Mesoscopic CH<sub>3</sub>NH<sub>3</sub>PbI<sub>3</sub>/TiO<sub>2</sub> heterojunction solar cells. *Journal of the American Chemical Society* **134**, 17396-17399 (2012).
27. Heo, J. H. *et al.* Efficient inorganic-organic hybrid heterojunction solar cells containing perovskite compound and polymeric hole conductors. *Nature Photonics* **7**, 486-491 (2013).
28. Mei, A. *et al.* A hole-conductor-free, fully printable mesoscopic perovskite solar cell with high stability. *Science* **345**, 295-298 (2014).
29. Park, N.-G., Grätzel, M., Miyasaka, T., Zhu, K. & Emery, K. Towards stable and commercially available perovskite solar cells. *Nature Energy* **1**, 16152 (2016).
30. Berry, J. J. *et al.* Perovskite photovoltaics: The path to a printable terawatt-scale technology. *ACS Energy Letters* **2**, 2540-2544 (2017).
31. Burschka, J. *et al.* Sequential deposition as a route to high-performance perovskite-sensitized solar cells. *Nature* **499**, 316-319 (2013).
32. Liang, K., Mitzi, D. B. & Prikas, M. T. Synthesis and characterization of organic-inorganic perovskite thin films prepared using a versatile two-step dipping technique. *Chemistry of Materials* **10**, 403-411 (1998).
33. Bi, D. *et al.* Efficient luminescent solar cells based on tailored mixed-cation perovskites. *Science Advances* **2**, e1501170 (2016).



34. Jeon, N. J. *et al.* Solvent engineering for high-performance inorganic-organic hybrid perovskite solar cells. *Nature Materials* **13**, 897-903 (2014).
35. Saliba, M. *et al.* Incorporation of rubidium cations into perovskite solar cells improves photovoltaic performance. *Science* **354**, 206-209 (2016).
36. Saliba, M. *et al.* Cesium-containing triple cation perovskite solar cells: improved stability, reproducibility and high efficiency. *Energy & Environmental Science* **9**, 1989-1997 (2016).
37. McMeekin, D. P. *et al.* A mixed-cation lead mixed-halide perovskite absorber for tandem solar cells. *Science* **351**, 151-155 (2016).
38. Pellet, N. *et al.* Mixed-organic-cation perovskite photovoltaics for enhanced solar-light harvesting. *Angewandte Chemie* **53**, 3151-3157 (2014).
39. Eperon, G. E. *et al.* Formamidinium lead trihalide: a broadly tunable perovskite for efficient planar heterojunction solar cells. *Energy & Environmental Science* **7**, 982-988 (2014).
40. Pellet, N., Teuscher, J., Maier, J. & Grätzel, M. Transforming hybrid organic inorganic perovskites by rapid halide exchange. *Chemistry of Materials* **27**, 2181-2188 (2015).
41. Yang, W. S. *et al.* High-performance photovoltaic perovskite layers fabricated through intramolecular exchange. *Science* **348**, 1234-1237 (2015).
42. Correa Baena, J. P. *et al.* Highly efficient planar perovskite solar cells through band alignment engineering. *Energy & Environmental Science* **8**, 2928-2934 (2015).
43. Yi, C. *et al.* Entropic stabilization of mixed A-cation ABX<sub>3</sub> metal halide perovskites for high performance perovskite solar cells. *Energy & Environmental Science* **9**, 656-662 (2016).
44. Tsai, H. *et al.* High-efficiency two-dimensional Ruddlesden-Popper perovskite solar cells. *Nature* **536**, 312-316 (2016).
45. Noel, N. K. *et al.* Lead-free organic-inorganic tin halide perovskites for photovoltaic applications. *Energy & Environmental Science* **7**, 3061-3068 (2014).
46. Markov, I. V. *Crystal Growth for Beginners : Fundamentals of Nucleation, Crystal Growth and Epitaxy*, 2<sup>nd</sup> ed., repr. 4-5, 77-80, 172-173 (New Jersey : World Scientific, 2004).
47. Liu, F., Sommer, F., Bos, C. & Mittemeijer, E. J. Analysis of solid state phase transformation kinetics: models and recipes. *International Materials Reviews* **52**, 193-212 (2007).
48. Jackson, K. A. *Kinetic Processes: Crystal Growth, Diffusion and Phase Transitions in Materials*. 183-184 (Wiley-VCH, 2010).
49. Salim, T. *et al.* Perovskite-based solar cells: Impact of morphology and device architecture on device performance. *Journal of Materials Chemistry A* **3**, 8943-8969 (2015).
50. Sharenko, A. & Toney, M. F. Relationships between lead halide perovskite thin-film fabrication, morphology, and performance in solar cells. *Journal of the American Chemical Society* **138**, 463-470 (2016).

51. Mastroianni, S. *et al.* Analysing the effect of crystal size and structure in highly efficient  $\text{CH}_3\text{NH}_3\text{PbI}_3$  perovskite solar cells by spatially resolved photo- and electroluminescence imaging. *Nanoscale* **7**, 19653-19662 (2015).
52. deQuilettes, D. W. *et al.* Impact of microstructure on local carrier lifetime in perovskite solar cells. *Science* **348**, 683-686 (2015).
53. Deschler, F. *et al.* High photoluminescence efficiency and optically pumped lasing in solution-processed mixed halide perovskite semiconductors. *The Journal of Physical Chemistry Letters* **5**, 1421-1426 (2014).
54. Zhang, F. *et al.* Engineering of hole-selective contact for low temperature-processed carbon counter electrode-based perovskite solar cells. *Journal of Materials Chemistry A* **3**, 24272-24280 (2015).
55. Zhang, W. *et al.* Enhanced optoelectronic quality of perovskite thin films with hypophosphorous acid for planar heterojunction solar cells. *Nature Communications* **6**, 10030 (2015).
56. Ye, S. *et al.* A breakthrough efficiency of 19.9% obtained in inverted perovskite solar cells by using an efficient trap state passivator  $\text{Cu}(\text{thiourea})\text{I}$ . *Journal of the American Chemical Society* **139**, 7504-7512 (2017).
57. Stranks, S. D. *et al.* Recombination kinetics in organic-inorganic perovskites: Excitons, free charge, and subgap states. *Physical Review Applied* **2**, 034007 (2014).
58. Stranks, S. D. *et al.* Electron-hole diffusion lengths exceeding 1 micrometer in an organometal trihalide perovskite absorber. *Science* **342**, 341-344 (2013).
59. Kus, J. Application of confocal laser-scanning microscopy (CLSM) to autofluorescent organic and mineral matter in peat, coals and siliciclastic sedimentary rocks — A qualitative approach. *International Journal of Coal Geology* **137**, 1-18 (2015).
60. Ummadisingu, A. *et al.* The effect of illumination on the formation of metal halide perovskite films. *Nature* **545**, 208-212 (2017).
61. deQuilettes, D. W. *et al.* Photo-induced halide redistribution in organic-inorganic perovskite films. *Nature Communications* **7**, 11683 (2016).
62. Noh, J. H., Im, S. H., Heo, J. H., Mandal, T. N. & Seok, S. I. Chemical management for colorful, efficient, and stable inorganic-organic hybrid nanostructured solar cells. *Nano Letters* **13**, 1764-1769 (2013).
63. Patterson, A. L. The scherrer formula for X-Ray particle size determination. *Physical Review* **56**, 978-982 (1939).
64. Burschka, J. High performance solid-state mesoscopic solar cells. *PhD thesis-EPFL* (2013).
65. Tress, W. *et al.* Understanding the rate-dependent J-V hysteresis, slow time component, and aging in  $\text{CH}_3\text{NH}_3\text{PbI}_3$  perovskite solar cells: the role of a compensated electric field. *Energy & Environmental Science* **8**, 995-1004 (2015).
66. Senocrate, A. *et al.* The nature of ion conduction in methylammonium lead iodide: A multimethod approach. *Angewandte Chemie* **56**, 7755-7759 (2017).

## References

---

67. Yang, T. Y., Gregori, G., Pellet, N., Gratzel, M. & Maier, J. The significance of ion conduction in a hybrid organic-inorganic lead-iodide-based perovskite photosensitizer. *Angewandte Chemie* **54**, 7905-7910 (2015).
68. Im, J. H., Jang, I. H., Pellet, N., Gratzel, M. & Park, N. G. Growth of  $\text{CH}_3\text{NH}_3\text{PbI}_3$  cuboids with controlled size for high-efficiency perovskite solar cells. *Nature Nanotechnology* **9**, 927-932 (2014).
69. Bi, D., El-Zohry, A. M., Hagfeldt, A. & Boschloo, G. Unraveling the effect of  $\text{PbI}_2$  concentration on charge recombination kinetics in perovskite solar cells. *ACS Photonics* **2**, 589-594 (2015).
70. Ahn, N., Kang, S. M., Lee, J.-W., Choi, M. & Park, N.-G. Thermodynamic regulation of  $\text{CH}_3\text{NH}_3\text{PbI}_3$  crystal growth and its effect on photovoltaic performance of perovskite solar cells. *Journal of Materials Chemistry A* **3**, 19901-19906 (2015).
71. Klintonberg, M. K., Weber, M. J. & Derenzo, D. E. Luminescence and scintillation of  $\text{PbI}_2$  and  $\text{HgI}_2$ . *Journal of Luminescence* **102-103**, 287-290 (2003).
72. Kondo, S., Ohsawa, H., Asada, H. & Saito, T. Inherent excitonic luminescence in metal halide promising for potential applications in light-emitting devices. *Journal of Applied Physics* **107**, 103526 (2010).
73. Harms, H. A., Tetreault, N., Pellet, N., Bensimon, M. & Gratzel, M. Mesoscopic photosystems for solar light harvesting and conversion: facile and reversible transformation of metal-halide perovskites. *Faraday Discussions* **176**, 251-269 (2014).
74. Sandroff, C. J. Clusters in solution: Growth and optical properties of layered semiconductors with hexagonal and honeycombed structures. *The Journal of Chemical Physics* **85**, 5337 (1986).
75. Zheng, Z. *et al.* In situ growth of epitaxial lead iodide films composed of hexagonal single crystals. *Journal of Materials Chemistry* **15**, 4555-4559 (2005).
76. Ahmad, S., Kanaujia, P. K., Niu, W., Baumberg, J. J. & Vijaya Prakash, G. In situ intercalation dynamics in inorganic-organic layered perovskite thin films. *ACS Applied Materials & Interfaces* **6**, 10238-10247 (2014).
77. Cao, D. H. *et al.* Remnant  $\text{PbI}_2$ , an unforeseen necessity in high-efficiency hybrid perovskite-based solar cells? *APL Materials* **2**, 091101 (2014).
78. Mullin, J. W. *Industrial Crystallization* 3-22 (Plenum, 1975).
79. Bard, A. J. *Electrochemical Methods: Fundamentals and Applications*, 2<sup>nd</sup> ed. 53-54, 540-544 (New York : Wiley, New York; 2001).
80. Calloni, A. *et al.* Stability of organic cations in solution-processed  $\text{CH}_3\text{NH}_3\text{PbI}_3$  perovskites: formation of modified surface layers. *The Journal of Physical Chemistry C* **119**, 21329-21335 (2015).
81. Bott, A. W. Electrochemistry of Semiconductors. *Current Separations* **17**, 87-91 (1998).
82. Balluffi, R. W., Allen, S. M. & Carter, W. C. *Kinetics of Materials* 459-463 (Hoboken, NJ : John Wiley & Sons, 2005).

- 
83. Kramer, D. Dependence of surface stress, surface energy and surface tension on potential and charge. *Physical Chemistry Chemical Physics* **10**, 168-177 (2008).
84. Wu, Y. *et al.* Retarding the crystallization of  $\text{PbI}_2$  for highly reproducible planar-structured perovskite solar cells via sequential deposition. *Energy & Environmental Science* **7**, 2934-2938 (2014).
85. Ratke, L. & Voorhees, P. W. *Growth and Coarsening: Ostwald Ripening in Material Processing* 1-2 (Springer, 2002).
86. Tress, W., Corvers, S., Leo, K. & Riede, M. Investigation of driving forces for charge extraction in organic solar cells: Transient photocurrent measurements on solar cells showing S-shaped current-voltage characteristics. *Advanced Energy Materials* **3**, 873-880 (2013).
87. Khanna, P. K., Singh, N., Charan, S. & Viswanath, A. K. Synthesis of Ag/polyaniline nanocomposite via an in situ photo-redox mechanism. *Materials Chemistry and Physics* **92**, 214-219 (2005).
88. Correa-Baena, J. P. *et al.* Unbroken perovskite: Interplay of morphology, electro-optical properties, and ionic movement. *Advanced Materials* **28**, 5031-5037 (2016).
89. Moore, D. T. *et al.* Crystallization kinetics of organic-inorganic trihalide perovskites and the role of the lead anion in crystal growth. *Journal of the American Chemical Society* **137**, 2350-2358 (2015).
90. Albrecht, S. *et al.* Monolithic perovskite/silicon-heterojunction tandem solar cells processed at low temperature. *Energy & Environmental Science* **9**, 81-88 (2016).
91. Eperon, G. E., Burlakov, V. M., Goriely, A. & Snaith, H. J. Neutral color semitransparent microstructured perovskite solar cells. *ACS Nano* **8**, 591-598 (2014).
92. Saliba, M. *et al.* Influence of thermal processing protocol upon the crystallization and photovoltaic performance of organic-inorganic lead trihalide perovskites. *The Journal of Physical Chemistry C* **118**, 17171-17177 (2014).
93. Yang, L., Wang, J. & Leung, W. W.-F. Lead iodide thin film crystallization control for high-performance and stable solution-processed perovskite solar cells. *ACS Applied Materials & Interfaces* **7**, 14614-14619 (2015).
94. Wu, C.-G. *et al.* High efficiency stable inverted perovskite solar cells without current hysteresis. *Energy & Environmental Science* **8**, 2725-2733 (2015).
95. Tu, Y. *et al.* Solvent engineering for forming stonehenge-like  $\text{PbI}_2$  nano-structures towards efficient perovskite solar cells. *Journal of Materials Chemistry A* **5**, 4376-4383 (2017).
96. Chen, Q. *et al.* Controllable self-induced passivation of hybrid lead iodide perovskites toward high performance solar cells. *Nano Letters* **14**, 4158-4163 (2014).
97. Agrawal, H., Vedeshwar, A. G. & Saraswat, V. K. Growth and characterization of  $\text{PbI}_2$  thin films by vacuum thermal evaporation. *Journal of Nano Research* **24**, 1-6 (2013).
98. Baikie, T. *et al.* Synthesis and crystal chemistry of the hybrid perovskite  $(\text{CH}_3\text{NH}_3)\text{PbI}_3$  for solid-state sensitised solar cell applications. *Journal of Materials Chemistry A* **1**, 5628-5641 (2013).

- 
99. Jacobsson, T. J., Schwan, L. J., Ottosson, M., Hagfeldt, A. & Edvinsson, T. Determination of thermal expansion coefficients and locating the temperature-induced phase transition in methylammonium lead perovskites using X-ray diffraction. *Inorganic Chemistry* **54**, 10678-10685 (2015).
100. Ahmad, S., Kanaujia, P. K., Niu, W., Baumberg, J. J. & Vijaya Prakash, G. In situ intercalation dynamics in inorganic-organic layered perovskite thin films. *ACS Applied Materials & Interfaces* **6**, 10238-10247 (2014).
101. Liu, W. *et al.* Nucleation mechanism of  $\text{CH}_3\text{NH}_3\text{PbI}_3$  with two-step method for rational design of high performance perovskite solar cells. *Journal of Alloys and Compounds* **697**, 374-379 (2017).
102. Fernández, I., Cremades, A. & Piqueras, J. Cathodoluminescence study of defects in deformed (110) and (100) surfaces of  $\text{TiO}_2$  single crystals. *Semiconductor Science and Technology* **20**, 239-243 (2005).
103. Li, N. *et al.* Multifunctional perovskite capping layers in hybrid solar cells. *Journal of Materials Chemistry A* **2**, 14973-14978 (2014).
104. Khawam, A. & Flanagan, D. R. Solid-state kinetic models: basics and mathematical fundamentals. *The Journal of Physical Chemistry. B* **110**, 17315-17328 (2006).
105. Vyazovkin, S. *et al.* ICTAC Kinetics Committee recommendations for performing kinetic computations on thermal analysis data. *Thermochimica Acta* **520**, 1-19 (2011).
106. Nie, W. *et al.* Solar cells. High-efficiency solution-processed perovskite solar cells with millimeter-scale grains. *Science* **347**, 522-525 (2015).
107. Noel, N. K. *et al.* A low viscosity, low boiling point, clean solvent system for the rapid crystallisation of highly specular perovskite films. *Energy & Environmental Science* **10**, 145-152 (2017).
108. Seo, J.-Y. *et al.* Ionic liquid control crystal growth to enhance planar perovskite solar cells efficiency. *Advanced Energy Materials* **6**, 1600767 (2016).
109. Kim, M. C. *et al.* Observation of enhanced hole extraction in Br concentration gradient perovskite materials. *Nano Letters* **16**, 5756-5763 (2016).
110. Song, J. *et al.* Low-temperature  $\text{SnO}_2$ -based electron selective contact for efficient and stable perovskite solar cells. *Journal of Materials Chemistry A* **3**, 10837-10844 (2015).
111. Zhao, C. *et al.* Perovskite Solar Cells: Revealing underlying processes involved in light soaking effects and hysteresis phenomena in perovskite solar cells. *Advanced Energy Materials* **5**, 1500279 (2015).
112. Abate, A. *et al.* Silolothiophene-linked triphenylamines as stable hole transporting materials for high efficiency perovskite solar cells. *Energy & Environmental Science* **8**, 2946-2953 (2015).
113. Anaraki, E. H. *et al.* Highly efficient and stable planar perovskite solar cells by solution-processed tin oxide. *Energy & Environmental Science* **9**, 3128-3134 (2016).
114. Abate, A. *et al.* Lithium salts as "redox active" p-type dopants for organic semiconductors and their impact in solid-state dye-sensitized solar cells. *Physical Chemistry Chemical Physics* **15**, 2572-2579 (2013).

115. Leijtens, T. *et al.* Overcoming ultraviolet light instability of sensitized TiO<sub>2</sub> with meso-superstructured organometal tri-halide perovskite solar cells. *Nature Communications* **4**, 2885 (2013).
116. Aristidou, N. *et al.* The role of oxygen in the degradation of methylammonium lead trihalide perovskite photoactive layers. *Angewandte Chemie International Edition* **54**, 8208-8212 (2015).
117. O'Mahony, F. T. F. *et al.* Improved environmental stability of organic lead trihalide perovskite-based photoactive-layers in the presence of mesoporous TiO<sub>2</sub>. *Journal of Materials Chemistry A* **3**, 7219-7223 (2015).
118. Sheikh, A. D. *et al.* Atmospheric effects on the photovoltaic performance of hybrid perovskite solar cells. *Solar Energy Materials and Solar Cells* **137**, 6-14 (2015).
119. Fang, H. H. *et al.* Ultrahigh sensitivity of methylammonium lead tribromide perovskite single crystals to environmental gases. *Science Advances* **2**, e1600534 (2016).
120. Contreras, L. *et al.* Specific cation interactions as the cause of slow dynamics and hysteresis in dye and perovskite solar cells: a small-perturbation study. *Physical Chemistry Chemical Physics* **18**, 31033-31042 (2016).
121. Li, X. *et al.* A vacuum flash-assisted solution process for high-efficiency large-area perovskite solar cells. *Science*, 10.1126/science.aaf8060 (2016).
122. Noel, N. K. *et al.* Enhanced photoluminescence and solar cell performance via lewis base passivation of organic-inorganic lead halide perovskites. *ACS Nano* **8**, 9815-9821 (2014).
123. Pattabi, M. *et al.* Aging studies on discontinuous silver films in ultrahigh vacuum. *Thin Solid Films* **322**, 340-343 (1998).
124. Paulson, G. G. & Friedberg, A. L. Coalescence and agglomeration of gold films. *Thin Solid Films* **5**, 47-52 (1970).
125. Goudy, A., Gee, M. L., Biggs, S. & Underwood, S. Atomic force microscopy study of polystyrene latex film morphology: Effects of aging and annealing. *Langmuir* **11**, 4454-4459 (1995).
126. German, R. M. *Sintering: from Empirical Observations to Scientific Principles* 75-76, 227-228 (Butterworth-Heinemann, Boston; 2014).
127. Liu, D. *et al.* Controlling CH<sub>3</sub>NH<sub>3</sub>PbI<sub>3-x</sub>Cl<sub>x</sub> film morphology with two-step annealing method for efficient hybrid perovskite solar cells. *ACS Applied Materials & Interfaces* **7**, 16330-16337 (2015).
128. Liu, J. *et al.* Improved crystallization of perovskite films by optimized solvent annealing for high efficiency solar cell. *ACS Applied Materials & Interfaces* **7**, 24008-24015 (2015).
129. Yang, M. *et al.* Facile fabrication of large-grain CH<sub>3</sub>NH<sub>3</sub>PbI<sub>3-x</sub>Br<sub>x</sub> films for high-efficiency solar cells via CH<sub>3</sub>NH<sub>3</sub>Br-selective Ostwald ripening. *Nature Communications* **7**, 12305 (2016).
130. Sheng, R. *et al.* Photoluminescence characterisations of a dynamic aging process of organic-inorganic CH<sub>3</sub>NH<sub>3</sub>PbBr<sub>3</sub> perovskite. *Nanoscale* **8**, 1926-1931 (2016).



## References

---

131. Maceiczky, R. M. *et al.* Microfluidic reactors provide preparative and mechanistic insights into the synthesis of formamidinium lead halide perovskite nanocrystals. *Chemistry of Materials* **29**, 8433-8439 (2017).
132. Horvath, E. *et al.* Nanowires of methylammonium lead iodide ( $\text{CH}_3\text{NH}_3\text{PbI}_3$ ) prepared by low temperature solution-mediated crystallization. *Nano Letters* **14**, 6761-6766 (2014).
133. Kadro, J. M., Nonomura, K., Gachet, D., Gratzel, M. & Hagfeldt, A. Facile route to freestanding  $\text{CH}_3\text{NH}_3\text{PbI}_3$  crystals using inverse solubility. *Scientific Reports* **5**, 11654 (2015).



# Acknowledgements

I would like to express my deep gratitude to Prof. Michael Grätzel for giving me the opportunity to undertake my PhD work with him. I am extremely grateful to him for taking great interest in my work and giving me invaluable inputs and guidance through innumerable discussions throughout my PhD, not to mention the support and freedom I was given to explore the new and seemingly inexplicable.

I am sincerely thankful to Dr. Wolfgang Tress for his insightful scientific feedback and his patient counsel during the course of my PhD. I also thank him for painstakingly proofreading my publications and this thesis.

I am grateful for the valuable scientific inputs provided by Dr. Robin Humphry-Baker for spectroscopy and Dr. Kurt Schenk for XRD measurements. The practical support for CLSM imaging provided by the BIOP team, Dr. Luigi Bozzo and Dr. Romain Guet, is very much appreciated. I acknowledge Dr. David Gachet (Attolight AG) for collecting the CL images. I gratefully acknowledge my collaborators on various projects - Dr. Ludmilla Steier, Ji-Youn Seo, Taisuke Matsui, Dr. Michael Saliba, Dr. Simone Meloni and Dr. Bart Roose. I am grateful to the Swiss National Science Foundation for their financial support.

I wish to express my thanks to Dr. Thomas Moehl, Dr. Fabrizio Giordano, Dr. Antonio Abate and Dr. Juan-Pablo Correa-Baena for their collaboration, friendship and helpful advice on navigating many a difficult situation. I would also like to thank the secretaries – Heidi Franchelet, Carmen Biagini and Anne-Lene Odegaard for their timely help on many occasions.

I thank my colleagues Konrad, Marcel, Jingshan, Matt, Paul, Marko and others at LPI and LSPM for all the interesting lunch discussions and laughs that made this time in Lausanne unforgettable. Special thanks to Saba, Cristina and Lucie for their steadfast friendship.

Last but not the least, I would like to thank my parents and my brother, without whose love and support not one ounce of this could have been accomplished.

Lausanne, 13<sup>th</sup> December 2017



# Curriculum Vitae

**Name:** Amita Ummadisingu

**Date, Place of Birth:** 28.02.1990, Hyderabad, India.

**Email:** amitahyd@gmail.com

## EDUCATION

- **École Polytechnique Fédérale de Lausanne (EPFL), Switzerland.**  
PhD in Chemistry and Chemical Engineering (Oct. 2014 – Dec. 2017)
- **École Polytechnique Fédérale de Lausanne (EPFL), Switzerland.**  
Master in Chemical Engineering and Biotechnology (Sept. 2012 – Jul. 2014)
- **Birla Institute of Technology and Science (BITS) - Pilani, India.**  
Bachelor of Engineering (Hons) in Chemical Engineering (Aug. 2007 - Jun. 2011)

## PROFESSIONAL EXPERIENCE

- **Swiss Center for Electronics and Microtechnology (CSEM), Muttenez, Switzerland.**  
(Masters Internship: Aug. 2013 - Feb. 2014)  
Project: Fabrication and characterization of organic tandem photovoltaic modules
- **1<sup>st</sup> Institute of Physics, University of Stuttgart, Germany.**  
(Visiting Scholar: Oct. 2011 - Apr. 2012)  
Project: Functionalized single walled carbon nanotubes for application in photovoltaics
- **Oracle Financial Services Software Ltd., Bangalore, India.**  
(Practice School II: Jan. 2011 - Jun. 2011)  
Project: Development of user interface screens for Oracle FLEXCUBE
- **National Geophysical Research Institute, Hyderabad, India.**  
(Practice School I: May 2009 - Jul. 2009)  
Project: Application of signal processing in MATLAB to discriminate earthquakes from explosions

## PROFESSIONAL QUALIFICATIONS

- **Languages known:** English (Fluent), Hindi (Fluent), Telugu (Fluent), French (B1), German (B1), Japanese (A1)
- **Certifications:** Labview Core I and II
- **Programming:** C, C++, Java
- **Software skills:** Microsoft Office, Adobe Illustrator, Wavemetrics IgorPro, OriginLab Origin, ImageJ/Fiji, FullProf, MATLAB

**AWARDS**

- Best poster award for Master projects in the Spring of 2014 by Section of Chemistry and Chemical Engineering at EPFL.
- Swiss Government Scholarship 2012 for the Master's degree at EPFL.
- Scholarship from the University of Stuttgart to work at the 1<sup>st</sup> Institute of Physics.
- Recipient of the R. P. Vaid Award - 2010 awarded by BITSAA International and Chemical Engineering Association - BITS Pilani, for excellence in academics and all-round achievements for the class of 2011.
- Awarded BITS and BITSAA Travel Scholarship in the year 2010 for attending the conference – AIChE Annual Meeting 2010, Salt Lake City, USA.

**PUBLICATIONS**

- Ummadisingu, A. & Grätzel, M. Revealing the detailed path of sequential deposition for metal halide perovskite formation. *Science Advances*, In press.
- Ummadisingu, A. *et al.* The effect of illumination on the formation of metal halide perovskite films. *Nature* **545**, 208-212 (2017).
- Roose, B.\*; Ummadisingu, A.\* *et al.* Spontaneous crystal coalescence enables highly efficient perovskite solar cells. *Nano Energy*, <http://dx.doi.org/10.1016/j.nanoen.2017.06.037> (2017).  
\* Contributed equally
- Ummadisingu, A. *et al.* Additives, hole transporting materials and spectroscopic methods to characterize the properties of perovskite films. *Chimia* **71**, 754-761 (2017).
- Pan, L. *et al.* New benchmark Cu<sub>2</sub>O photocathodes for solar water splitting. *Nature Catalysis*, Submitted.
- Cao, Y. *et al.* 11% efficiency solid-state dye-sensitized solar cells with copper (II/I) hole transport materials. *Nature Communications* **8**, doi: 10.1038/ncomms15390 (2017).
- Saliba, M. *et al.* Incorporation of rubidium cations into perovskite solar cells improves photovoltaic performance. *Science*, 10.1126/science.aah5557 (2016).
- Hadadian, M. *et al.* Enhancing efficiency of perovskite solar cells via N-doped graphene: Crystal modification and surface passivation. *Advanced Materials*, 10.1002/adma.201602785 (2016).
- Seo, J.-Y. *et al.* Ionic liquid control crystal growth to enhance planar perovskite solar cells efficiency. *Advanced Energy Materials*, 10.1002/aenm.201600767 (2016).
- Ummadisingu, A. & Gupta, S. Characteristics and kinetic study of chitosan prepared from seafood industry waste for oil spills cleanup. *Desalination and Water Treatment* **44**, 44-51 (2012).
- Ummadisingu, A. & Soni, M.S. Concentrating solar power technology, potential and policy in India. *Renewable and Sustainable Energy Reviews* **15**, 5169-5175 (2011).



## CONFERENCES

- Ummadisingu, A. & Grätzel, M. Mechanism of perovskite film formation and the effect of light. *Elevator pitch & poster 67<sup>th</sup> Lindau Nobel Laureate Meeting in Chemistry*, Lindau, Germany, Jun. 25- 30, 2017.
- Ummadisingu, A. & Grätzel, M. Mechanism of perovskite formation and strategies for controlling morphology. *Proc. HOPV-2017*, Lausanne, Switzerland, May 21- 24, 2017.
- Ummadisingu, A., Steier, L., Tress, W. & Grätzel, M. Kinetics of metal halide perovskite formation by sequential deposition. *Proc. HOPV-2016*, Swansea, UK, Jun. 28 - Jul. 1, 2016.
- Ummadisingu, A., Pellet N. & Grätzel, M. Kinetics of methylammonium lead iodide perovskite formation on mesoporous layers via the sequential deposition method. *Poster HOPV-2015*, Rome, Italy, May 10-13, 2015.
- Ummadisingu, A., Sheth, P. & Babu, B.V. Experimental studies on gasification of wood shavings of pine wood in a downdraft biomass gasifier. *Proc. AIChE Annual Meeting 2010*, Salt Lake City, Utah, USA, Nov. 7-12, 2010.
- Sheth, P., Ummadisingu, A. & Babu, B.V. Combined transport and kinetic modeling of downdraft biomass gasifier. *Proc. AIChE Annual Meeting 2010*, Salt Lake City, Utah, USA, Nov. 7-12, 2010.
- Ummadisingu, A. & Gupta, S. Utilization of chitosan prepared from seafood industry waste to clean up oil spills. *Proc. CHEMCON-2009*, Andhra University, Visakhapatnam, India, Dec. 27-31, 2009.